

---

# Aerosol characterization by multi-wavelength Raman- and depolarization lidar observations

Silke Martha Groß

---



München 2011



---

# **Aerosol characterization by multi-wavelength Raman- and depolarization lidar observations**

**Silke Martha Groß**

---

Dissertation  
an der Fakultät für Physik  
der Ludwig–Maximilians–Universität  
München

vorgelegt von  
Silke Martha Groß  
aus Kulmbach

München, den 04.02.2011

Erstgutachter: Prof. Dr. Bernhard Mayer

Zweitgutachter: Dr. Bernadett Weinzierl

Tag der mündlichen Prüfung: 09.05.2011

# Contents

<b>Abstract</b>	<b>v</b>
<b>1 Introduction</b>	<b>1</b>
1.1 Aerosols and climate	2
1.2 Selected aerosols of the Earth's atmosphere	4
1.2.1 Desert dust	4
1.2.2 Biomass burning aerosols	5
1.2.3 Marine aerosols	7
1.2.4 Volcanic ash particles	8
1.3 Benefit of advanced lidar measurements	9
1.4 Saharan mineral dust experiment	10
1.5 Objective and structure of this thesis	12
1.6 External data	13
<b>2 Lidar technique</b>	<b>15</b>
2.1 Lidar technique	15
2.2 Lidar equation	16
2.3 Inversion of the lidar equation	17
2.3.1 Klett- / Fernald-Algorithm	17
2.3.2 Raman method	19
2.4 Depolarization	22
2.4.1 Polarization lidar method	22
2.4.2 Depolarization calibration	25
2.5 Error calculation	26
2.5.1 Error of the lidar ratio	26
2.5.2 Error of the particle linear depolarization ratio	31
<b>3 Instrumentation</b>	<b>33</b>
3.1 Lidar systems	33
3.1.1 POLIS	33
3.1.2 MULIS	35
3.1.3 Bertha	37
3.1.4 HSRL	38

---

3.2	Sun-photometer and radiosondes . . . . .	38
3.3	Improvements of POLIS . . . . .	39
3.3.1	Gluing algorithm . . . . .	39
3.3.2	Depolarization calibration . . . . .	41
<b>4</b>	<b>Characterization</b>	<b>43</b>
4.1	Saharan dust . . . . .	43
4.1.1	Fresh pure Saharan dust . . . . .	43
4.1.2	Aged pure Saharan dust . . . . .	47
4.1.3	Long-range transported Saharan dust . . . . .	51
4.1.4	Change of optical properties during transport . . . . .	55
4.2	Biomass burning aerosols . . . . .	58
4.3	Marine aerosols . . . . .	62
4.4	Volcanic ash particles . . . . .	65
4.4.1	Pure volcanic ash . . . . .	65
4.4.2	Volcanic ash and sulfuric acid mixed with boundary layer aerosols . . . . .	68
<b>5</b>	<b>Discussion</b>	<b>73</b>
5.1	Review of $S_p$ and $\delta_p$ . . . . .	73
5.2	Changes of optical properties of Saharan dust . . . . .	74
5.3	Comparison of AOD . . . . .	75
5.4	Discrimination of aerosol types . . . . .	77
5.5	Change of optical properties in aerosol mixtures . . . . .	80
5.6	Determination of volume fraction . . . . .	83
5.7	Hygroscopicity and depolarization . . . . .	87
<b>6</b>	<b>Conclusion</b>	<b>91</b>
<b>A</b>	<b>Statistical information</b>	<b>95</b>
<b>B</b>	<b>List of abbreviatons</b>	<b>105</b>
	<b>Acknowledgment</b>	<b>118</b>

# Zusammenfassung

Aerosole sind ein wichtiger Parameter in Bezug auf Klimaänderungen, dennoch werden sie nur unzureichend in Klimamodellen dargestellt. Die Hauptursache hierfür ist die eingeschränkte Kenntnis ihrer räumlichen und zeitlichen Verteilung, sowie ihrer optischen Eigenschaften. Besonders die Nicht-Sphärizität individueller Aerosoltypen macht die Modellierung der optischen Eigenschaften schwierig. In dieser Studie werden mehrwellenlängen Raman- und Depolarisations-Lidarmessungen dazu genutzt, vier der Haupt-Aerosoltypen der Atmosphäre — Saharastaub, Aerosole aus Biomasseverbrennung, marines Aerosol und Vulkanstaub — zu charakterisieren. Die Aerosoltypen wurden bezüglich des linearen Partikeldepolarisationsverhältnisses und des Lidarverhältnisses untersucht. Die Messungen wurden während der Feldmesskampagnen des SAMUM-Projekts und während besonderer meteorologischer Ereignisse über München/Maisach durchgeführt. Insgesamt basiert diese Arbeit auf etwa 600 Stunden Lidarmessungen.

Auf Grund von Verbesserungen des portablen Lidarsystems POLIS war es möglich, die gerätebedingten Fehler deutlich zu verringern. Dadurch war es zum ersten Mal möglich, die Wellenlängenabhängigkeit der linearen Partikeldepolarisation von Saharastaub zu untersuchen. Desweiteren wurden in dieser Arbeit die optischen Eigenschaften von ferntransportiertem Saharastaub über München charakterisiert, sowie deren transportbedingte Änderungen untersucht. Eine signifikante Änderung der Wellenlängenabhängigkeit der linearen Partikeldepolarisation zwischen frischem, gealtertem und ferntransportiertem Saharastaub wurde gefunden. Zur Untersuchung von Wellenlängenabhängigkeit und Änderung der optischen Eigenschaften, ist eine genaue Fehlerangabe erforderlich. Deshalb wurde in dieser Arbeit eine analytische Fehlerrechnung entwickelt, die sowohl den systematischen Fehler, resultierend aus Unsicherheiten der Input-Parameter, sowie den statistischen Fehler, bedingt durch Signalrauschen, des Lidarverhältnisses beinhaltet. Resultierend aus genauen Messungen und geringen Fehlern konnten eindeutige Unterschiede der optischen Eigenschaften der untersuchten Aerosoltypen gefunden werden. Diese Unterschiede zeigen den Nutzen von hochentwickelten Lidarsystemen zur Erkennung unterschiedlicher Aerosoltypen. Die Änderung der linearen Partikeldepolarisation und des Lidarverhältnisses in einer Zweikomponentenmischung wurde berechnet und ein nichtlinearer Verlauf gefunden. Basierend auf Messungen der linearen Partikeldepolarisation wurde der Anteil der einzelnen Aerosoltypen an einer Zweikomponentenmischung bestimmt. Vergleiche mit unabhängigen Messungen stellen die Anwendbarkeit dieser Methode sicher.





# Abstract

Aerosols are one key parameter in global climate changes, but they are only poorly characterized in climate models. The main reason is the limited knowledge about aerosol distribution and aerosol optical properties. Especially the non-spherical shape of individual aerosols makes it difficult to model their optical parameters. In this study multi-wavelength Raman- and depolarization-lidar measurements are used to characterize four major aerosol types of the atmosphere — Saharan dust, biomass burning aerosols, marine aerosols and volcanic ash. The aerosol types were investigated with respect to their wavelength dependent values of the linear particle depolarization ratio and the extinction-to-backscatter ratio (lidar ratio). The measurements were performed during the field experiments of the SAMUM project and during special meteorological events over Munich/Maisach. Altogether this study is based on about 600 hours of lidar measurements.

Due to of the improvements of the portable lidar system POLIS, the errors of the retrieved optical properties could be decreased significantly. Thus, for the first time it was possible to determine a wavelength dependence of the particle linear depolarization ratio of Saharan dust. Furthermore, the changes of the optical properties of Saharan dust and their wavelength dependence during transport was analyzed in this thesis. A significant change of the wavelength dependence of the particle linear depolarization ratio between fresh, aged, and long-range transported Saharan dust to Central Europe was found. It is obvious that for the investigation of wavelength dependence and changes of optical properties the knowledge about the uncertainties of the results is as important as the measurement itself. Therefore an analytical error calculation of the systematical errors, due to uncertainties in the input values, and the statistical errors, due to signal-noise, of the lidar ratio was developed. As a benefit of the highly accurate measurements and the resulting small errors significant differences in the optical properties of the four investigated aerosol types were found. These differences highlight the potential of advanced lidar measurements to distinguish between individual aerosol types. In a further step, the changes of the linear particle depolarization ratio and the lidar ratio in a two-component aerosol mixture was calculated, and a non-linear characteristic was found. Based on lidar measurements of the linear depolarization ratio, the contribution of the individual aerosol types to a two-component aerosol mixture was determined, using the example of a dust and marine aerosol mixture in the planetary boundary layer during the second field campaign of SAMUM. A comparison with independent in-situ measurements proved the applicability of this method.

Parts of this work have been published in:

Peer reviewed journals:

Groß, S., Freudenthaler, V., Toledano, C., and Wiegner, M.: Lidar ratio of Saharan dust over Cape Verde Islands: Assessment and error calculation, *Journal of Geophysical Research* - in print

Groß, S., Tesche, M., Freudenthaler, V., Toledano, C., Wiegner, M., Ansmann, A., Althausen, D., and Seefeldner, M.: Characterization of Saharan dust, marine aerosols and a mixture of biomass burning aerosols and dust by means of multi-wavelength depolarization- and Raman-measurements during SAMUM 2, *Tellus B* - accepted

Groß, S., Gasteiger, J., Freudenthaler, V., Wiegner, M., Geiß, A., Schladitz, A., Toledano, C., Kandler, K., Tesche, M., Ansmann, A., and Wiedensohler A.: Characterization of the planetary boundary layer by means of lidar measurements during SAMUM-2, *Tellus B* - accepted

Groß, S., Freudenthaler, V., Gasteiger, J., Geiß, A., Schnell, F., and Wiegner, M.: 2011 Dual-wavelength linear depolarization ratio of volcanic aerosols: lidar measurements of the Eyjafjallajökull plume over Maisach, Germany, *Atmospheric Environment* - accepted

Ansmann, A., Tesche, M., Groß, S., Freudenthaler, V., Seifert, P., Hiebsch, A., Schmidt, J., Wandinger, U., Matthis, I., Müller, D., and Wiegner, M.: the 16 April 2010 major volcanic ash plume over central Europe: EARLINET lidar and AERONET photometer observations at Leipzig and Munich, Germany, *Geophys. Res. Lett.*, 37, doi:10.1029/2010GL043809, 2010

Ansmann, A., Tesche, M., Seifert, P., Groß, S., Freudenthaler, V., Apituley, A., Wilson, K. M., Serikov, I., Linne, H., Heinold, B., Hiebsch, A., Schnell, F., Schmidt, J., Mattis, I., Wandinger, U., and Wiegner, M.: Lidar profiling of ash and sulfate particle mass over central Europe after the eruption of the Eyjafjallajökull volcano, *Journal of Geophysical Research* - accepted

Emeis, S., Junkermann, W., Schäfer, K., Forkel, R., Suppan, P., Flentje, H., Gilge, S., Fricke, W., Wiegner, W., Freudenthaler, V., Groß, S., Ries, L., Meinhardt, F., Münkel, C. and Obleitner, F.: Spatial structure and dispersion of the April 16/17, 2010 volcanic ash cloud over Germany, *Atmospheric Chemistry and Physics Discussion*, 2010

Gasteiger, J., Groß, S., Freudenthaler, V., and Wiegner, M.: Volcanic ash from Iceland over Munich: Mass concentration retrieved from ground-based remote sensing measurements, *Atmospheric Chemistry and Physics*, 2011

Gasteiger, J., Wiegner, M., Groß, S., Freudenthaler, V., Toledano, C., Tesche, M., and Kandler, K., Modeling lidar-relevant optical properties of complex mineral dust aerosols, *Tellus B* - accepted

Heinold, B., Tegen, I., Esselborn, M., Freudenthaler, V., Groß, S., Kandler, K., Knipertz, P., Müller, D., Schepanski, K., and Schladitz, A., Regional modelling of Saharan dust and land fire smoke: Model description and validation, *Tellus B* - accepted

Köhler, C., Trautmann, T., Lindermeir, E., Vreeling, W., Lieke, K., Kandler, K., Weinzierl, B., Groß, S., and Tesche, M.: Comparison of Ground Based Radiation Measurements in the Thermal IR during SAMUM-2 with Radiative Transfer Simulations, *Tellus B* - submitted

Schladitz, A. Müller, T. Nordmann, S., Tesche, M. Groß, S., Freudenthaler, V., Gasteiger, J., and Wiedensohler, A., In situ aerosol characterization at Cape Verde, Part 2: Parameterization of relative humidity- and wavelength-dependent aerosol optical properties, *Tellus B* - accepted

Schumann, U., Weinzierl, B., Reitebuch, O., Schlager, H., Minikin, A., Forster, C., Baumann, R., Sailer, T., Graf, K., Mannstein, H., Voigt, C., Rahm, S., Simmet, R., Scheibe, M., Lichtenstern, M., Stock, P., Rüba, H., Schäuble, D., Tafferner, A., Rautenhaus, M., Gerz, T., Ziereis, H., Krautstrunk, M., Mallaun, C., Gayet, J.-F., Lieke, K., Kandler, K., Ebert, M., Weinbruch, S., Stohl, A., Gasteiger, J., Groß, S., Freudenthaler, V., Wiegner, M., Ansmann, A., Tesche, M., Olafsson, H., and Sturm, K.: Airborne observations of the Eyjafjalla volcano ash cloud over Europe during air space closure in April and May 2010, *Atmospheric Chemistry and Physics*, 2011

Seifert, P., Ansmann, A., Groß, S., Freudenthaler, V., Heinold, B. Hiebsch, A., Schmidt, J., Schnell, F., Tesche, M., Wandinger, U., Mattis, I., and Wiegner, M.: Ice formation in ash-influenced clouds after the eruption of the Eyjafjallajökull volcano in April 2010, *Journal of Geophysical Research* - submitted

Tesche, M., Ansmann, A., Müller, D., Althausen, D., Engelmann, R., Freudenthaler, V., and Groß, S.: Vertically resolved separation of dust and smoke over Cape Verde by using multiwavelength Raman and polarization lidars during Saharan Mineral Dust Experiment 2008. *J. Geophys. Res.* 114, doi: 10.1029/2009JD011862, 2009b

Tesche, M., Groß, S., Ansmann, A., Müller, D., Althausen, D., Freudenthaler, V., and Esselborn, M. 2011. Profiling of Saharan dust and biomass burning smoke with multiwavelength polarization Raman lidar at Cape Verde, *Tellus B* - accepted

Tesche, M., Müller, D., Groß, S., Ansmann, A., Althausen, D., and Freudenthaler, V., Optical and microphysical properties of smoke over Cape Verde inferred from multiwavelength lidar measurements, *Tellus B* - accepted

Toledano, C., Wiegner, M., Groß, S., Freudenthaler, V., Gasteiger, J., Müller, D., Müller, T., Schladitz, A., Torres, B., and O'Neill, N., 2011, Optical properties of aerosol mixtures derived from sun-sky radiometer during SAMUM-2, *Tellus* - accepted

Weinzierl, B., Sauer, D., Esselborn, M., Petzold, A., Veira, A., Rose, M., Mund, S., Wirth, M., Ansmann, A., Tesche, M., Groß, S., and Freudenthaler, V.: Microphysical and optical properties of dust and tropical biomass burning aerosol layers in the Cape Verde region - An overview of the airborne in situ and lidar measurements during SAMUM-2, *Tellus* - submitted

Wiegner, M., Gasteiger, J., Groß, S., Schnell, F., Freudenthaler, V., and Forkel, R., 2010. Characterization of the Eyjafjallajökull ash-plume: Potential of lidar remote sensing, - *J. Phys. Chem. Earth* - accepted

#### Conference Proceedings:

Groß, S., Freudenthaler, V., Toledano, C., Seefeldner, M., and Wiegner, M., 2008. Mini-lidar measurements of particle depolarization and Raman scattering of Saharan-dust and biomass burning at 355 nm during SAMUM 2, *Proc. Of 24th International Laser Radar Conference, Boulder, USA, 23-27 June 2008, S04P-10*

Groß, S., Freudenthaler, V., Gasteiger, J., Schnell, F., Hayek, T., Eifried, M., Wiegner, M., and Köpke, P., 2009, Optical properties of long-range transported Saharan dust over Southern Germany, *International Symposium of Tropospheric Profiling, Delft, Netherlands, 2009*

Groß, S., Freudenthaler, V., Tesche, M., Althausen, D., and Wiegner, M., Optical properties of marine aerosols, Saharan dust, and dust and biomass burning aerosols - lidar measurements during SAMUM2, *Proc. Of 25th International Laser Radar Conference, St. Petersburg, Russia, 5-9 July 2010*

Groß, S., Gasteiger, J., Freudenthaler, V., Schnell, F., and Wiegner, M., 2010. Characterization of the Eyjafjallajökull ash-plume by means of lidar measurements over the Munich EARLINETsite, Proc. of SPIE Vol. 7827, Toulouse, France, 20-23 September 2010

Freudenthaler, V., Groß, S., Engelmann, R., Mattis, I., Wandinger, U., Pappalardo, G., Amodeo, A., Giunta, A., D'Amico, G., Chaikovsky, A., Osipenko, F., Slesar, A., Nicolae, D., Belegante, L., Talianu, C., Serikov, I., Linne, H., Jansen, F., Wilson, K.M., de Graaf, M., Apituley, A., Trickl, T., Giehl, H., and Adam, M, EARLI09 - direct intercomparison of eleven EARLINET lidar systems, Proc. Of 25th International Laser Radar Conference, St. Petersburg, Russia, 5-9 July 2010

Gasteiger, J., Groß, S., Freudenthaler, V., and Wiegner, M., Study on spectral lidar-related optical properties of mineral dust aerosols with complex microphysical properties, Proc. Of 25th International Laser Radar Conference, St. Petersburg, Russia, 5-9 July 2010

Pappalardo, G., Amodeo, A., Ansmann, A., Apituley, A., Alados Arboledas, L., Balis, D., Böckmann, C., Chaikovsky, A., Comeron, A., D'Amico, G., De Tomasi, F., Freudenthaler, V., Giannakaki, E., Giunta, A., Grigorov, I., Gustafsson, O., Groß, S., Haeffelin, M., Iarlori, M., Kinne, S., Linne, H., Madonna, F., Mamouri, R., Mattis, I., McAuliffe, M., Molero, F., Mona, L., Müller, D., Mitev, V., Nicolae, D., Papayannis, A., Perrone, M. R., Pietruczuk, A., Pujadas, M., Putaid, J.-P., Ravetta, F., Rizi, V., Serikov, I., Sicard, M., Simeonov, V., Spinelli, N., Stebel, K., Trickl, T., Wandinger, U., Wang, X., Wagner, F., and Wiegner, M., EARLINET observations of the Eyjafjallajökull ash plume over Europe, Proc. of SPIE Vol. 7827, Toulouse, France, 20-23 September 2010

Tesche, M., Ansmann, A., Althausen, D., Müller, D., Freudenthaler, V., and Groß, S., Multiwavelength polarization Raman lidar measurements of dust and smoke at Cape Verde during SAMUM-2, Proc. Of 25th International Laser Radar Conference, St. Petersburg, Russia, 5-9 July 2010

Tesche, M., Ansmann, A., Althausen, D., Heese, B., Müller, D., Freudenthaler, V., Groß, S., and Wiegner, M., Lidar Observations of Pure and Aged Saharan Dust during the Saharan Mineral Dust Experiments 1 and 2, Proc. Of 24th International Laser Radar Conference, Boulder, USA, 23-27 June 2008



# Chapter 1

## Introduction

Nine of the ten warmest years since the beginning of the instrumental record were observed in the last ten years (2001-2010) (NOAA, 2011). The global mean temperature averaged over land and ocean increased by  $0.76^{\circ}\text{C} \pm 0.19^{\circ}\text{C}$  within the last century (IPCC, 2007). Notable is that the rate of warming during the last 50 years almost doubles the rate of warming over the last 100 years. It is estimated that most of the observed increase in global averaged temperature since the mid 20th century is due to the increase in anthropogenic greenhouse gas concentration (IPCC, 2007). However, the warming caused by the increase of greenhouse gas concentration is very likely to be even higher than observed. Aerosol particles from volcanic eruptions or from anthropogenic sources may offset some warming that would otherwise have taken place (IPCC, 2007). The understanding of the impact of aerosols on global climate is medium to low, for certain types of aerosols it is even very low (IPCC, 2007). It depends on the vertical distribution and the chemical composition of the aerosols, on the reflectance of the underlying surface, and on the presence and amount of clouds (IPCC, 2007). Aerosols show a large spatial and temporal variability, therefore, the regional impact of aerosols can be quite different. A major gap in our knowledge is the aerosol distribution. Furthermore the non-spherical shape and inhomogeneity of certain types of aerosols introduces difficulties in modeling their optical parameters. Thus the importance of aerosols is only poorly characterized in climate models (Satheesh and Moorthy, 2005). Measurements with advanced lidar systems are crucial as they provide vertical resolved optical properties that help to assess the impact of aerosols on global climate. In this work four major aerosol types of the Earth — Saharan dust, biomass burning, marine aerosols and volcanic aerosols — are investigated. The data were gathered during the field experiments of the Saharan Mineral Dust Experiment (SAMUM) and during special meteorological events over Central Europe. They include the lidar derived optical properties of the different aerosol types, and their vertical distribution above the measurement site. The experimental dataset shall improve and validate modeling of optical properties and aerosol transport. Furthermore they may serve as basis for aerosol climatologies.

## 1.1 Aerosols and climate

Aerosols are small particles and liquid droplets, from about  $0.01 \mu\text{m}$  to hundreds of  $\mu\text{m}$ , suspended in the air. They can have anthropogenic sources, like burning of fossil fuels or alteration of Earth's surface by land use, or they can be produced naturally from dust storms, forest fires, volcanoes and sea spray. The amount of anthropogenic produced aerosols is currently estimated to 10 % of the total amount of aerosols in the atmosphere, mainly concentrated on the northern hemisphere (IPCC, 2007). The majority of the aerosol particles are found in the troposphere, where they have a residence time of a few days to several weeks (Haywood and Boucher, 2000; Raes et al., 2000). Mostly they are washed out by rain. However, aerosols can also be found in the stratosphere: Severe volcanic eruptions like that of Mount Pinatubo, Philippines, in 1991 release large amounts of aerosols into the stratosphere, where they can remain for several months and lead to a cooling of the troposphere (Parker et al., 1996).

Compared to greenhouse gases which are homogeneously mixed in the troposphere, the distribution and amount of tropospheric aerosols are highly variable. Additionally, the impact of aerosols is not limited to one side of the radiation balance, due to their size distribution and chemical composition. They influence the Earth's climate mainly in two ways: *directly* by scattering and absorption of solar and terrestrial radiation and *indirectly* by acting as condensation nuclei. As aerosols can act as cloud condensation nuclei, they change the number concentration of cloud droplets at constant water content, and therewith the albedo of the cloud. This effect is called the *first indirect* aerosol effect (Twomey, 1974). A higher amount of smaller droplets may decrease the precipitation efficiency and thus extend the life time of the cloud (*second indirect* aerosol effect - Albrecht 1989). Absorption of shortwave radiation by strongly absorbing particles can affect tropospheric stability, and influences cloud formation and cloud lifetime (Hansen et al., 1997; Ackermann, 1998). This effect is known as the *semi-direct* effect.

The importance of aerosols can be quantified by the aerosol optical depth (AOD). The AOD is a measure of the attenuation of the incoming solar radiation on its way through the atmosphere due to the presence of aerosols. It is the columnar integrated extinction ( $\alpha_p$ ) by aerosol scattering and absorption.

$$AOD = \int_{z_0}^{z_1} (\alpha_p \cdot dz) \quad (1.1)$$

The fraction of solar radiation that passes through the atmosphere without being scattered or absorbed (Transmission) can be derived from the AOD from

$$T = \exp - \int_{z_0}^{z_1} AOD, \quad (1.2)$$

Thus an AOD of 1 means, that about 2/3 of the solar radiation are scattered and absorbed by atmospheric aerosols and only 1/3 reaches the Earth's surface. Figure 1.1 displays the global seasonal AOD for December-February and June-August 2008. The evaluation is based on measurements of the *Multangle Imaging SpectroRadiometer* (MISR)



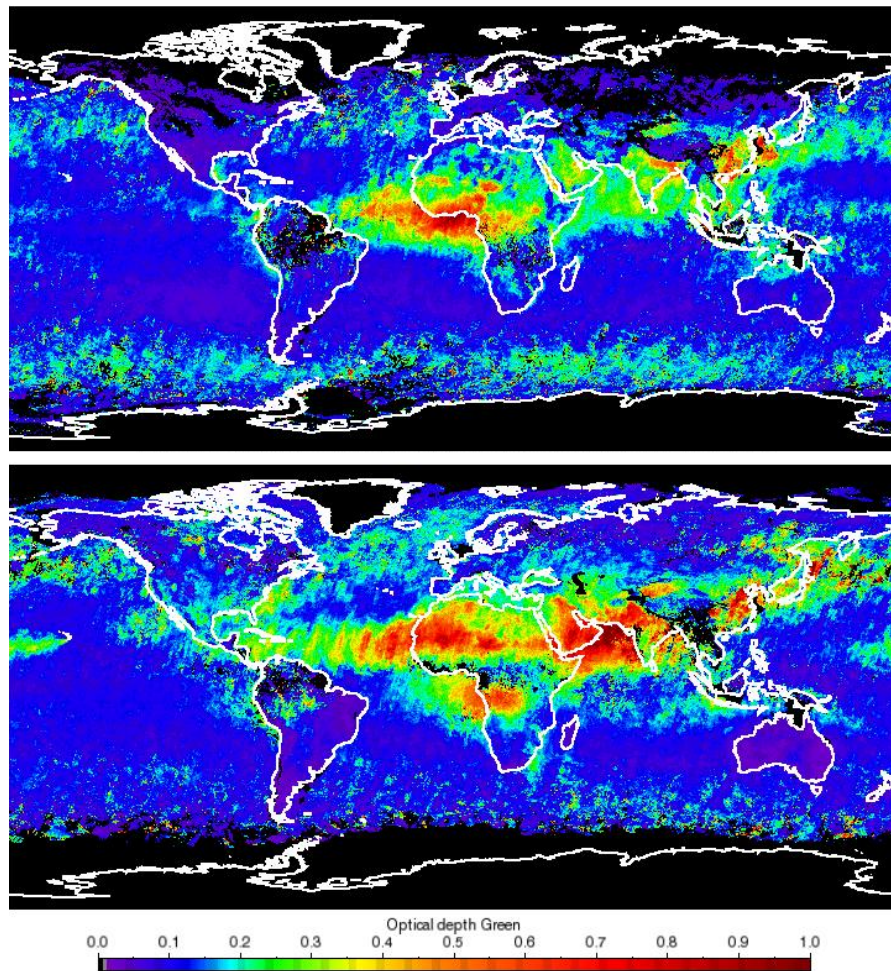


Figure 1.1: Mean of aerosol optical depth (AOD) based on MISR-observations at 555 nm from December-February 2008 (upper plot) and June-August 2008 (lower plot). (<http://eosweb.larc.nasa.gov>)

on NASA's Terra satellite. The blue color indicates areas with low AOD, whereas the red color denotes areas with high AOD. For black areas no data are available. In the winter season high aerosol load, due to forest fires and Saharan dust outbreaks, can be seen in the Gulf of Guinea. In contrast the area of maximum AOD due to forest fires is shifted southward in the summer season. Biomass burning regions are now located over Central Africa and South America. High AOD, caused by Saharan dust storms can be seen over Western Africa. In both seasons the long-range transport of aerosols from Africa over the Atlantic Ocean to Middle and South America is evident. Other areas with high dust load in summertime are Middle and East Asia. Russia is affected by forest fires, mainly in winter time, and East Asia and China show only a weak seasonal cycle of AOD due to industrial pollution.

The direct and indirect interaction of aerosols with global climate is described by the

radiative forcing. It is a measure in  $\text{Wm}^{-2}$  of the influence on the radiation balance of the Earth-atmosphere system by alteration of factors (aerosols or trace gases) that influence the Earth's climate. These factors have the possibility to change the incoming and outgoing energy in the Earth's surface-atmosphere system. The radiative forcing quantifies their influence on the radiation budget and thus their potential on climate change. A negative radiative forcing shows a cooling effect, whereas a positive radiative forcing tends to warm the surface-atmosphere system. The total radiative forcing of all aerosols is estimated to be  $-0.5 \pm 0.4 \text{ Wm}^{-2}$  with a medium to low rate of understanding (IPCC, 2007). However, the understanding of individual types of aerosols is very low and the estimated radiative forcing is more uncertain. As an example, the given radiative forcing of mineral dust in the last IPCC report (2007) is  $-0.1 \pm 0.2 \text{ Wm}^{-2}$ . For biomass burning aerosol it is estimated to be  $+0.03 \pm 0.12 \text{ Wm}^{-2}$ . The current knowledge of the four investigated aerosol types is summarized in the following section.

## 1.2 Selected aerosols of the Earth's atmosphere

### 1.2.1 Desert dust

Mineral dust is one major component of the Earth's atmosphere. With an estimated emission of 1000-2600 Tg per year (Zender et al., 2004; Cakmur et al., 2006) it contributes to the global AOD by 30% (Tegen et al., 1997). The dust emission is assumed to have a significant anthropogenic component mainly originating from agriculture, industrial practices (Prospero et al., 2002) and changes in surface water (Reheis et al., September, 1995). Modeling studies have attempted to constrain the anthropogenic impact on dust emission. Tegen and Fung (1995) suggested about 30 - 50 % contribution from land use. In later studies Tegen et al. (2004) estimated the contribution of land use sources to less than 10%. Mahowald et al. (2004) used the same data as Tegen et al. (2004) but a different model and found a 0 - 50% land use source.

The main source regions of desert dust are limited to the Northern Hemisphere (Prospero et al., 2002), extending from the west coast of North Africa to Middle and East Asia. The largest source region is the Saharan desert. With nine million  $\text{km}^2$  it is the largest desert on Earth. Its contribution to the global annual dust emission is about 50 - 70 % (Washington et al., 2003; Mahowald et al., 2005). As dust can be transported over thousands of kilometers it is not only a regional phenomenon, but has a global climate effect. Dust is exported from the Saharan desert during the whole year. Once lifted in the air, mineral dust can be transported over several thousands of kilometers (Goudie and Middleton, 2001). It can be transported over the Mediterraneans to Central Europe (Ansmann et al., 2003), over the Balkans to Eastern Europe (Papayannis et al., 2008) and over the Atlantic Ocean to the Caribbean (e.g. Prospero and Carlson, 1972; Liu et al., 2008a) and the Amazon region (Ansmann et al., 2009). Figure 1.2 shows an image of the *Moderate Resolution Imaging Spectroradiometer* (MODIS) flying on NASA's Aqua satellite for 29 January 2008. Dust from a heavy dust storm is transported from Western Africa to the

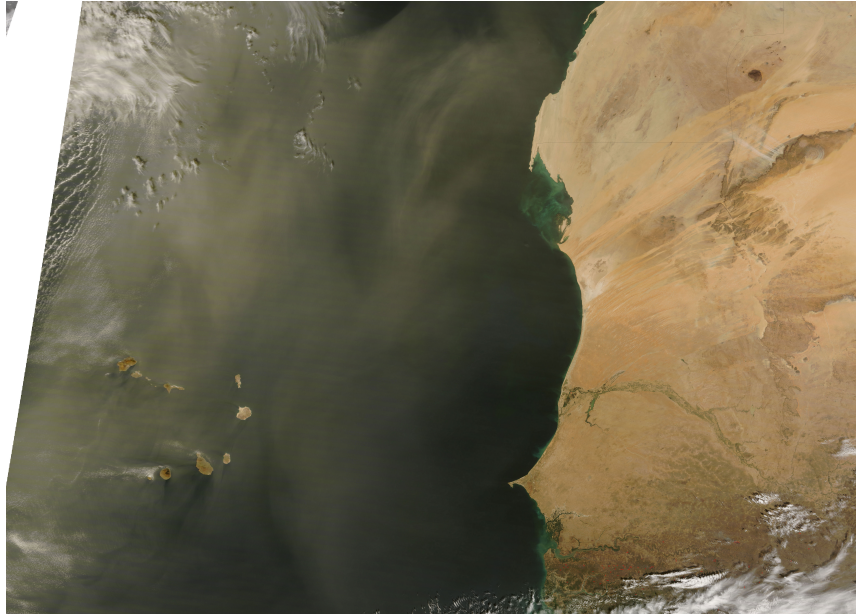


Figure 1.2: Saharan dust storm off the West Coast of Africa - 29 January 2008, (<http://earthobservatory.nasa.gov>)

Atlantic Ocean. High dust loaded air masses (brownish color) can be seen over and north of the Cape Verde Islands.

Dust is expected to influence the atmosphere in different ways. It is expected that Saharan dust influences the generation of Cyclones in the Caribbean (Evan et al., 2006; Wu, 2007) and prevents precipitation over the North Atlantic (Rosenfeld et al., 2001). In the Amazon region the Saharan mineral dust acts as fertilizer (Koren et al., 2006).

The direct aerosol effect of the dust particles is very complex. Due to their large range of size (from about  $0.01\mu m$  to about  $100\mu m$  - Sokolik et al. 2001 and their chemical composition they not only scatter and absorb the incoming solar light, but also have a significant impact on long-wave terrestrial radiation (Tanré et al., 2003). The magnitude and sign of the direct aerosol effect of dust strongly depends on the optical properties, the vertical, horizontal and spatial distribution of the dust plume, as well as on the albedo of the underlying surface (Sokolik and Toon, 1996; Sokolik et al., 2001; Myhre and Stordal, 2001). A further difficulty in radiative transfer models is the strongly irregular shape of mineral dust particles, which prevents the application of classical Mie theory (Mie, 1908).

### 1.2.2 Biomass burning aerosols

Biomass burning describes the burning of living and dead vegetation, including anthropogenic sources, like burning of vegetation for land clearing and land-use, as well as natural induced fires, e.g. from lightnings. The human-induced fraction is estimated to be about 90 % (Andreae, 1991). In Africa more biomass is burned (e.g. forest fires and savannas) on

an annual basis than anywhere else. But first believed as a regional problem of the tropics, global biomass burning turned out to be more extensive than previously thought, and is increasing with time (Levine et al., 1992). So biomass burning is an important component in global climate change.

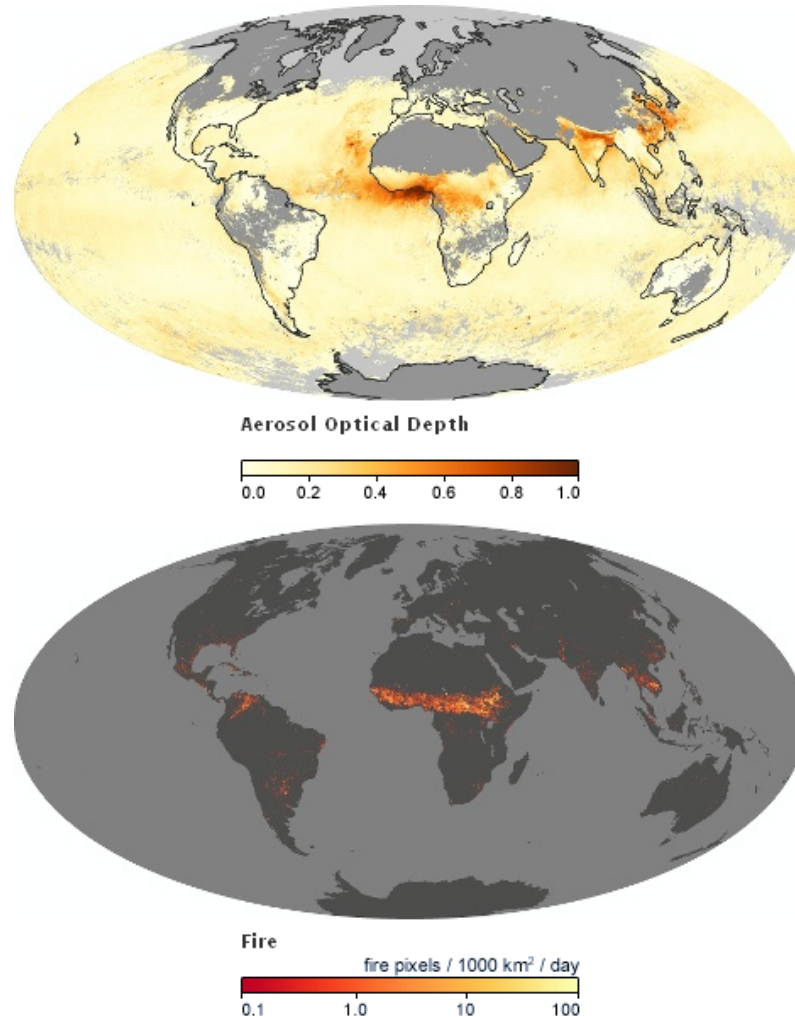


Figure 1.3: Monthly averaged AOD as seen from the MODIS sensor on NASA's Terra satellite (upper panel) and active fires from MODIS sensors on NASA's Terra and Aqua satellites (lower panel) for February 2008. (<http://earthobservatory.nasa.gov/GlobalMaps/>)

Biomass burning releases particles and gases into the atmosphere. The released gases include greenhouse gases (mainly carbon dioxide ( $\text{CO}_2$ ), methane ( $\text{CH}_4$ ), nitrous oxide ( $\text{N}_2\text{O}$ )) that help warm the Earth (positive radiative forcing). It is also one of the largest source for small particles (Reid et al., 2005a), which consists of 5 - 10 % of black carbon (Reid et al., 2005b). Although the contribution of black carbon to the total amount of aerosols is estimated only to 3 - 5% (compared to 21 - 48% of mineral dust) (Tegen et al.,

1997), black carbon is the second strongest contribution to current global warming (Ramanathan and Carmichael, 2008). Some model calculations estimate the global warming due to black carbon to 0.3 - 0.4°C (Jacobson, 2004). However, the estimation of the climate effect has large uncertainties as it strongly depends on the spatial distribution of black carbon, its residence time in the atmosphere, and of its micro-physical and chemical properties (Jacobson, 2001). Black carbon is the most efficient particulate absorber of solar radiation (Menon et al., 2002), causing a cooling of the Earth's surface and a warming of the atmosphere, which effects cloud formation and precipitation. E.g. smoke particles were found to reduce the cloud droplet size (Andreae et al., 2004) and to inhibit precipitation from smoke-infected clouds (Rosenfeld, 1999).

Figure 1.3 shows the monthly averaged AOD (upper part) for February 2008. The palest yellow indicates an AOD of 0.1 (clear sky with maximum visibility), whereas the reddish brown color indicates very hazy conditions (AOD = 1). In the lower part of the plot, fire maps show the location of actively burning fires in February 2008. The colors indicate the number of fires observed within 1000 km<sup>2</sup>. Red areas show one fire per day, orange five fires and the yellow pixels show as many as ten fires. The observations are based on MODIS sensors on NASA's Terra and Aqua satellites. As can be seen, one of the areas with the largest dust load (Central Africa and the Sahel) coincides with high fire activities. But biomass burning also causes high AOD over northern India and in East Asia.

### 1.2.3 Marine aerosols

In addition to mineral dust, sea salt is one major type of aerosols in the atmosphere. Erickson and Duce (1988) estimated the total amount of sea salt emission from ocean to atmosphere to be 1000-3000 Tg per year, Tegen et al. (1997) estimated even 5900 Tg per year. In the last IPCC report a best guess of 3300 Tg per year is given (IPCC, 2007). That means, that the median emission per m<sup>2</sup> ocean surface per year is about 10 g.

Figure 1.4 shows the global annual emission rate for sea salt in 1990, calculated with the *Goddard Chemistry Aerosol Radiation and Transport* (GOCART) model (Chin et al., 2002). The white color denotes no sea salt emission, whereas the red colored areas show the largest amount of sea salt emission. It can be seen, that between 40-60° N and 40-60° S (mid latitude westerly belt) the sea salt emission has its maximum.

Sea salt particles have a large range of sizes from about 0.05 to 10  $\mu\text{m}$ . Their residence time in the atmosphere ranges from a few hours to several days. They are mainly generated by bursting of air bubbles (Blanchard and Syzdek, 1982), which is strongly dependent on wind speed (Monahan, 1968). Sea salt particles are very efficient as cloud condensation nuclei. Thus they do not just scatter the incoming and outgoing light, but have also a strong indirect aerosol effect. A small amount of giant particles can significantly change the stratus-cumulus drizzle production and the cloud albedo (Feingold et al., 1999). Activation of sea-salt particles can significantly increase the number concentration of cloud droplets in marine stratus clouds and therefore enhance the cloud albedo with respect to incoming shortwave radiation (Latham and Smith, 1990), leading to a negative radiative forcing and

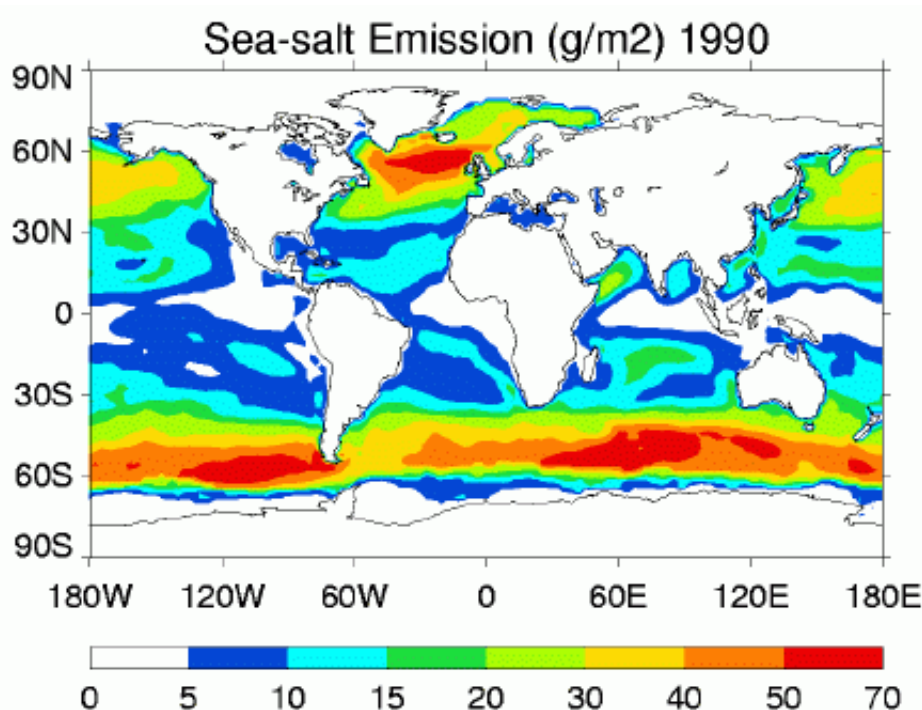


Figure 1.4: Global annual emission rate for sea salt in 1990, calculated with the GOCART model. (<http://acdb-ext.gsfc.nasa.gov/People/Chin/gocartinfo.html>)

therewith to a cooling effect.

#### 1.2.4 Volcanic ash particles

Although the mean annual emission of volcanic aerosols in the atmosphere ( $\approx 5 - 10$  Tg/year of  $\text{SO}_2$  and 20 Tg/yr of fine ash - Mather et al. 2003) is low compared to sea-salt and mineral dust, they can significantly influence climate on continental or even global scale, as they have an influence on the radiation budget of the Earth (Robock, 2000) and the hydrological cycle (Trenberth and Dai, 2007).

Ash particles sediment rapidly in the first days or weeks, whereas sulfur dioxide, especially when injected into the stratosphere can remain for several weeks or even months. Sulfur dioxide converts to sulfuric acid, which condenses rapidly in the stratosphere, and thus has a significant impact on the Earth's climate, as it reflects the shortwave solar radiation and leads to a cooling of the lower atmosphere (negative radiative forcing). As examples, the eruption of Pinatubo (Philippines, 1991) led to a global cooling of the troposphere of 0.5 K to 0.8 K in the following year (Parker et al., 1996). The strongest eruption in modern times, the Tambora (Java, 1815), led to a reduction of the tropospheric temperature of up to 3 K in parts of the northern hemisphere in the subsequent summer (Rampino and Self, 1982). But volcanic particles do not just scatter and absorb radiation, they also mod-

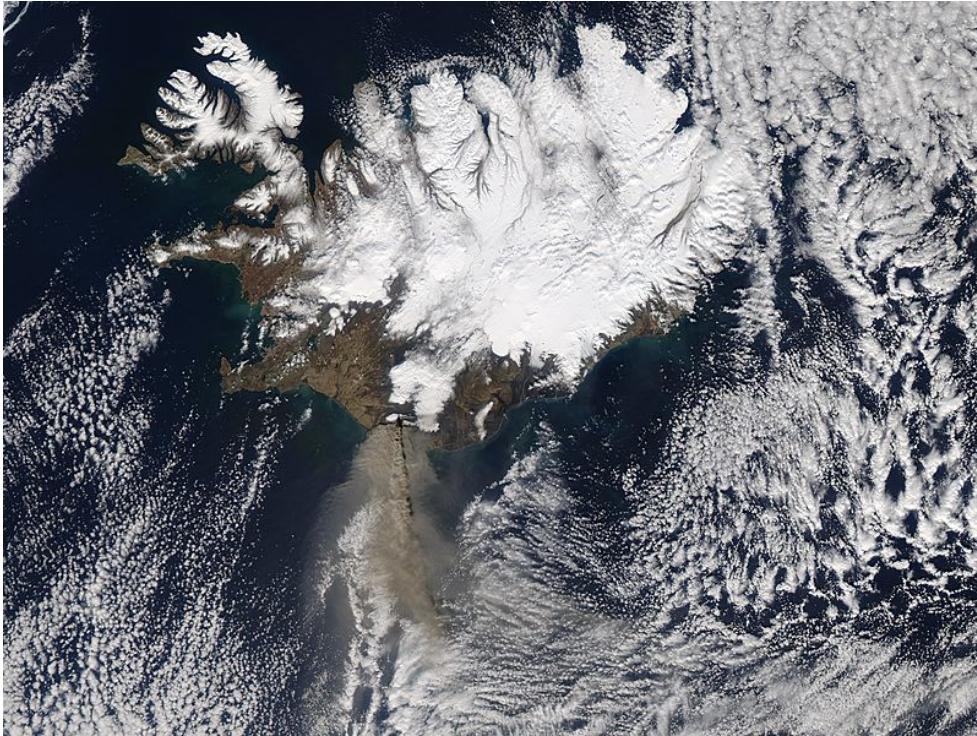


Figure 1.5: Ash plume of the Eyjafjallajökull Volcano, Iceland, as observed with the MODIS sensors on NASA’s Aqua satellite on 17 April 2010 at 13:20 UTC. (<http://rapidfire.sci.gsfc.nasa.gov/gallery/>)

ify cloud cover and cloud radiation properties, as they act as condensation nuclei (Hobbs et al., 1982). Volcanic eruptions also release mineral particles and glass particles into the atmosphere. As these particles have a low melting point and a sharp-edged nature, they are expected to damage aircrafts engines (Casadevall, 1994) when their amount is above a certain threshold. So volcanic eruptions have significant consequences for air traffic and thus a severe economic impact.

Figure 1.5 shows the volcanic ash plume of the Eyjafjallajökull, Iceland, as detected by MODIS sensors on NASA’s Aqua satellite on 17 April 2010. Northern air flow advected the ash plume over Europe, where it influenced air traffic for almost one month.

### 1.3 Benefit of advanced lidar measurements

For a better understanding of the effects of aerosols on the climate system, it is important to get highly accurate information of their optical properties (e.g. extinction coefficient, single scattering albedo and phase function), as well as on their temporal and spatial distribution. Satellite instruments provide a high temporal-resolved global coverage of the aerosol distribution. However, to retrieve aerosol optical properties from passive instruments certain assumptions have to be made, causing errors in the retrieved data products.

Above highly reflecting areas like deserts the analyses are even more uncertain (Sokolik et al., 2001). Furthermore they provide only a low or even no vertical resolution. Active remote sensing with lidar (Light Detection and Ranging) systems offers a high vertical and temporal resolution of measurements and is therefore most appropriate for studies of aerosols. But remote sensing with lidars has only a minor spatial distribution. Therefore the *Cloud-Aerosol Lidar with Orthogonal Polarization* (CALIOP) on board the *Cloud Aerosol Lidar and Infrared Pathfinder Satellite Observations* (CALIPSO) was launched in 2006 (Winker et al., 2007). It provides the vertical and global aerosol distribution, but still has two main deficiencies; CALIOP measures only the backscattered light from the atmosphere. Thus it is not able to directly retrieve the climate efficient extinction coefficient and thus the AOD. For the derivation of the extinction coefficient further assumptions of additional input parameters have to be made. The choice of the correct input parameter is based on an aerosol-feature mask, allocating a certain parameter to the assumed type of aerosol. However, this proceeding can be affected of miss-interpretation and thus lead to large errors in the retrieved AOD (Wandinger et al., 2010). Therefore it is important to have a method that clearly distinguishes between different types of aerosols. Advanced lidar systems, like high spectral resolution lidars (HSRL), or Raman-lidars, can directly retrieve the extinction coefficient without any further assumptions, and provide input parameters for the evaluation of satellite based lidar systems. They also provide informations on optical parameters that can be used for a classification of aerosols (see Chapter 5) and therefore to separate different types of aerosols. Another problem of satellite remote sensing with lidar is the temporal gap between two overflights over the same point. In case of CALIPSO it takes 16 days until the satellite passes over the same ground track again. Observation of local events are therewith difficult or, in some cases, even impossible. Ground-based systems have the opportunity to monitor the development of single events over one point, but do not cover the spatial distribution. Here, combination of satellite remote sensing and networks of advanced lidar systems can fill the gap by coordinated measurements. As an example, the *European Aerosol Research Lidar Network* EARLINET (Boesenberg, 2003) proved its potential to monitor the 4d-distribution of the volcanic ash plume during the eruption of the Eyjafjallajökull in April and May 2010.

## 1.4 Saharan mineral dust experiment

To improve our knowledge of Saharan mineral dust, the Saharan mineral dust experiment, SAMUM, was conducted. Its aim is to characterize the microphysical, chemical and optical properties, as well as the vertical distribution of Saharan dust. SAMUM is a joint project of several German research Institutes and Universities, funded by the German Research Foundation (DFG). The first campaign (SAMUM-1) in May and June 2006 was located in Ouarzazate (1130 m asl, 30.9° N, 6.9° W) and Tinfou (684 m asl, 30.1° N, 5.7° W), Morocco, to measure pure not-aged Saharan dust close to the source. In-situ measurements of microphysical and chemical properties (e.g. Kandler et al., 2009; Weinzierl et al., 2009; Kaaden et al., 2009) as well as analyses of the radiative effects of dust (e.g. Bierwirth et al. 2009),



columnar integrated parameters (e.g. Toledano et al. 2009) and profiles of dust optical properties (e.g. Tesche et al. 2009a; Esselborn et al. 2009; Freudenthaler et al. 2009) were performed during SAMUM-1. The second campaign (SAMUM-2) in January and February 2008 was located at Praia (75 m asl, 14.9° N, -23.5° E), the capital of Cape Verde Island, located in the Atlantic Ocean approximately 570 km west of Senegal. Observations of pure dust at the beginning of the long-range transport across the Atlantic Ocean, as well as of marine aerosols and biomass burning aerosols from Central Africa were made. The findings of SAMUM support the modeling of dust transport and the impact of Saharan dust on the Earth's climate, and shall validate and improve radiative transfer codes for non-spherical particles. Figure 1.6 shows the location of both campaigns.

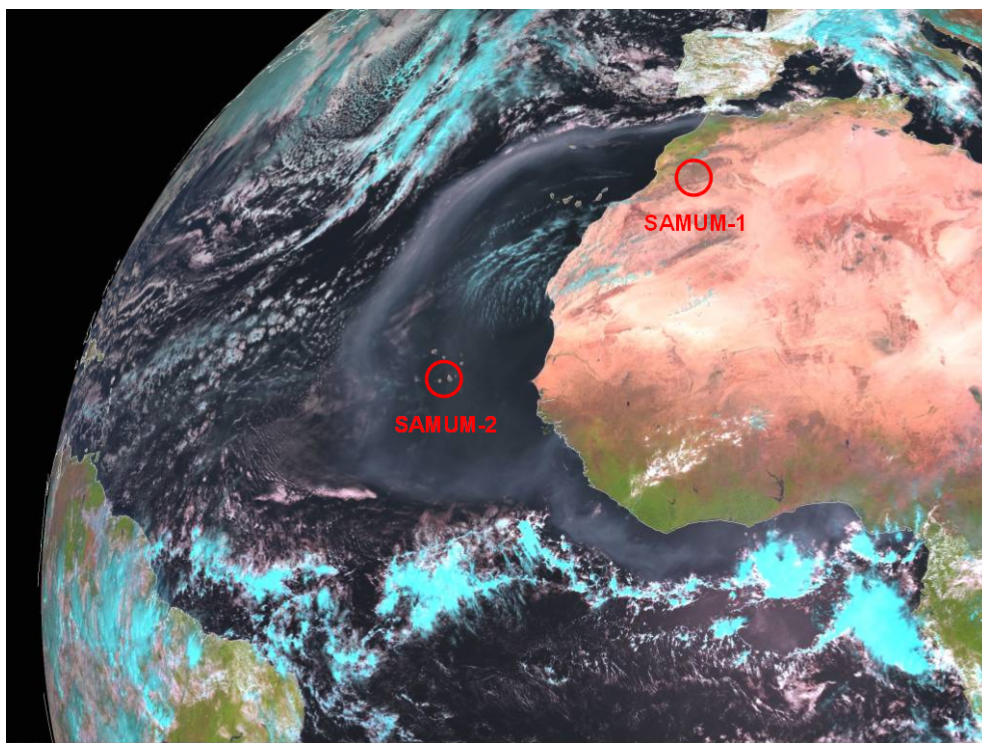


Figure 1.6: Location of the measurement sites of the two campaigns of the SAMUM-Project. Source: EUMETSAT - MSG 6 March 2004

During SAMUM-1 and SAMUM-2 three ground-based Raman- and depolarization lidar systems performed daily measurements, usually for three hours before noon and three hours after sunset, as well as during overpasses of CALIPSO and of the research aircraft FALCON (DLR, Oberpfaffenhofen) with the high spectral resolution lidar (HSRL). The combination of all lidar systems employed during SAMUM allows analyses of the spectral behavior of the optical properties of Saharan dust at multiple wavelengths (Tesche et al., 2009a) and of the particle linear depolarization ratio  $\delta_p$  at four wavelengths (Freudenthaler et al., 2009).

Besides the lidar systems, sun-photometer measurements of a Cimel sun- and sky-photometer of the AERosol RObotic NETwork (AERONET) (Holben et al., 1998) and

the SSARA system of the Meteorological Institute (MIM) of the Ludwig-Maximilians-Universität (LMU), München provided measurements of direct and indirect solar radiances between 340 - 1640 nm (SAMUM-1) and 340 - 1550 nm (SAMUM-2). In both campaigns a variety of in-situ measurements, on board the FALCON aircraft and ground-based, performed analyses of the micro-physical properties (e.g. size distribution and mass concentration) and chemical properties (e.g. chemical composition). Furthermore the spectral absorption of the collected particles and their hygroscopicity was studied. Airborne measurements additionally monitored the horizontal variability of the analyzed layers by means of lidar and in-situ measurements.

## 1.5 Objective and structure of this thesis

In this study the four major aerosol types — desert dust, biomass burning aerosols, marine aerosols and volcanic ash — are investigated based on lidar measurements performed during the field experiments of the SAMUM project and during special meteorological events over Central Europe. The main objective of this thesis is the determination of two parameters, the extinction-to-backscatter ratio (lidar ratio) and the particle linear depolarization ratio, and the examination of their wavelength dependence. Both parameters are intensive properties and therewith only dependent on the aerosol type. Regarding measurements of one or both of these intensive parameters raises several scientific questions:

- Is it possible to discriminate different aerosol types by means of lidar measurements?
- What is the benefit of multi-wavelength depolarization measurements?
- How do the lidar derived optical properties change in aerosol mixtures?
- What else can be learned from the particle linear depolarization ratio?
  - Is it possible to determine the contribution of an individual aerosol type to an aerosol mixture?
  - Does hygroscopicity affect the particle linear depolarization ratio?

Most experimental studies in literature deal with examinations of the particle linear depolarization ratio at one wavelength, mainly at 532 nm. In this study simultaneous measurements of the lidar ratio and the particle linear depolarization ratio at two wavelength are presented. For the first time, dual wavelength depolarization measurements of aged and transported dust, biomass burning aerosols, marine aerosols and volcanic ash are presented. This gives the possibility to study, for the first time, the wavelength dependent changes of the optical properties of Saharan dust during transport. To investigate differences of the optical properties of different aerosol types, and changes of optical properties during transport, a comprehensive error calculation is almost as important as the measurement itself. Therefore an analytical error calculation for the retrieval of the lidar ratio was invented.

This thesis is organized as follows:

Besides the fundamentals of lidar measurements, Chapter 2 describes the two basic methods used for the evaluation of the lidar signals. Furthermore it presents the basis of depolarization measurements and provides an error calculation to determine the uncertainties of the retrieved optical properties. The error calculation not only considers the statistical errors resulting from signal noise, but also includes systematic errors resulting from uncertainties in the input parameters.

The lidar systems, which were used for the measurements relevant for this work are presented in Chapter 3. Altogether measurements of four lidar systems will be presented, however, the measurements of the two lidar systems from the Ludwig-Maximilians-Universität, München, form the backbone of this thesis.

Chapter 4 presents the results of the optical properties of the four basic aerosols types - desert dust, biomass burning aerosols, marine aerosols and volcanic ash. They were derived with the methods described in Chapter 2. For each aerosol type an overview of the overall situation and the main results are presented, additionally the optical properties are retrieved exemplarily on the basis of one case study. The results of the different aerosol types are analyzed related to their spectral behavior and to possible changes during transport. The evaluation and characterization of the optical properties is based on approximately 600 hours of lidar measurements.

In Chapter 5 the results of the lidar measurements are discussed. This discussion includes the relation to former, independent studies of individual results, comparisons with independent measurements and examinations of the previous mentioned scientific questions. Chapter 6 concludes this work with a summary of the results.

## 1.6 External data

For the realization of this study contribution of several persons or organizations were applied. These contributions are summarized in the following. The measurements with the lidar system Bertha during SAMUM-2 were performed from Matthias Tesche. He also analyzed the particle linear depolarization ratio at 710 nm. Dr. Volker Freudenthaler was mainly responsible for the measurements with the MULIS lidar system during SAMUM-2 and during special meteorological events over Central Europe. The analysis of these measurements were one main part of this study. The SSARA sun-photometer measurements during SAMUM-1 were performed from Markus Garhammer. Dr. Carlos Toledano provided the data of the SSARA sun-photometer measurements during SAMUM-2. They were used for the meteorological overview of the measurement situation and for comparisons with the lidar derived optical properties. Sun-photometer measurements of the CIMEL were downloaded from the AERONET web page (<http://aeronet.gsfc.nasa.gov> - PI: Peter Köpke). The HYSPLIT trajectories were calculated with the Hybrid Single particle Lagrangian Integrated Trajectory (HYSPLIT) transport and dispersion model on the READY website (<http://ready.arl.noaa.gov/HYSPLIT.php>). Alexander Schalditz provided the measurements and analyses of in-situ retrieved volume fraction of dust and

marine aerosols during SAMUM, and Dr. Konrad Kandler performed single particle analyses of the volume fractions. These data sets were used for a comparison and validation of lidar derived volume fraction. During SAMUM-2 radiosondes were launched from the Leibniz Institute of Tropospheric Research (IFT), Leipzig usually twice a day. For events over Munich/Maisach radiosondes of the German Weather Service (DWD), launched in Oberschleißheim, were used. They were needed for evaluation of the lidar signals.

# Chapter 2

## Lidar technique

### 2.1 Lidar technique

Lidar (light detection and ranging) is an active remote sensing instrument emitting pulsed laser light into the atmosphere and measuring the returns scattered from particles and molecules. A similar technique to lidar was first used in 1938 (Bureau, 1946) when pulsed light was used for cloud height detection. Since the invention of the laser in 1960 (Maiman, 1960) and especially the Q-switched laser in 1962 (McClung and Hellwarth, 1962) lidar got under rapid development. Already a simple backscatter lidar provides information of the vertical and temporal distribution of aerosols and clouds. Using advanced lidar systems like high-spectral-resolution lidar (HSRL) or Raman lidar systems permits the quantitative examination of the optical properties of aerosols (e.g. Esselborn et al., 2009; Ansmann et al., 1992). With multi-wavelength measurements, information about the spectral behavior of the aerosol particles can be achieved which allow evaluation e.g. of the size distribution and micro-physical properties (Müller et al., 2000). These evaluations are based on Mie theory (Mie, 1908) and therefore limited to spherical particles. Additional measurements of the linear depolarization ratio make it possible to evaluate the micro-physical parameters even for non-spherical particles (Wiegner et al., 2009; Gasteiger et al., 2010).

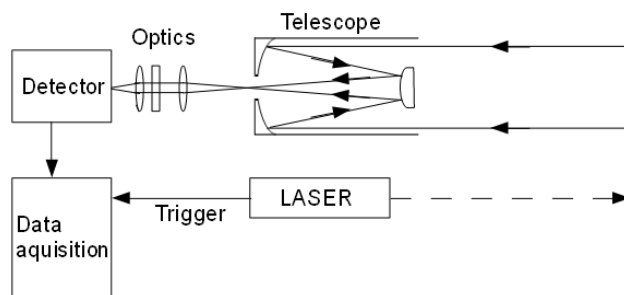


Figure 2.1: Principle setup of a lidar system. (according to Freudenthaler, 2000)

The basic lidar setup is shown in Figure 2.1. The laser generates and emits short pulsed light with specific spectral properties. In modern lidar systems Nd:YAG (Neodym-doped Yttrium-Aluminium-Granat) lasers are frequently used. They emit light in the infrared spectral region at 1064 nm but the widely used frequencies at 532 nm and 355 nm can be achieved by doubling and tripling with nonlinear crystals. Some systems apply a beam expander to reduce the divergence of the beam. The light, sent into the atmosphere, is scattered from particles and molecules. A telescope collects the backscattered photons. It is usually followed by the detection optics, which separates the different wavelengths and specific depolarization states, detected by a series of photomultiplier. These photomultiplier convert the optical signal into an electrical signal, which is stored in a computer. When the laser pulse is shorter as the resolved time, the distance  $r$  of the scattering elements from the lidar system can be obtained from the delay between the laser pulse and the receiving pulse as  $r = ct/2$ , with  $c$  the speed of light and the factor  $1/2$  because the light has to go forth and back. As an example: for a resolved time interval of  $\Delta t$  of 50 ns the corresponding range resolution  $\delta R = c\Delta t/2$  is 7.5 m.

## 2.2 Lidar equation

The lidar equation describes the relationship between the detected signal  $P(\lambda, r)$  at wavelength  $\lambda$  from distance  $r$ , the transmission of the atmosphere and the scattering processes in the atmosphere at an scattering angle of  $\phi = 180^\circ$ , and the system parameters. In its simplest form it can be written as

$$P(\lambda, r) = \frac{C_L O(r)}{r^2} \beta(\lambda, r) T^2(\lambda) \quad (2.1)$$

$C_L$  is the system constant, including all system parameters, like area of the receiver optics, transmission of the optical setup, and energy of the laser pulse. The overlap function  $O$  describes the range-dependent measurement geometry. In principle it is hardly determinable in praxis, but it is important to know the range at which the full scattering volume is inside the field of view of the telescope ( $O = 1$ , Figure 2.2). These two factors are completely controlled by the lidar setup, whereas the last two factors provide the information of the atmosphere. The total backscatter coefficient  $\beta = \beta_p + \beta_m$  consists of the backscatter coefficient of particles  $\beta_p$  and of molecules  $\beta_m$ , and describes the ability to scatter light back at  $\phi = 180^\circ$ .  $T$  is the transmission term and describes the attenuation of the laser light from the laser to distance  $r$  and back.  $T$  is calculated, following the law of Lambert-Beer, from the integral over the total extinction coefficient  $\alpha$ .

$$T(\lambda) = \exp \left\{ - \int_0^r \alpha(\lambda, r') dr' \right\} \quad (2.2)$$

Like  $\beta$ , the total extinction coefficient consists of a particle and a molecular contribution ( $\alpha = \alpha_p + \alpha_m$ ), with  $\alpha_p$  the particle extinction coefficient and  $\alpha_m$  the molecular extinction coefficient.

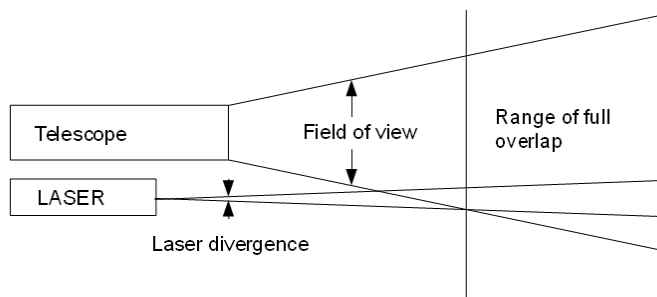


Figure 2.2: Schematic display of the overlap function.

## 2.3 Inversion of the lidar equation

### 2.3.1 Klett- / Fernald-Algorithm

A method with a high height resolution is presented by Klett, 1981. This method only uses the elastic backscattered signals with high signal-to-noise ratio. However, as input parameter the extinction-to-backscatter ratio (lidar ratio)  $S_p$  is needed.

The lidar equation for the elastic backscattered signal is

$$P(\lambda_0, r) = \frac{C_{\lambda_0}}{r^2} \cdot \beta(\lambda_0, r) \cdot \exp\left(-2 \int_0^r (\alpha_p(\lambda_0, r') + \alpha_m(\lambda_0, r')) dr'\right) \quad (2.3)$$

with  $P(\lambda_0, r)$  the power received at the laser wavelength  $\lambda_0$  from range  $r$ .  $C_{\lambda_0}$  is the system constant and denotes all system parameters of the elastic optics.

Equation 2.3 consists of four unknown parameters, the backscatter coefficient of particles and molecules  $\beta_p$  and  $\beta_m$ , and the extinction coefficient of particles and molecules  $\alpha_p$  and  $\alpha_m$ . As  $\alpha_m$  can be calculated using temperature and pressure profiles of radiosonde measurements, and  $\beta_m$  can be derived from

$$\beta_m = \frac{3}{8\pi} \alpha_m = \frac{1}{S_m} \alpha_m \quad (2.4)$$

the number of unknown parameters can be reduced to two.  $S_m$  is the lidar ratio of molecules. With the lidar ratio of particles,  $S_p$ , retrieved e.g. from Raman measurements (see section 2.3.2) or taken from literature, e.g. OPAC (Hess et al., 1998), assuming a realistic aerosol type, only one unknown parameter remains and the equation (2.3) can in principle be solved.

$$P(r)r^2 = (\beta_p + \beta_m) \exp \left\{ +2 \int_{r_0}^r (S_p(r') - S_m(r')) \beta_m(r') dr' \right\} \\ \cdot \exp \left\{ -2 \int_{r_0}^r S_p(r') (\beta_m(r') + \beta_p(r')) dr' \right\} \quad (2.5)$$

The substitution

$$Z(r) = P(r)r^2 \exp \left\{ -2 \int_{r_0}^r (S_p(r') - S_m(r')) \beta_m(r') \right\} \quad (2.6)$$

and the differentiation of the natural logarithm of equation 2.6 result in a Riccati differential equation (Klett, 1981, 1985)

$$\frac{\partial(\beta_m + \beta_p)}{\partial r} = \frac{\partial \ln[Z(r)]}{\partial r} (\beta_m(r) + \beta_p(r)) + 2S_p(r) (\beta_m(r) + \beta_p(r))^2 \quad (2.7)$$

One solution of equation 2.7 is

$$\beta_p = \frac{Z(r)}{\frac{Z(r_0)}{(\beta_m(r_0) + \beta_p(r_0))} - 2 \int_{r_0}^r \frac{Z(r')}{S_p(r')} dr'} \quad (2.8)$$

for  $r > r_0$ . The initial values at  $r_0$  have to be known. In principle they can be estimated from visibility, but it has to be kept in mind that the full overlap of lidar system normally occurs at a few hundred meters above ground.

For increasing  $r$  the denominator decreases and can even get negative for wrong initial values or lidar ratios. Thus the algorithm is numerical instable. The exchange of the integration limits ( $r < r_0$ ) (Fernald, 1984; Klett, 1985) leads to a stable solution, relatively insensitive to wrong initial values or lidar ratios.



$$\beta_p = \frac{Z(r)}{\frac{Z(r_0)}{(\beta_m(r_0) + \beta_p(r_0))} + 2 \int_{r_0}^r \frac{Z(r')}{S_p(r')} dr'} \quad (2.9)$$

for  $r < r_0$ . As initial values the well known values (Rayleigh) of an assumed aerosol free region in the upper troposphere can be used.

Finally,  $\alpha_p$  can be calculated using the lidar ratio for the assumed aerosol type or directly measured with the Raman method.

$$\alpha_p = S_p \cdot \beta_p \quad (2.10)$$

### 2.3.2 Raman method

When light is scattered from molecules, most photons are elastically backscattered. That means they have the same wavelength as the incident photons. However a small fraction of the incident light causes changes of the electronic energy of the molecules and the photons are backscattered with a wavelength different, and usually smaller, than the incident photons. The inelastic backscattered light is only affected by aerosol extinction and not by aerosol scattering, therefore it can be used to determine the aerosol extinction. The method proposed by Ansmann et al. (1992) is based on simultaneous measurements of the elastic and inelastic ( $N_2$  Raman-shifted) wavelength, which allow an independent determination of the particle extinction coefficient  $\alpha_p$  and the particle backscatter coefficient  $\beta_p$ , and thus of the extinction-to-backscatter ratio (lidar ratio)  $S_p$  (Ansmann et al., 1992). In this work  $S_p$  at 355 nm and 532 nm are determined. Thus signal pairs of elastically and inelastically backscattered light at 355/387 nm and 532/607 nm are used.

The lidar equation for the elastic backscattered signal  $P(\lambda_0, r)$  is introduced in the previous section 2.3. The lidar equation for the inelastic  $N_2$  Raman-shifted wavelength is

$$P(\lambda_R, r) = \frac{C_{\lambda_R}}{r^2} \cdot \frac{N \cdot d\sigma(180^\circ)}{d\Omega} \exp\left(-\int_0^r (\alpha_p(\lambda_R, r') + \alpha_m(\lambda_R, r') + \alpha_p(\lambda_0, r') + \alpha_m(\lambda_0, r')) dr'\right) \quad (2.11)$$

where  $P(\lambda_R, r)$  is the power received at the  $N_2$  Raman-shifted wavelength  $\lambda_R$  at range  $r$ , respectively.  $C_{\lambda_R}$  denotes all system parameters of the inelastic receiving optics.  $N$  is the number density of nitrogen molecules,  $d\sigma_{180^\circ}/d\Omega$  is the Raman scattering cross section at  $180^\circ$ . Again,  $\beta_p$  and  $\beta_m$  are the particle and molecular backscatter coefficients and  $\alpha_p$  and  $\alpha_m$  the particle and molecular extinction coefficients.

As the molecular density of nitrogen can be calculated from radiosond data,  $\alpha_p$  can be directly retrieved from the measurements of the  $N_2$  Raman-shifted wavelength.

$$\alpha_p(\lambda_0, r) = \frac{\frac{d}{dr} \left[ \ln \frac{N(r)}{P(\lambda_R, r)r^2} \right] - \alpha_m(\lambda_0, r) - \alpha_m(\lambda_R, r)}{1 + \left( \frac{\lambda_0}{\lambda_R} \right)^\kappa} \quad (2.12)$$

$\kappa$  is the Angström Exponent, which characterizes the wavelength dependence of the particle extinction coefficient. For particles with large diameters compared to the measurement wavelength  $\kappa = 0$ , whereas for particles with diameters in the range of the measurement wavelength  $\kappa \approx 1$ . As  $\alpha_m(\lambda_0) = Const \cdot N(r)$ , Equation 2.12 can be written as

$$\alpha_p(\lambda_0, r) = \frac{\frac{d}{dr} \left[ \ln \frac{\alpha_m(\lambda_0, r)}{P(\lambda_R, r)r^2} \right] - \alpha_m(\lambda_0, r) - \alpha_m(\lambda_R, r)}{1 + \left( \frac{\lambda_0}{\lambda_R} \right)^\kappa} \quad (2.13)$$

When using the elastic signals and the Raman-shifted signals, the particle backscatter coefficient  $\beta_p$  can be determined from

$$\beta_p(\lambda_0, r) = [Q(r)E(r)R(r_0) - 1] \beta_m(\lambda_0, r) \quad (2.14)$$

using the quotient of the measured signals at height  $r$  and a reference height  $r_0$ ,

$$Q = \frac{P(\lambda_0, r)P(\lambda_R, r_0)}{P(\lambda_0, r_0)P(\lambda_R, r)} \quad (2.15)$$

with the signal pairs

$$\begin{aligned} \frac{P(\lambda_0, r)}{P(\lambda_0, r_0)} &= \frac{\beta_p(\lambda_0, r) + \beta_m(\lambda_0, r)}{\beta_p(\lambda_0, r_0) + \beta_m(\lambda_0, r_0)} \left( \frac{r_0}{r} \right)^2 \\ &\quad \exp \left\{ -2 \int_{r_0}^r (\alpha_p(\lambda_0, r') + \alpha_m(\lambda_0, r')) dr' \right\} \end{aligned} \quad (2.16)$$

and

$$\begin{aligned} \frac{P(\lambda_R, r_0)}{P(\lambda_R, r)} &= \frac{\beta_p(\lambda_0, r) + \beta_m(\lambda_0, r)}{\beta_p(\lambda_0, r_0) + \beta_m(\lambda_0, r_0)} \left( \frac{r}{r_0} \right)^2 \\ &\quad \exp \left\{ + \int_{r_0}^r (\alpha_p(\lambda_0, r') + \alpha_m(\lambda_0, r') + \alpha_p(\lambda_R, r') + \alpha_m(\lambda_R, r')) dr' \right\} \end{aligned} \quad (2.17)$$

It follows

$$\begin{aligned} Q(r) &= \frac{\beta_p(\lambda_0, r) + \beta_m(\lambda_0, r)}{\beta_p(\lambda_0, r_0) + \beta_m(\lambda_0, r_0)} \frac{\beta_m(\lambda_0, r_0)}{\beta_m(\lambda_0, r)} \\ &\quad \frac{\exp \left\{ - \int_{r_0}^r (\alpha_p(\lambda_0, r') + \alpha_m(\lambda_0, r')) \right\}}{\exp \left\{ - \int_{r_0}^r (\alpha_p(\lambda_R, r') + \alpha_m(\lambda_R, r')) \right\}} \end{aligned} \quad (2.18)$$

With the substitution  $E(r)$

$$E(r) = \frac{\exp \left\{ - \int_{r_0}^r (\alpha_p(\lambda_0, r') + \alpha_m(\lambda_0, r')) \right\}}{\exp \left\{ - \int_{r_0}^r (\alpha_p(\lambda_R, r') + \alpha_m(\lambda_R, r')) \right\}} \quad (2.19)$$

and the backscatter ratio

$$R_0 = \frac{\beta_m(\lambda_0, r_0) + \beta_p(\lambda_0, r_0)}{\beta_m(\lambda_0, r_0)} \quad (2.20)$$

at the reference height  $r_0$ .

With the profiles of  $\alpha_p$  and  $\beta_p$  retrieved from equation 2.13 and 2.14 the lidar ratio  $S_p$

$$S_p(\lambda_0, r) = \frac{\alpha_p(\lambda_0, r)}{\beta_p(\lambda_0, r)} \quad (2.21)$$

can be obtained.

The signal-to-noise-ratios of the signals of the Raman-channels, i.e., 387 nm and 607 nm, is low, thus smoothing of the lidar signals is required. Typically, smoothing of the order of several hundreds of meters is adequate. As a consequence, the vertical resolution of the retrievals is significantly reduced compared to the raw signals.

## 2.4 Depolarization

### 2.4.1 Polarization lidar method

The linear depolarization ratio is defined as the ratio of the cross- and co-polarized backscattered light with respect to the plane of polarization of the transmitted linearly polarized laser beam. Both components are separated by a polarizing beam-splitter cube (PBS). It splits the incident beam into two beams of orthogonal planes of polarization. However, for many common PBS the separation is not perfect. Thus one or both output beams contain a mixture of polarization states.

Analog to the lidar equation (Equation 2.1) the powers of the cross- and co-polarized signals before the PBS can be expressed as

$$P_{\parallel} = \frac{C_{\parallel}}{r^2} \beta_{\parallel} T^2 \quad (2.22)$$

and

$$P_{\perp} = \frac{C_{\perp}}{r^2} \beta_{\perp} T^2 \quad (2.23)$$

with the parallel- ( $\beta_{\parallel}$ ) and cross-polarized ( $\beta_{\perp}$ ) component of the total backscatter coefficient  $\beta$ , the system constants (including the telescope aperture and the laser power)  $C_{\parallel}$  and  $C_{\perp}$ , and the atmospheric transmittance  $T^2$ .

In praxis the determination of the signals described in equations 2.22 and 2.23 is technically difficult and therefore subject to uncertainties. One reason is that the PBS might be misaligned with respect to the plane of laser polarization under an angle  $\varphi$  (see Fig. 2.3). Thus the power components with respect to the plane of the PBS are

$$P_p = P_{\parallel} \cos^2(\varphi) + P_{\perp} \sin^2(\varphi) \quad (2.24)$$

and

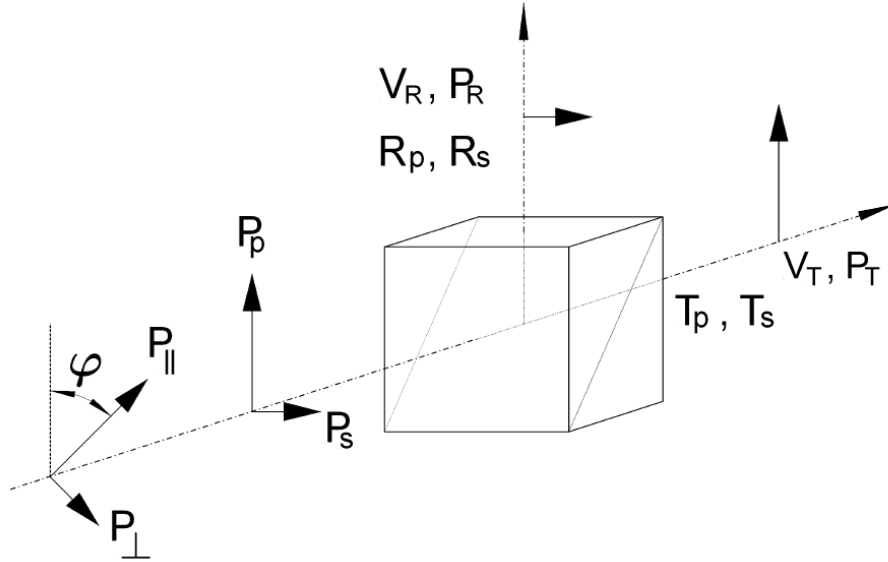


Figure 2.3: Signal power components in a receiver of a depolarization lidar with a polarizing beam-splitter cube with reflectivity  $R_p$  and  $R_s$  and transmittances  $T_p$  and  $T_s$  for linearly polarized light parallel (p) and perpendicular (s) to the incident plane of the polarizing beam-splitter.  $P_R$  and  $P_T$  are the measured quantities in the reflected and transmitted path, respectively, and  $V_R$  and  $V_T$  are the corresponding amplification factors including the optical transmittances. - Plot from Freudenthaler et al., 2009

$$P_s = P_{\parallel} \sin^2(\varphi) + P_{\perp} \cos^2(\varphi) \quad (2.25)$$

$\varphi$  is the angle between the plane of polarization of the laser beam and the plane of the PBS, it is  $\varphi = 0^\circ$  when the co-polarized signal  $P_{\parallel}$  is measured in the transmitted path and  $\varphi = 90^\circ$  when it is measured in the reflected path. Regarding the different optical transmittances and electronic amplification of each channel (with  $V_R$  and  $V_T$  the amplification factors resulting from the different system constants of the two detector optics), the components of the total reflected ( $P_R$ ) and total transmitted ( $P_T$ ) power, that are actually measured behind the PBS are

$$P_R = [P_p(\varphi)R_p + P_s(\varphi)R_s]V_R \quad (2.26)$$

and

$$P_T = [P_p(\varphi)T_p + P_s(\varphi)T_s]V_T \quad (2.27)$$

with reflectivities  $R_p$  and  $R_s$  and transmittances  $T_p$  and  $T_s$  of the PBS, resulting from insufficient separation of both planes of polarization. In the following the signal ratio  $\delta^* = P_R(\varphi)/P_T(\varphi)$  and a relative amplification factor  $V = V_R/V_T$  are used.

### Volume linear depolarization ratio

In a first step the volume linear depolarization ratio  $\delta_v$  is calculated. It describes the polarization ratio of the total backscattered light from molecules and aerosols. It is increasing with increasing amount of non-spherical particles.  $\delta_v$  is the ratio between the cross- and co-polarized signals

$$\delta_v = \frac{P_{\perp}}{P_{\parallel}} = \frac{P_s}{P_p}, \varphi = 0^{\circ} \quad (2.28)$$

As for a commercial PBS  $R_s$  is closer to 1 than  $T_p$ , the high parallel signal is detected in the reflected branch of the PBS ( $\varphi = 90^{\circ}$ ) to reduce cross-talk.

$$\delta_v = \frac{P_{\perp}}{P_{\parallel}} = \frac{P_p}{P_s}, \varphi = 90^{\circ} \quad (2.29)$$

It follows

$$\delta_v = \frac{P_p}{P_s} = \frac{R_s - \frac{\delta^*}{V} T_s}{\frac{\delta^*}{V} T_p - R_p} \quad (2.30)$$

as for the measurements of  $\delta$  additional polarizing filters were used behind the PBS to suppress cross-talk ( $T_s = R_p = 0$ ) equation 2.30 is reduced to

$$\delta_v = \frac{P_{\parallel}}{P_{\perp}} = V \frac{P_R}{P_T} \quad (2.31)$$

The relative amplification factor  $V$  has to be determined from additional measurements (see Section 2.4.2).

### Particle linear depolarization ratio

From  $\delta_v$  the particle linear depolarization ratio  $\delta_p$  can be calculated. It describes the linear depolarization ratio resulting only from aerosols. It is an intensive property of aerosols and aerosol mixtures, and provides information about the shape of the aerosols.  $\delta_p$  can be calculated according to Biele et al. (2000)

$$\delta_p = \frac{(1 + \delta_m)R - (1 + \delta_v)\delta_m}{(1 + \delta_m)\delta_v R - (1 + \delta_v)} \quad (2.32)$$

with the backscatter ratio  $R$

$$R = \frac{\beta_m + \beta_p}{\beta_m} \quad (2.33)$$

and the molecular linear depolarization ratio  $\delta_m$ , resulting only from molecules. It can be calculated with high accuracy (Behrendt and Nakamura, 2002).

### 2.4.2 Depolarization calibration

The relative amplification factor  $V = V_R/V_T$  can be retrieved from a calibration measurement using equations 2.28, 2.26 and 2.27.

$$V = \frac{((1 + \delta_v \tan^2(\varphi)) T_p) + (\tan^2(\varphi) + \delta_v) T_s \frac{P_R(\varphi)}{P_T(\varphi)}}{((1 + \delta_v \tan^2(\varphi)) R_p) + (\tan^2(\varphi) + \delta_v) R_s \frac{P_R(\varphi)}{P_T(\varphi)}} \quad (2.34)$$

In the following three methods to determine  $V$  are presented and shortly discussed.

#### 0°-calibration

For  $\varphi=0^\circ$  it follows

$$V = \frac{T_p + \delta_v T_s \frac{P_R}{P_T}(0^\circ)}{R_p + \delta_v R_s \frac{P_R}{P_T}(0^\circ)} \quad (2.35)$$

If  $\delta_v$  is known in a certain range of the lidar signal (e.g. in the free troposphere where  $\delta_v=\delta_m$ ),  $V$  can be determined from a regular measurement. However, this method suffers from severe error sources. Already a small amount of depolarizing aerosols in the assumed aerosol free region leads to large errors. Second, the signal-to-noise ratio in the calibration range is insufficient for accurate analysis. Furthermore, especially for small cross-polarized

signals, the uncertainties in  $T_p$  can result in large errors. And fourth, the measured  $\delta_m$  depends on the bandwidth of the chosen interference filters.

Other calibration methods use the fact, that  $P_R = P_T$  at  $\varphi=45^\circ$ .

### 45°-calibration

For  $\varphi=45^\circ$  or  $\varphi=\pm 45^\circ$  it follows

$$V = \frac{T_p + T_s}{R_p + R_s} \frac{P_R}{P_T} (\pm 45^\circ) \quad (2.36)$$

This method is independent of  $\delta_v$ , however already an error of  $1^\circ$  from  $\varphi=\pm 45^\circ$  leads to large errors in  $V$ . The polarization plane of the laser is difficult to measure with this high accuracy and therefore a sufficient alignment of the PBS with respect to the polarization plane of the laser is difficult to achieve.

### $\pm 45^\circ$ -calibration

Freudenthaler et al. (2009) showed that two subsequent calibration measurements at  $90^\circ$  difference, that is  $\varphi = +45^\circ + \gamma$  and  $\varphi = -45^\circ + \gamma$ , compensate the error occurred of a possible misalignment ( $\gamma$ ) of the PBS with respect to the laser polarization plane over a large range. Therefore this method is the most accurate one.

$$V = \frac{T_p + T_s}{R_p + R_s} \sqrt{\frac{P_R}{P_T} (+45^\circ) \cdot \frac{P_R}{P_T} (-45^\circ)} \quad (2.37)$$

## 2.5 Error calculation

### 2.5.1 Error of the lidar ratio

For the determination of optical particles from measurements the assessment of the uncertainties is almost as important as the measurement itself. In this work an analytical method to determine the errors of  $S_p$  was developed. As  $S_p$  is the ratio of the extinction coefficient  $\alpha_p$  and of the backscatter coefficient  $\beta_p$ , the errors of these two parameters must be assessed first. Both are retrieved according to the Raman-methodology (Section 2.3.2). In this context, the errors of the lidar signals must be calculated, because they contribute



to the errors of  $\alpha_p$  and  $\beta_p$ . The systematical and statistical errors are calculated separately. The latter is primarily governed by the noise of the involved lidar signals, whereas the systematical errors result from uncertainties of the input parameters of the retrievals.

For the sake of brevity  $f_p$  and  $f_m$  are defined

$$f_p = \left(\frac{\lambda_0}{\lambda_R}\right)^\kappa \quad (2.38)$$

and

$$f_m = \left(\frac{\lambda_0}{\lambda_R}\right)^{4.085} \quad (2.39)$$

with  $\lambda_0$  being the laser wavelength,  $\lambda_R$  the  $N_2$ -Raman shifted wavelength, and  $\kappa$  the Angström exponent. 4.085 denotes the wavelength dependence of Rayleigh, considering a mean correction factor of  $k=0.085$  due to polarizability and a resulting wavelength dependence of the refractive index of molecules.

In the following  $X = Pr^2$  is used. Equation 2.13 can be rewritten as

$$\alpha_p(\lambda_0, r) = (1+f_p^{-1}) \cdot \left\{ \frac{1}{\alpha_m(\lambda_0, r)} \underbrace{\frac{d}{dr}\alpha_m(\lambda_0, r)}_{C_a} - \frac{1}{X(\lambda_R, r)} \underbrace{\frac{d}{dr}X(\lambda_R, r)}_{C_x} - (\alpha_m(\lambda_0, r)(1+f_m)) \right\} \quad (2.40)$$

From Equation 2.40 it is clear, that errors of  $f_p$ ,  $C_x$ ,  $C_a$ ,  $\alpha_m$ , and  $X$  can contribute to the systematical and to the statistical error of  $\alpha_p$ . The systematical error  $\Delta\alpha_p^{yst}$  is assessed according to

$$\Delta\alpha_p^{yst}(\lambda_0, r) = \left| \frac{\partial\alpha_p(\lambda_0, r)}{\partial f_p(\lambda_0, r)} \Delta f_p(\lambda_0, r) \right| + \left| \frac{\partial\alpha_p(\lambda_0, r)}{\partial\alpha_m(\lambda_0, r)} \Delta\alpha_m(\lambda_0, r) \right| \quad (2.41)$$

A systematical error of the lidar signals is not assumed, so no term with  $\Delta X$  appears in Equation 2.41. The same is assumed for the derivatives of the range-corrected signal and of  $\alpha_m$ ,  $C_x$  and  $C_a$ , i.e., the slopes of the corresponding least-square fits. The remaining partial derivatives in Equation 2.40 can be calculated straight forward. More critical is the assessment of the uncertainties of the input parameters.  $f_p$  is governed by the uncertainty of the Angström exponent  $\kappa$ . The exponent  $\kappa$  can either be taken from retrievals based

on co-located sun-photometer measurements or from literature, e.g. OPAC (Hess et al., 1998), assuming a realistic aerosol type. As an example, for Saharan dust  $\kappa=0.2$  and  $\Delta\kappa=0.01$  was used based on measurements during SAMUM-1. This translates to  $\Delta f_p \approx 0.01$ .  $\Delta a_m$  denotes the uncertainty, resulting from differences in time and space between the radiosonde ascent and the lidar measurement. Based on long-term studies for Munich,  $\Delta a_m = 0.02a_m$  is assumed.

The statistical error can be derived as follows:

$$\Delta\alpha_p^{stat}(\lambda_0, r) = \sqrt{\left(\frac{\partial\alpha_p(\lambda_0, r)}{\partial Pr^2(\lambda_R, r)}\Delta Pr^2(\lambda_R, r)\right)^2 + \left(\frac{\partial\alpha_p(\lambda_0, r)}{\partial C_x(r)}\Delta C_x^{stat}(r)\right)^2} \quad (2.42)$$

The first term on the right of Equation 2.42 is related to the signal noise, and is calculated as described in the Appendix. The second term of Equation 2.42 describes the statistical error of the used least-square fit  $C_x$ , and is inherently calculated by the fit-algorithm. Systematical errors in the Angström coefficient or in the molecular extinction coefficient do not contribute to the statistical error.

The backscatter coefficient  $\beta$  is derived according to Equations 2.14 to 2.20. In first approximation it is assumed that the lidar signals  $P(\lambda_0, r)$  and  $P(\lambda_R, r)$  have no systematical error. Furthermore, it is assumed that errors of the extinction coefficients  $\Delta\alpha_m$  and  $\Delta\alpha_p$  and the Angström exponent  $\kappa$  can be neglected. For the error calculation of  $\beta_p$  it is assumed in first approximation that  $\Delta\alpha_m$  and  $\Delta\alpha_p$ ,  $P(\lambda_0, r)$  and  $P(\lambda_R, r)$  do not have a systematical error. Thus the systematical error of  $\beta_p$  can be accessed from

$$\begin{aligned} \Delta\beta_p^{syst}(\lambda_0, r) &= \left| \frac{\partial\beta_p(\lambda_0, r)}{\partial R(\lambda_0, r_0)}\Delta R(\lambda_0, r_0) \right| + \left| \frac{\partial\beta_p(\lambda_0, r)}{\partial\beta_m(\lambda_0, r)}\Delta\beta_m(\lambda_0, r) \right| \\ &= \left| (\beta_p(\lambda_0, r) + \beta_m(\lambda_0, r)) \frac{\Delta R(\lambda_0, r_0)}{R(\lambda_0, r_0)} \right| + \left| \beta_p(\lambda_0, r) \frac{\Delta\beta_m(\lambda_0, r)}{\beta_m(\lambda_0, r)} \right| \quad (2.43) \end{aligned}$$

The most significant contribution to the systematical error of the particle backscatter coefficient is the uncertainty of the scattering ratio at the reference range  $R(\lambda_0, r_0)$ .

For the statistical error of  $\beta_p$ , the noise of the measured signals at both wavelengths is considered

$$\begin{aligned} \Delta\beta_p^{stat}(\lambda_0, r) = & \sqrt{\left(\frac{\partial\beta_p(\lambda_0, r)}{\partial P(\lambda_0, r)}\Delta P(\lambda_0, r)\right)^2 + \left(\frac{\partial\beta_p(\lambda_0, r)}{\partial P(\lambda_0, r_0)}\Delta P(\lambda_0, r_0)\right)^2} \\ & + \left(\frac{\partial\beta_p(\lambda_0, r)}{\partial P(\lambda_R, r)}\Delta P(\lambda_R, r)\right)^2 + \left(\frac{\partial\beta_p(\lambda_0, r)}{\partial P(\lambda_R, r_0)}\Delta P(\lambda_R, r_0)\right)^2 \end{aligned} \quad (2.44)$$

This can be written as

$$\begin{aligned} \Delta\beta_p^{stat}(\lambda_0, r) = & Q(r) \cdot E(r) \cdot R(\lambda_0, r_0) \cdot \beta_m(\lambda_0, r) \\ & \cdot \sqrt{\left(\frac{\Delta P(\lambda_0, r)}{P(\lambda_0, r)}\right)^2 + \left(\frac{\Delta P(\lambda_0, r_0)}{P(\lambda_0, r_0)}\right)^2 + \left(\frac{\Delta P(\lambda_R, r)}{P(\lambda_R, r)}\right)^2 + \left(\frac{\Delta P(\lambda_R, r_0)}{P(\lambda_R, r_0)}\right)^2} \end{aligned} \quad (2.45)$$

Therewith the systematical and statistical error of  $S_p$  can be written as

$$\begin{aligned} \Delta S_p^{syst}(\lambda_0, r) = & \left| \frac{\partial S_p(\lambda_0, r)}{\partial \alpha_p(\lambda_0, r)} \Delta \alpha_p^{syst}(\lambda_0, r) \right| + \left| \frac{\partial S_p(\lambda_0, r)}{\partial \beta_p(\lambda_0, r)} \Delta \beta_p^{syst}(\lambda_0, r) \right| \\ = & \left| S_p(\lambda_0, r) \frac{\Delta \alpha_p^{syst}(\lambda_0, r)}{\alpha_p(\lambda_0, r)} \right| + \left| S_p(\lambda_0, r) \frac{\Delta \beta_p^{syst}(\lambda_0, r)}{\beta_p(\lambda_0, r)} \right| \end{aligned} \quad (2.46)$$

and

$$\begin{aligned} \Delta S_p^{stat} = & \sqrt{\left(\frac{\partial S_p(\lambda_0, r)}{\partial \alpha_p(\lambda_0, r)} \Delta \alpha_p^{stat}(\lambda_0, r)\right)^2 + \left(\frac{\partial S_p(\lambda_0, r)}{\partial \beta_p(\lambda_0, r)} \Delta \beta_p^{stat}(\lambda_0, r)\right)^2} \\ = & \sqrt{\left(S_p(\lambda_0, r) \frac{\Delta \alpha_p^{stat}(\lambda_0, r)}{\alpha_p(\lambda_0, r)}\right)^2 + \left(S_p(\lambda_0, r) \frac{\Delta \beta_p^{stat}(\lambda_0, r)}{\beta_p(\lambda_0, r)}\right)^2} \end{aligned} \quad (2.47)$$

Error of lidar signals

For the photon-counting signals, the signal noise is estimated by applying the law of error propagation and Poisson statistics. The signal noise for the analog signals is estimated as follows.  $a$  is used as subscript for the noise of the amplifier and the skylight background,  $ps$  for photon statistics. The virtual number of photons in the analog signal is denoted as  $N$ .  $r_0$  is set as the reference (middle of reference range; i.e. the Rayleigh fit range). The noise  $\sigma$  of the analog amplification and from photon statistics is uncorrelated. Thus it can be written

$$\sigma = \sqrt{\sigma_a^2 + \sigma_{ps}^2} \quad (2.48)$$

The noise  $\sigma(r)$  at an arbitrary range-bin  $r$  can be calculated from the standard deviation of a number of range-bins around  $r$  provided that the signal variations are only due to photon statistics and not due to changes in the aerosol distribution. As a consequence, the Rayleigh fit range around  $r_0$  is best suited to determine  $\sigma$  as the standard deviation of the signal noise. Any other signal range would lead to a less accurate (overestimated)  $\sigma$  as temporal and spatial changes of the aerosol distribution would contribute to the standard deviation.

The range independent  $\sigma_a$  is determined from the pretrigger range that extends typically over a range of 300 range bins prior to the laser shot. Hence  $\sigma_{ps}$  is determined for range  $r_0$  from Equation 2.48.

$$\sigma_{ps}(r) = \sqrt{\sigma(r)^2 - \sigma_a^2} \quad (2.49)$$

and derive  $\sigma_{ps}(r)$  for any other range  $r$  according to

$$\sigma_{ps}(r) = \sqrt{N(r)} = \sqrt{\frac{N(r)}{N(r_0)}} \cdot \sigma_{ps}(r_0) = \sqrt{\frac{P(r)}{P(r_0)}} \cdot \sigma_{ps}(r_0) = \sqrt{\frac{P(r)}{P(r_0)}} \cdot \sqrt{\sigma(r_0)^2 - \sigma_a^2} \quad (2.50)$$

where  $P(r)$  is the measured lidar signal. Finally, it is

$$\sigma(r) = \sqrt{\sigma_a^2 + \frac{P(r)}{P(r_0)}(\sigma(r_0)^2 - \sigma_a^2)} \quad (2.51)$$

This is used for  $\Delta X$  and  $\Delta P$ , which are required for the assessment of the errors described above.

### 2.5.2 Error of the particle linear depolarization ratio

The error calculation for the particle linear depolarization ratio  $\delta_p$  is done according to Freudenthaler et al. (2009), considering an additional error evoked from the uncertainty in the measurements of the molecular linear depolarization ratio  $\delta_m$  and the detection limits of the lidar systems. The error calculation considers only the systematical errors caused by uncertainties of the input parameters. Statistical noise errors from photon statistics and amplification noise are not considered here as they are small compared to the systematical errors.

Equation 2.32 can be rewritten as

$$\delta_p = \frac{\delta_v (1 + \delta_m) B + (\delta_v - \delta_m)}{(1 + \delta_m) B - (\delta_v - \delta_m)} \quad (2.52)$$

with

$$B = R - 1 = \frac{\beta_p}{\beta_m} \quad (2.53)$$

With the assumption  $\delta_m \ll 1$  it follows

$$\delta_p = \frac{\delta_v B + (\delta_v - \delta_m)}{B - (\delta_v - \delta_m)} \quad (2.54)$$

The systematical error caused by uncertainties in the system and input parameters can be derived from

$$\Delta\delta_p = \left| \frac{\partial\delta_p}{\partial B} \Delta B \right| + \left| \frac{\partial\delta_p}{\partial\delta_v} \Delta\delta_v \right| + \left| \frac{\partial\delta_p}{\partial\delta_m} \Delta\delta_m \right| \quad (2.55)$$

with

$$\Delta B = \left| \frac{\partial B}{\partial\beta_p} \Delta\beta_p \right| + \left| \frac{\partial B}{\partial\beta_m} \Delta\beta_m \right| \quad (2.56)$$

the second part of Equation 2.56 is neglected.

$$\Delta B = B \frac{\Delta \beta_p}{\beta_p} \quad (2.57)$$

$\beta_p$  is derived from the Fernald inversion (Section 2.3.1) with uncertainties in the reference value  $\beta_p(r_0)$  and the lidar ratio  $S_p$ . The error of  $\beta_p$  was determined from the maximum difference that can be achieved from the minimum and maximum values of  $\beta_p(r_0)$  and range dependent lidar ratio  $S_p(r)$ . The error of  $\beta_p(r_0)$  is estimated from the volume depolarization ratio in the reference height, similar to the method of Tesche et al. (2009b) considering the signal noise around  $r_0$ .  $S_p(r)$  and the corresponding error of  $S_p(r)$  is adopted from simultaneous or the closest Raman measurements in time.

For the volume linear depolarization ratio  $\delta_v$  it is considered:

$$\frac{\Delta \delta_v}{\delta_v} \approx \left| \frac{\delta V}{V} \right| + \left| \frac{\delta R_s}{\delta_v} \right| \quad (2.58)$$

As additional polarizing filters are used behind the beam splitter cube, the cross-talk is suppressed and the error of  $\delta_v$  is reduced to  $\left| \frac{\delta V}{V} \right|$ . The calibration constant  $V$ , determined at least one time a day for the same lidar setup, shows a relative difference lower than 0.01.

Due to the system setup a limitation of the detection of the molecular linear depolarization ratio and a resulting error of 0.0022 is considered.

The partial derivatives of Equation 2.55 can be written as

$$\frac{\partial \delta_p}{\partial B} = \frac{\delta_v - \delta_p}{B - (\delta_v - \delta_m)} \quad (2.59)$$

$$\frac{\partial \delta_p}{\partial \delta_v} = \frac{(B + 1) + \delta_p}{B - (\delta_v - \delta_m)} \quad (2.60)$$

$$\frac{\partial \delta_p}{\partial \delta_m} = \frac{\delta_p - 1}{B - (\delta_v - \delta_m)} \quad (2.61)$$

# Chapter 3

## Instrumentation

### 3.1 Lidar systems

For the measurements of the linear depolarization ratio  $\delta$  and the lidar ratio  $S_p$  three ground-based depolarization- and Raman-lidar-systems were operated during the two campaigns of the Saharan mineral dust experiment (SAMUM), as well as one high spectral resolution lidar (HSRL) on board of the research aircraft falcon. The measurements of transported aerosols to Central Europe were performed with tow lidar systems over Munich and/or Maisach. In the following, the lidar systems are briefly described.

#### 3.1.1 POLIS

The portable lidar system POLIS was developed at the Meteorological Institut (MIM) of the Ludwig-Maximilians-Universität, München. It can be operated from ground or from an aircraft. To measure either the linear depolarization ratio or the Raman-backscatter it was constructed modular with two detection options (see Figure 3.1).

Table 3.1: POLIS - Technical Data

Laser	Nd:YAG ('Big Sky, Ultra GMR')
Wavelength	355 nm
Pulse-Energy	7-8 mJ
Repetition-Rate	20 Hz
Beam-Divergence	0.69 mrad
Telescope	Dall-Kirkham, 175 mm
Focal length	1.2
Field of View	typ. $\pm 2.5$ mrad
Range Resolution	7.5 m
Range	ca. 100 m to free troposphere
Weight	3 parts, 15 kg each
Size	0.6 m <sup>3</sup>

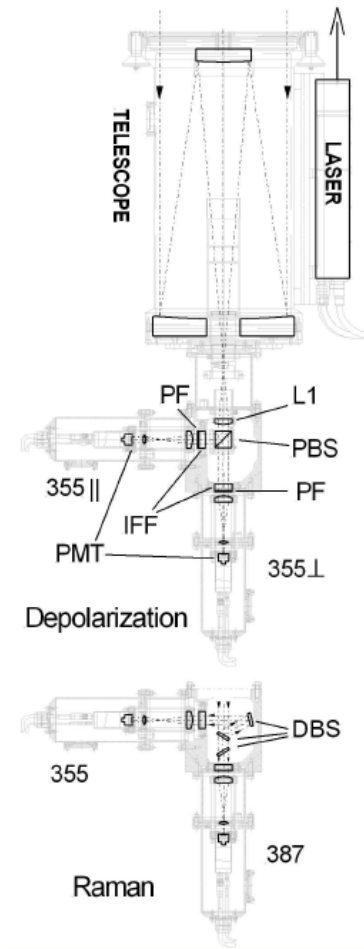


Figure 3.1: POLIS - Schematic with depolarization and Raman module. L1 - collimating lens, PBS - polarizing beam splitter cube, IFF - interference filter, PMT - photomultiplier, PF - polarizing filter, DBS - dichroic beamsplitter cube.

The telescope of POLIS is a Dall-Kirkham Cassegrain with an effective diameter of 175 mm. The laser is a frequency doubled and tripled flashlamp-pumped Nd:YAG laser (Big Sky, Ultra GMR). In the used configuration it emits only linear polarized light at 355 nm with a repetition rate of 20 Hz and a pulse energy of 7.5 mJ. The laser is assembled to the telescope using a high precision and stable two-axis tilting mount, with which the laser can be adjusted with respect to the telescope axis with an accuracy better than 0.1 mrad. The minimum overlap range of POLIS is at about 100 m. The main system parameters are summarized in Table 3.1.

As mentioned above, POLIS either measures the parallel and cross-polarized signals at 355 nm or the backscatter at 355 nm and the  $N_2$ -Raman shifted wavelength at 387 nm. The two detection modules are mounted to the telescope by a superfinished circular flange behind the collimating lens. No optical realignment is required. With this mounting a change of the two modules is easy and can be done within about ten minutes. It was used



regularly during the measurement situations described in this work.

The flange also allows the accurate rotation of the whole depolarization detector module with respect to the laser polarization for alignment and calibration purposes. The separation of the co- and the cross-polarized signals is achieved by a custom-made polarizing beam-splitter cube (Optarius, UK) with a transmission  $T_p$  of 95.21% and a reflection  $R_s$  of 99.85%. In order to minimize cross-talk effects, the parallel-polarized signal is detected in the reflected channel of the polarizing beam-splitter cube (see Section 2.4). Additional polarizing filters (LPG-23, ITOS, Germany) are used in the depolarization module in each channel behind the polarizing beam splitter cube to suppress the cross-talk. Thus the radiation in the corresponding channels is now completely co- or cross-polarized with respect to the laser-polarization. The calibration of the depolarization measurements is done by the  $\pm 45^\circ$ -method (see Section 2.4.2).

Using the measurements with the Raman module, the lidar ratio  $S_p$  at 355 nm can be retrieved with POLIS, and so a complete evaluation of the linear particle depolarization ratio at 355 nm is possible. The  $90^\circ$  reflection of the 355 nm by means of two consecutive, custom-made  $25^\circ$  dichroic beam-splitters (see Figure 3.1) and the additional, same dichroic beam-splitter for axis shift compensation increase the wavelength separation and thus reduce the crosstalk from the 355 nm to the 387 nm channel.

Each channel has an interference filter with 1nm bandwidth, and can be equipped with neutral density filters. A quick exchange of the neutral density filters makes it possible to optimize them for the individual detection channel, the signal range and the meteorological conditions. The data acquisition is a LICEL (Germany) TR-20 with Hamamatsu photomultipliers R7400 for combined analog and photon-counting signals.

### 3.1.2 MULIS

MULIS (Multi-wavelength Lidar System - Freudenthaler et al. 2009) is a mobile, five wavelength lidar system with a Nd:YAG laser (Coninum, Surlite II), frequency doubled and tripled by Potassium Dideuterium Phosphate crystals. It has backscatter channels at 355, 532 and 1064 nm and  $N_2$ -Raman-shifted channels at 387 and 607 nm. The relevant system specifications can be found in Table 3.2.

The receiving telescope, the laser, and the receiving optics are directly assembled on the scanning mount. The laser axis can be adjusted with respect to the axis of the receiver optical axis with an accuracy of 0.1 mrad. The minimum overlap range of the system is between about 200 - 400 m. An adjustable field stop is used to decrease the field of view and thus the signal power in the near range during special measurement situations and during calibration measurements.

The beamsplitters BS1 to BS4 are used at  $30^\circ$  to minimize diattenuation effects of the dichroic beam-splitters (see Figure 3.2). The custom made polarizing beam-splitter cube (PBS) (Optarius, UK) has high  $T_p = 0.9831$  and high  $R_s = 0.9991$ , however, due to the divergence of the incident beam on the PBS the effective  $R_s$  is estimated to be  $0.9965 \pm 0.002$ . In order to minimize cross-talk the co-polarized signal was detected in the reflected branch of the PBS. Additional polarizing sheet filters behind the PBS suppress

Table 3.2: MULIS - Technical Data

Laser	Nd:YAG ('Continuum, Surelite II')
Wavelength	355, 532, 1064 nm
Pulse-Energy	175 mJ + 50 mJ + 175 mJ
Repetition-Rate	10 Hz
Beam-Divergence	0.6 mrad
Telescope	Cassegrain, 300 mm
Focal length	0.96
Field of View	1 - 2.5 mrad
Range Resolution	7.5 m
Range	ca. 200-400 m to free Troposphere
Size	1.3 m <sup>3</sup>

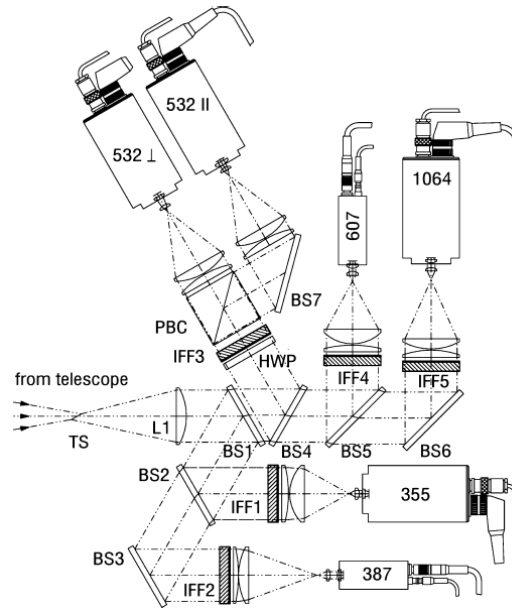


Figure 3.2: Optical setup of the MULIS receiver with analog backscatter channels at 355 nm, 532 nm (parallel- and cross- polarized), 1064 nm, and Raman channels at 387 and 607 nm. TS, tilted slit diaphragm; L1, collimating lens; BS\*, dichroic beamsplitters (BS3, 6 and 7 are used as mirrors); IFF\*, interference filter; PBC, polarizing beam-splitter cube at 532 nm and HWP, half-wave plate at 532 nm for the calibration of the depolarization channels. - Figure adopted from Freudenthaler et al. 2009

cross-talk, so that the powers in the respective channels are completely co- and cross-polarized. In front of the PBS (not shown in Fig. 3.2), a half-waveplate (Casix, China) is used to rotade the plane of polarization. It is mounted in a custom made rotation mount. The stepping motor drive is computer controlled with an accuracy and repeatability of rotation better than  $0.1^\circ$  For the 1064 nm signal an avalanche photo diode (APD) is used,

for all other channels Hamamatsu R7400 photomultiplier tubes (PMT). Analog detection with an A/D-conversion of 12 or 14 bits are used for the elastic backscatter channels at 355 and 532 nm. It is accomplished by transient recorders on PC-boards (Spectrum GmbH, Germany). LICEL detector modules (LICEL, Germany) in the combined analog and photon-counting mode were used for the Raman channels. The signal strength was adjusted (individually per channel) with fixed absorbing neutral density filters (Schott, Germany).

### 3.1.3 Bertha

Bertha (backscatter extinction lidar-ratio temperature humidity profiling apparatus) is a six-wavelength lidar designed and employed by the Leibniz Institute of Tropospheric Research (IFT), Leipzig, Germany. For the transmittance of the six wavelength four lasers are employed. One Nd:YAG laser transmits pulses at 355, 532 and 1064 nm, another is used for pumping two Ti:Sa (Titanium-sapphire) lasers, one of them emitting linear polarized light at 710 nm, the other emits pulses at 400 and 800 nm. All six beams are aligned onto one optical axis. The telescope is a Cassegrain with a diameter of 530 mm.

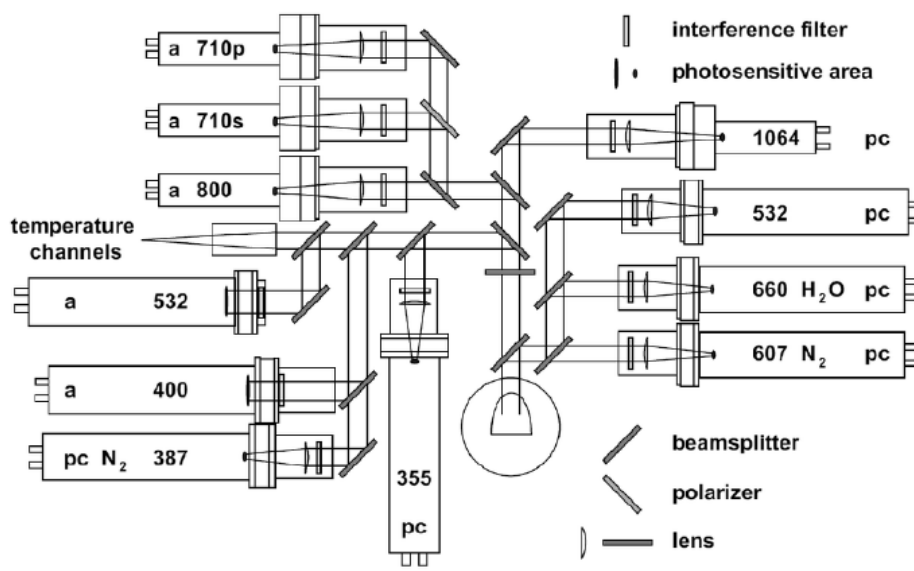


Figure 3.3: Sketch of the BERTHA receiver. The 14-channel lidar measures elastic backscatter signals (355, 400, 532, 710, 800, 1064 nm), vibrational Raman signals (387, 607, 660 nm, nitrogen N<sub>2</sub>, water vapor H<sub>2</sub>O), and rotational Raman signals around 532 nm (temperature channels, includes another 532 nm elastic backscatter channel). The number denotes the detection wavelength of the respective photomultiplier tube, abbreviations a and pc describe the kind of signal detection (analog or photon counting), s and p (710 nm) denote channels for detection of cross and parallel-polarized light, respectively. - Figure adopted from Tesche et al., 2009a

Bertha has channels for the elastically backscattered light at the six emitted wavelengths and for the Raman shifted wavelengths at 387, 607 nm (nitrogen) and 607 nm (water vapor). Furthermore it has pure rotational Raman channels from oxygen and nitrogen around 532 nm for measurements of the temperature profile. The setup of the multichannel receiver is shown in Figure 3.3. For the co- and cross-polarized components of the backscattered light, Photomultiplier tubes (PMT) are used as detectors. For the elastically backscattered signals at 400, 532, 710 and 800 nm the analog detection is used with an A/D conversion of 12 bit, whereas for the 355 and 1064 nm, as well as for the Raman signals photoncounting detection PMTs operating at 300 MHz are used. For calibration of the depolarization measurements, the  $0^\circ$ -method was applied during SAMUM-1. During SAMUM-2 the  $\pm 45^\circ$ -method was applied (see Section 2.4.2). The system is described in details in Tesche et al. (2009a). For this work only the measurements of the particle linear depolarization ratio at 710 nm is of interest.

### 3.1.4 HSRL

As data of the High Spectral Resolution Lidar (HSRL) are considered in the analysis of SAMUM-1, the system is briefly described. The principle of HSRL is based on two measured profile which can be processed to yield separate returns of the molecular and aerosol scattering. The method uses the Doppler shift produced when photons are scattered by molecules due to their thermal motion. In contrast, the moving of aerosol particles is low and the spectral broadening is negligible. The HSRL, applied during SAMUM, was operated from the Deutsches Zentrum für Luft und Raumfahrt (DLR), Oberpfaffenhofen, Germany. It is based on a high-powered Nd:YAG laser at 100 Hz. The laser is diode-pumped and injection-seeded. The HSRL measures the extinction at 532 nm and the linear particle depolarization ratio at 532 and 1064 nm. For the spectral separation dichroic beam-splitters (DBS) are used in the receiver module, and for the separation of the co- and cross-polarized returns polarizing beam-splitters (PBS). Additional PBS behind the first one suppress the cross-talk. The depolarization calibration is done with the  $45^\circ$ -method by manually rotating the detection optics. The schematic of the receiver module is shown in Fig. 3.4 A detailed description of the system can be found in Esselborn et al., (2008).

## 3.2 Sun-photometer and radiosondes

In this work, data of two sun-photometers are used: The sun- and sky-radiometer SSARA (Sun- and Sky Automated RAdiometer), developed and operated by MIM (Toledano et al., 2009), was operated during both SAMUM campaigns. It provides measurements of aerosol optical depth (AOD) at several wavelengths in the range 340 - 1550 nm, available in one minute steps. Measurements of a Cimel sun- and sky-photometer from the MIM-AERONET site were used for the aerosol characteristics over the lidar measurement site Munich. It measures direct spectral radiances at twelve wavelengths between 340 - 1020 nm. During the SAMUM campaigns at Quarzazate (Morocco) and Praia (Cape Verde),

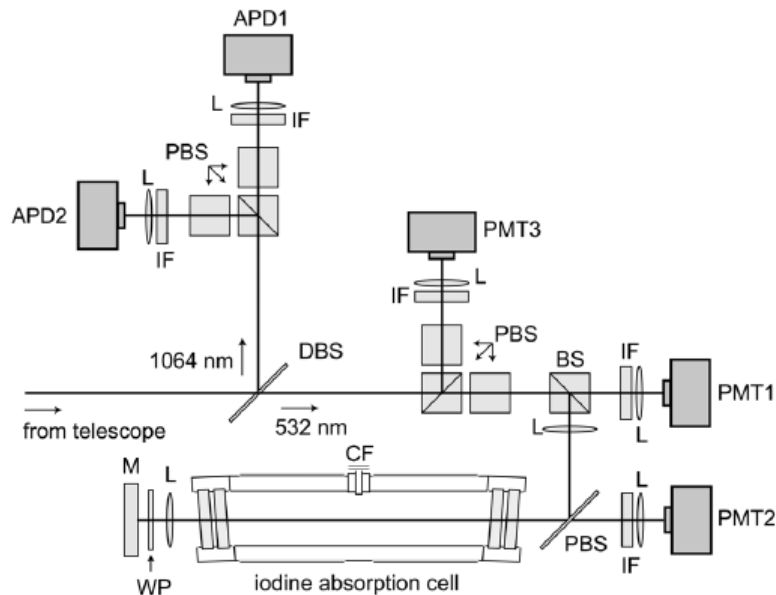


Figure 3.4: Schematic of the receiver module used for detection at 532 nm and 1064 nm. APD: avalanche photo diode, BS: beam splitter, CF: cool finger, DBS: dichroic beam splitter, IF: interference filter, L: lens, M: mirror, PBS: polarization beam splitter, PMT: photomultiplier, WP: quarter wave plate - Figure adopted from Esselborn et al., 2009

radiosondes were launched from IFT during the measurement sessions, typically twice a day. They provide relative humidity-, temperature- and pressure-profiles, required for the Rayleigh-calibration of the lidar signals. For the analysis of the lidar measurements over Munich and Maisach, radiosonde data from regular launches, twice a day, at Oberschleißheim from the German Weather Service (DWD), are used. Measurements of the Cimel sun- and sky-photometers employed during SAMUM are not considered in this work.

### 3.3 Improvements of POLIS

After the first measurement campaign of SAMUM, POLIS was improved with respect to measurement range and accuracy of depolarization measurements, which will be described in the following.

#### 3.3.1 Gluing algorithm

During SAMUM-1 only the analog detection of the Hamamatsu-PMT was used, with signal maximum at the limit of the preamplifier range. These analog systems are infected by preamplifier distortion in the far-range and additionally suffer from oscillations, when detecting signals outside the linearity range of the preamplifier. (In our case the optimal

maximal signal strength is about half of the preamplifier range  $\pm 10\%$ .) These effects limit the measurement range of the systems. It can be improved by combination of simultaneously measured analog and photon-counting signals ('gluing'). For the strong signals (in the near range) the analog detection is used and for the weak signals in the far range the high sensitivity of the photon counting detection. For combining both signals, they must be both undistorted in an overlap-range of sufficient length. According to LICEL (Bernd Mielke, personal communication) that region extends to 0.5 counts per range-bin (7.5m range-bin) in the photon-counting for the used photomultiplier. For the analog signals an empirical threshold of 0.1 mV for the lower limit was found. Above that threshold the signal is assumed to be not influenced from signal distortion with a high signal to noise ratio. This range can be controlled by the optical transmission of the receiver by means of neutral density filters and by amplification of the preamplifier. With these optimal settings, analog and photon-counting signals perfectly match in a range of about 1 to 3 km and can be readily combined, considering the lower and higher threshold (in our case 1.1 - 1.4 km). The photon counting signals have to be dead-time corrected for the gluing. For this purpose a so called non-paralyzable behavior of the system is assumed.

$$N = \frac{S}{1 + S * \tau_d} \quad (3.1)$$

where N is the observed count-rate, S is the true count-rate and  $\tau_d$  is the system dead time. Equation 3.1 can be inverted to

$$S = \frac{N}{1 - N * \tau_d} \quad (3.2)$$

however this method can only be used for low count-rates. The background is subtracted separately from the analog and photon-counting signals. Between the lower threshold and the higher threshold ('gluing range') a linear regression is performed to convert the analog signal into a virtual photon counting signal.

$$\sum_{i=1}^n (PC(z_i) - a * Ana(z_i))^2 = \min \quad (3.3)$$

Figure 3.5 shows an example of the glued analog and photon counting signals of the co-polarized signal. The black line shows the photon-counting signal, the gray line the analog signal after being normalized with respect to the photon-counting signal between 1.1 km and 1.4 km. The analog and photon-counting signals match well up to about 3 km. The thin black line shows the attenuated molecular backscatter from actual radiosonde

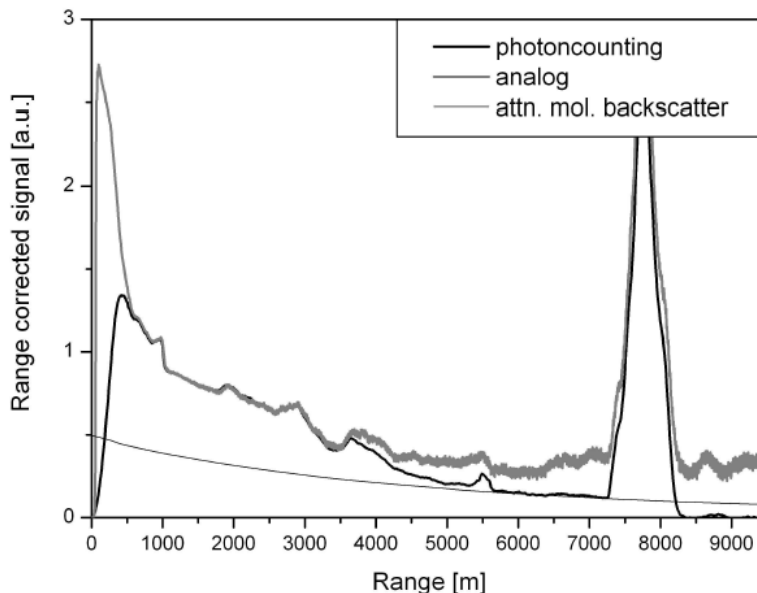


Figure 3.5: Glued analog and photon counting range-corrected signals of the co-polarized channel fitted between 1.1 and 1.4 km. Thin line: attenuated molecular backscatter from actual radiosonde data.

data. As can be seen, with a combination of analog and photon-counting signals the dynamic range, and with this the height range of the signal can be significantly improved. The use of the photon-counting signal in the far range allows a calibration of the signals without further information. On the other end of the detection range, the analog signal allows the measurement of the high near range signal, which otherwise would be lost by saturation of the photon-counting signal. The measurements took place on 03 February 2008 during the field experiment of SAMUM 2 in Praia, Cape Verde. With glued analog and photon-counting signals a signal analysis regarding extinction coefficient and particle linear depolarization ratio is possible from about 100 m above ground to the free troposphere.

### 3.3.2 Depolarization calibration

Note, that in depolarization mode the co- and cross-polarized signals are measured separately. Thus, to evaluate the total backscatter signal and the linear volume depolarization ratio from the measured signals, the relative calibration factor  $V = V_R/V_T$  (see Section 2.4) is needed. For POLIS  $V$  is achieved with the  $\pm 45^\circ$  depolarization-calibration method with two measurements at  $+45^\circ$  and  $-45^\circ$  rotation of the detection module. As additional polarization filters are used since SAMUM-2 to reduce the cross-talk, we can set  $R_s=T_p=1$  and get

$$V = \sqrt{P_R/P_T(-45^\circ)P_R/P_T(+45^\circ)} \quad (3.4)$$

with the measured signals  $P_R$  and  $P_T$  in the reflected and transmitted channel, respectively. The error of this calibration depends on the accuracy of the  $90^\circ$  difference of the two measurements. It appears that this was the main source of the large errors in the depolarization ratio during SAMUM-1. To reduce the error, mechanical limit stops were placed at the mounting flange before SAMUM-2, ensuring less than  $0.1^\circ$  deviation from the  $90^\circ$  difference, resulting in a relative error of  $\delta_v$  of less than 1%.

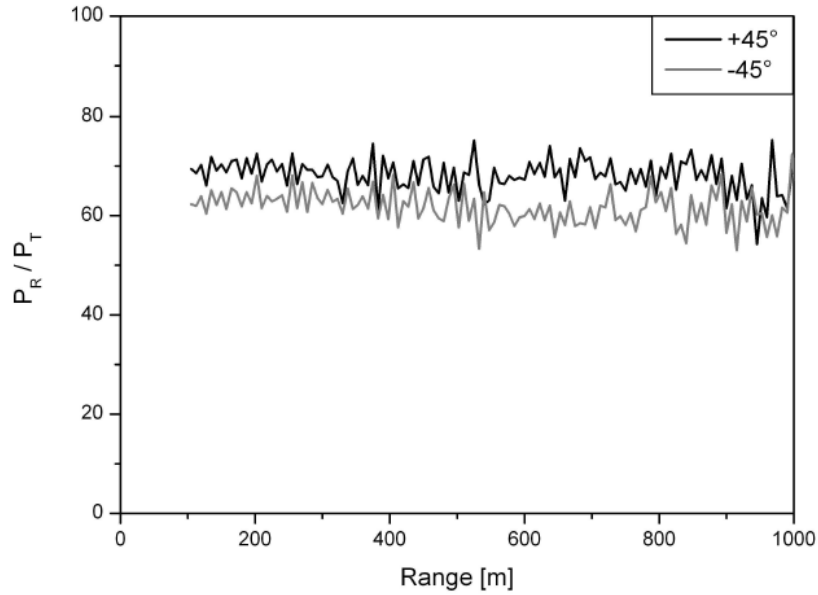


Figure 3.6: Range dependent analog signal ratios  $P_R/P_T(+45^\circ)$  and  $P_R/P_T(-45^\circ)$

Another problem was the saturated signal in the cross-polarized channel during the calibration-measurements. Using perforated plates on top of the telescope as neutral density filters for all channels, the signal strength can be reduced without changing any parameter, which could influence the calibration factor.

Altogether a significant improved depolarization calibration and measurement is achieved. In Figure 3.6 the range dependent signal ratios  $P_R/P_T$  of the  $+45^\circ$  and  $-45^\circ$  measurements of the analog and photon-counting signals are plotted. The constancy of the ratios (apart from noise) shows, that there is no differential range dependency of the signal ratios of the transmitted and reflected channels. The constant offset of the signal ratios of the  $+45^\circ$  and  $-45^\circ$  measurements indicates the error of the single  $45^\circ$ -calibration, resulting from misalignment of the PBS with respect to the plane of laser polarization under an angle  $\varphi$ . At a single calibration measurement at  $+45^\circ$  or  $-45^\circ$  this misalignment would lead to an error of  $V$  and thus of the total backscattered signal. With two subsequent measurements at exactly  $90^\circ$  difference ( $\pm 45^\circ$ -calibration method) the errors compensate each other very well.



# Chapter 4

## Characterization of selected aerosol types

In the following the results of the measurements during the SAMUM-project and during special meteorological events over Central Europe are presented. The optical properties of the major aerosol components of the Earth's atmosphere, mineral dust, biomass burning aerosols, and sea salt, as well as of volcanic particles are characterized by lidar measurements. For a classification, the intensive parameters lidar ratio  $S_p$  and particle linear depolarization ratio  $\delta_p$ , both at 355 nm and 532 nm are used.

### 4.1 Saharan dust

#### 4.1.1 Fresh pure Saharan dust

For the characterization of the optical properties of fresh, pure Saharan dust, the findings during SAMUM-1 (Tesche et al., 2009a; Freudenthaler et al., 2009) are used. These findings are important as they are used to analyze the changes of Saharan dust during transport and lifetime.

Two major dust episodes occurred during the first SAMUM campaign, characterized by an Angström exponent (440-870nm) of  $\kappa \leq 0.3$  (Figure 4.1). The aerosol optical depth (AOD) at 500 nm during the two dust events ranged between 0.3 and 0.6, and reached maximum values near 0.9. The first episode lasted from 12 - 22 May 2006, when a low-level cyclone advected dust loaded air-masses to the measurement site in Morocco. During the second period, starting on 2 June 2006, a surface high brought dusty air to Morocco.

Measurements of the Raman-lidar system Bertha, during the whole measurement campaign, result in statistical mean  $S_p$  of  $55 \pm 5$  sr at 355 nm, and  $56 \pm 5$  sr at 532 nm for pure, fresh Saharan dust (Tesche et al., 2009a). The mean values of  $\delta_p$  were  $\delta_p = 0.26 \pm 0.06$  at 355 nm,  $\delta_p = 0.31 \pm 0.01$  at 532 nm (MULIS),  $\delta_p = 0.27 \pm 0.09$  at 710 nm (Bertha), and  $\delta_p = 0.26 \pm 0.04$  at 1064 nm (HSRL). Although the errors of 355 nm and 710 nm are very large, the minimum and maximum  $\delta_p$  values are between 0.17 and 0.39 for the whole

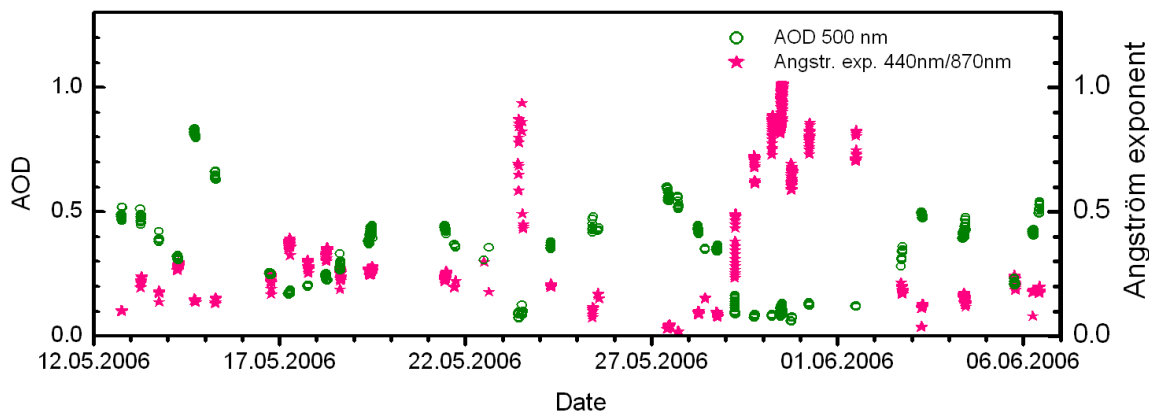


Figure 4.1: Aerosol optical depth at 500 nm and Angström exponent (440 nm / 870 nm) from SSARA sun-photometer measurements over Quarzazate.

wavelength range between 355 and 1064 nm (Freudenthaler et al., 2009). As an example of the vertical structure, the analyses of 19 May 2006 are shown in the following, as presented by Freudenthaler et al. (2009) and Tesche et al. (2009a).

### Case study 19 May 2006

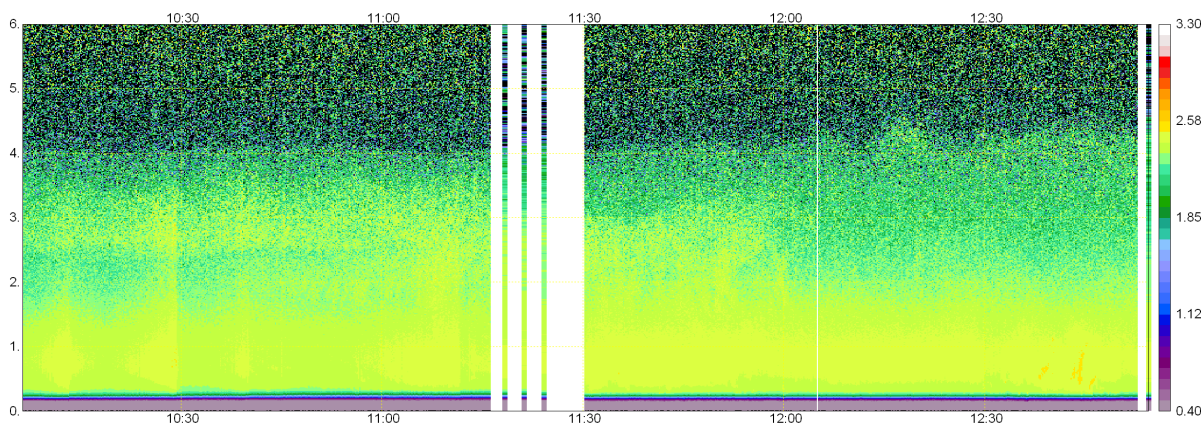


Figure 4.2: Time-height cross section of the range-corrected signal at 532 nm derived from MULIS lidar measurements at Ouarzazate on 19 Mai 2006, 10:00 - 12:55 UTC, for 0 - 6 km above sea level.

Figure 4.2 displays the measurements during the morning session (10:00 - 13:00 UTC) on 19 May 2009 over Ouarzazate performed with the MULIS system. Shown is the range corrected signal at 532 nm. At the beginning of the measurements, the top of the stable

dust layer was at about 5 km (above sea level). After 11 UTC convection started, reaching the top of the layer (now about 5.5 km asl) at about 12:20 UTC.

Calculated HYSPLIT back-trajectories (Figure 4.3) indicate, that the dust was advected directly from Algeria. The dust loaded air masses passed the desert areas during the last three days before their arrival at Ouarzazate.

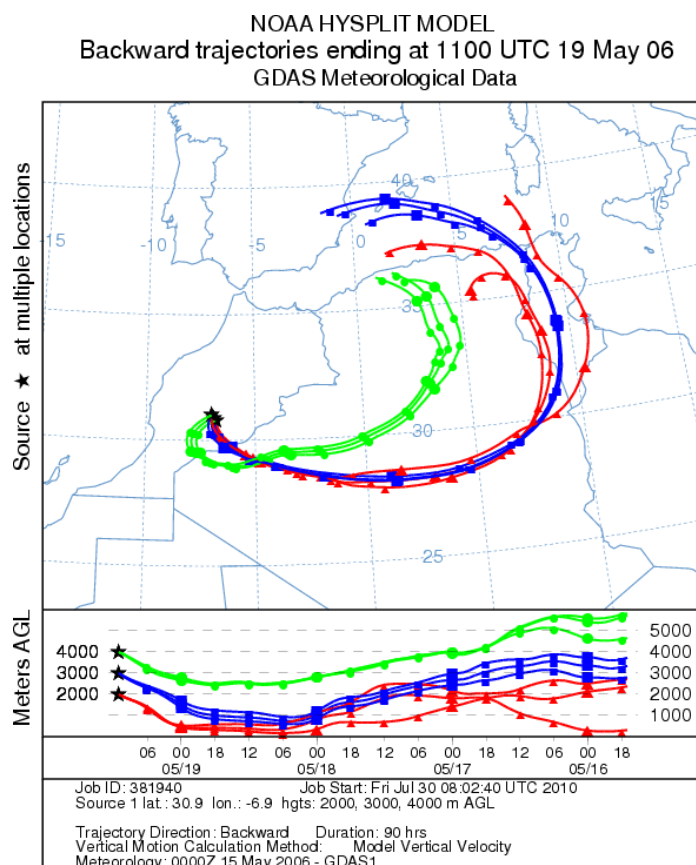


Figure 4.3: 90-h HYSPLIT backward trajectories ending in Ouarzazate, Morocco, on 19 May, 2006 at 11:00 UTC.

Figure 4.4 shows a set of optical properties at multiple wavelengths, derived with the three ground-based lidar systems and the HSRL on board of the Falcon aircraft. For the data analyses the lidar signals were averaged over different time periods (Bertha 09:59 - 11:16 UTC, POLIS 10:00 - 11:16 UTC, MULIS 10:16 - 10:51 UTC and HSRL 11:08 - 11:09 UTC). The profiles of the backscatter and extinction coefficient (panels a and b) show rather wavelength independent values. Measurements of the different instruments agree well. The most relevant parameter for this work is the lidar ratio  $S_p$ . As a consequence of the day-time measurements and the resulting high solar background, it could only be retrieved with the HSRL and with the very powerful Bertha at 532 nm. Due to technical reasons it is just available above 3.75 km asl for the latter.  $S_p$  shows a constant value of about 50 sr throughout the dust layer up to about 5.5 km.

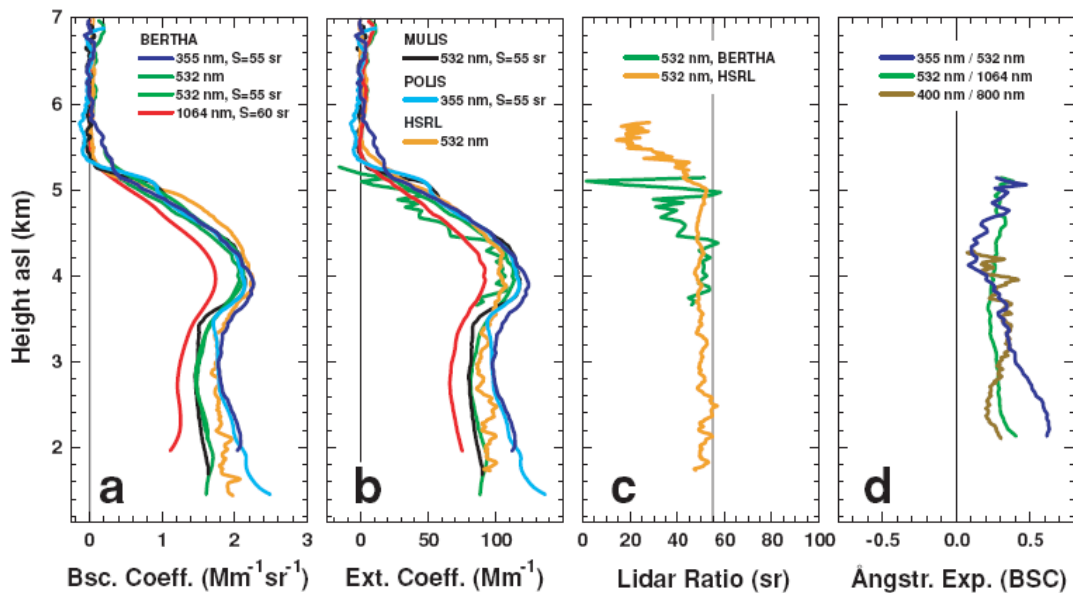


Figure 4.4: Backscatter coefficients (a), extinction coefficients (b), lidar ratio (532 nm) (c), and the backscatter-related Ångström exponent (d) for the wavelength pairs 355 nm/532 nm, 400 nm/800 nm, and 532 nm/1064 nm are shown. Signal smoothing lengths range from 300–660 m. - Plot from Tesche et al., 2009a

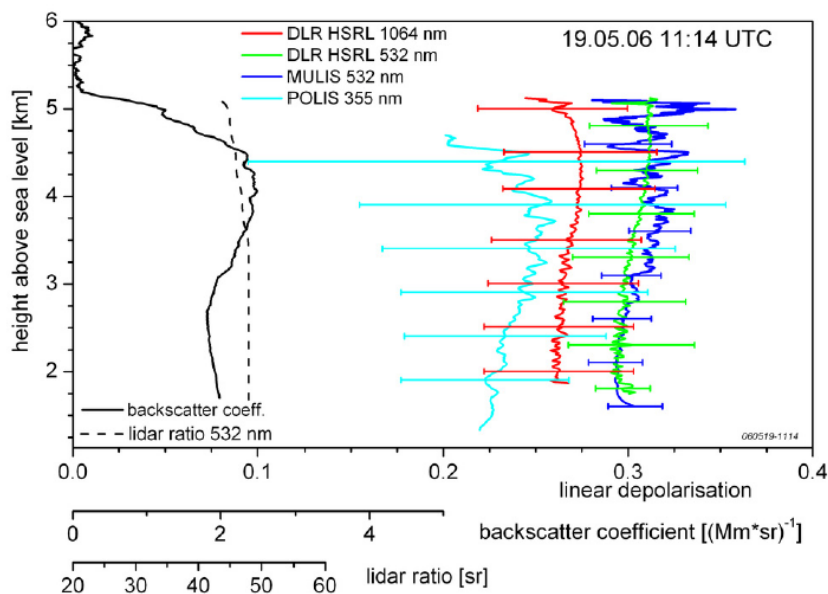


Figure 4.5: Particle linear depolarization ratio on 19 May, 11 UTC at several wavelengths over Ouarzazate. The error bars indicate the systematic uncertainties. The MULIS backscatter coefficient was calculated with the Fernald algorithms using the lidar ratio measured with the DLR HSRL. - Plot from Freudenthaler et al., 2009

In Figure 4.5 the profile of  $\delta_p$  with almost height-constant values, indicate a well mixed layer up to about 5.5 km. The mean values of  $\delta_p$  were found to be  $\delta_p = 0.24 \pm 0.07$  at 355 nm (POLIS),  $\delta_p = 0.31 \pm 0.01$  (MULIS), and  $\delta_p = 0.29 \pm 0.03$  (HSRL) at 532 nm, and  $\delta_p = 0.26 \pm 0.04$  at 1064 nm (HSRL). As can be seen, the most accurate values were achieved from the measurement of the MULIS system at 532 nm, and the HSRL at 532 nm and 1064 nm, showing a decrease with wavelength. At 355 nm the systematic errors are too large, to get significant information about wavelength dependence.

### 4.1.2 Aged pure Saharan dust

During the second field campaign of the SAMUM project, possible changes of Saharan dust during the first days of transport should be determined. The only episode of pure dust began on 28 January, 2008, when a major dust plume reached the Cape Verde Islands. The arrival of the dust at the measuring site occurred in the afternoon of January 28. This is supported by measurements of SSARA (Figure 4.6) showing an increase of the aerosol optical depth (AOD) at 500 nm after noon of 28 January up to values of 0.4 – 0.6. Simultaneously, the Angström exponent  $\kappa$  between 440 and 870 nm dropped below 0.2.

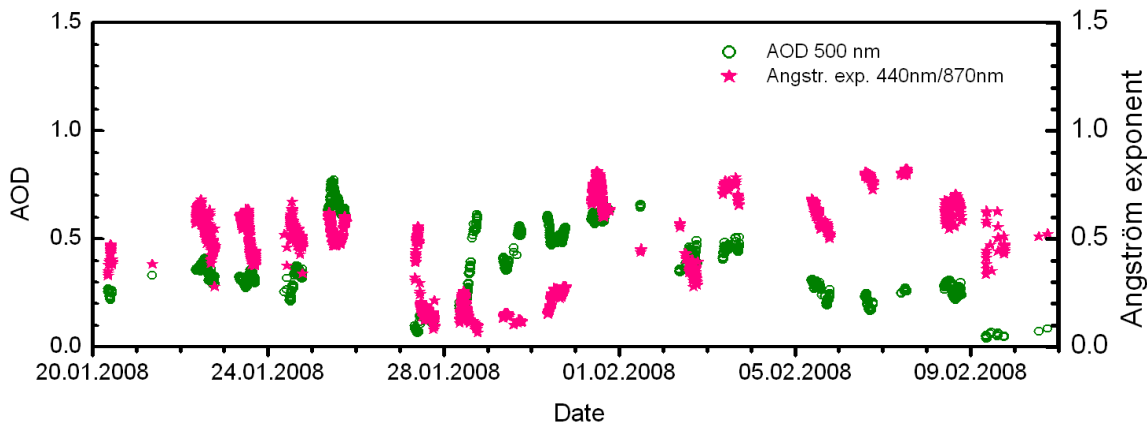


Figure 4.6: Aerosol optical depth at 500 nm and Angström exponent (440 nm / 870 nm) from SSARA sun-photometer measurements over Praia.

The strong easterly flow, advecting these dust loaded air-masses to Praia, was caused by a high pressure system over the Azores in the western Atlantic. Above 3.0 km clean air from northwest was advected due to a low pressure system located west of the Canary Islands.

Additionally to this event, almost during the whole measurement period dust was found between about 0.5 - 1.5 km, embedded between a mixture of dust and biomass burning aerosols in upper layers, and marine aerosols or a mixture of marine aerosols and dust in the boundary layer. The Raman lidar measurements result in  $48 \text{ sr} \leq S_p \leq 63 \text{ sr}$  at 355 nm and  $54 \text{ sr} \leq S_p \leq 66 \text{ sr}$  at 532 nm for pure, short-range transported Saharan dust with mean values of  $58 \pm 6 \text{ sr}$  and  $61 \pm 6 \text{ sr}$  at 355 nm and 532 nm, respectively. For  $\delta_p$  mean values

of  $0.25 \pm 2$  ( $0.25 - 0.27$ ) at 355 nm (POLIS),  $0.3 \pm 1$  ( $0.29 - 0.31$ ) at 532 nm (MULIS), and  $0.37 \pm 4$  ( $0.37 - 0.40$ ) at 710 nm (Bertha) are found. Due to the high accuracy of the measurements and the resulting small errors in  $\delta_p$  a clear increase of  $\delta_p$  with wavelength is evident for aged, pure Saharan dust. The errors allocated to the mean values denote the mean systematic errors.

As an example of the aerosol distribution, analyses of the particle linear depolarization ratio  $\delta_p$  and the lidar ratio  $S_p$  of 29 January are shown.

### Case study 29 January 2008

On 29 January the AOD from SSARA measurements showed a moderate mean value of 0.5 at 500 nm. The aerosol layers reached to about 1.0 km (above ground level), consisting of a boundary layer up to about 0.4 km and an overlying dust-layer. The structure and the stability of the layering (18:30 - 22:30 UTC) is shown in Figure 4.7 as measured with MULIS at 1064 nm (range-corrected signal). The columnar structure of the plot is a result of the measurements under different elevation angles ( $\Theta$ ) (scanning). Signals under different elevation angles differ in detected signal strength due to their different pathway through the atmosphere.

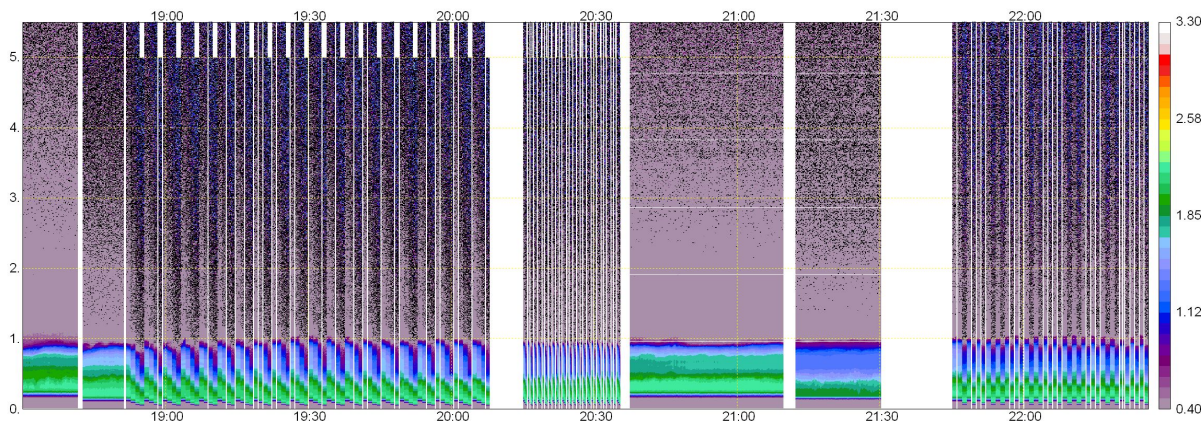


Figure 4.7: Time-height cross section of the range-corrected signal at 1064 nm derived from MULIS lidar measurements at Praia on 29 January 2008, 18:30 - 22:30 UTC, for 0 - 5.5 km above ground level.

HYSPLIT backward trajectories (Figure 4.8) identify the Saharan desert between ( $10^\circ$  N,  $15^\circ$  E) and ( $30^\circ$  N,  $15^\circ$  W) as source region and indicate that biomass burning did not influence the plume. The dust had traveled three to five days until it arrived at the Cape Verde Islands.

For the analysis of the Raman measurements (20:40 - 21:40 UTC) not only MULIS and POLIS measurements are combined. To get the best possible coverage of the lowermost atmosphere, also MULIS measurements at two elevation angles( $\Theta$ ) are combined. For the

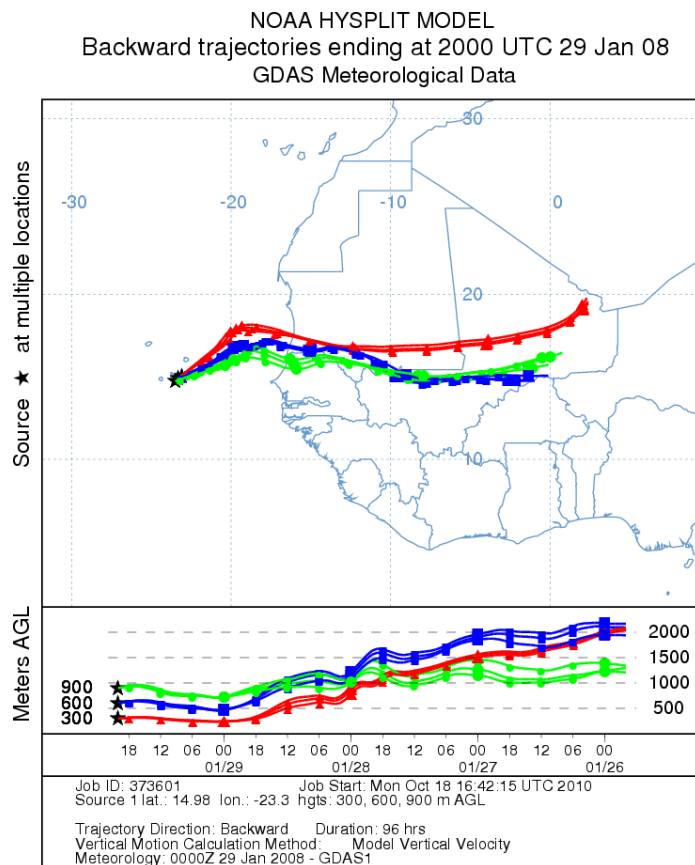


Figure 4.8: 96-h HYSPLIT backward trajectories ending in Praia, Cape Verde Islands, on 29 January, 2008 at 20:00 UTC

lowermost 0.5 km the measurements at  $\Theta=20^\circ$  is used, and  $\Theta=87^\circ$  above. The smoothing window length for MULIS is 53 range-bins, for POLIS ( $\Theta=79^\circ$ ) it is 21 range-bins up to 0.3 km and 53 range-bins else. For the analyses of  $\delta_p$  POLIS and MULIS measurements under an elevation angle of  $\Theta=79^\circ$  and  $\Theta=87^\circ$ , respectively, are used. For the analyses, the raw signals are smoothed with a window length of 11 range-bins. The elevation angle of Bertha was  $\Theta=90^\circ$  and the resolution of the raw data is 60 m. To analyze the linear depolarization ratio, a time period coincident with the Raman-measurements was chosen (20:40 - 21:40 UTC) for MULIS and Bertha. As already mentioned, POLIS could either measure in depolarization- or Raman mode, thus the selected time period for the depolarization analysis was just before the Raman measurements (18:00 - 20:00 UTC). As the temporal stability of the atmosphere was verified, the depolarization measurements of both time intervals are well comparable.

Figures 4.9 shows  $\alpha_p$ - and  $S_p$ -profiles, resulting from the Raman analysis at 355 nm (POLIS - cyan), and 355 nm and 532 nm (MULIS - blue and green). Figure 4.10 shows  $\delta_p$ -profiles at three wavelengths from the lidar systems POLIS (355 nm - cyan), MULIS (532 nm - green), and Bertha (710 nm - wine). The black line shows the mean backscatter

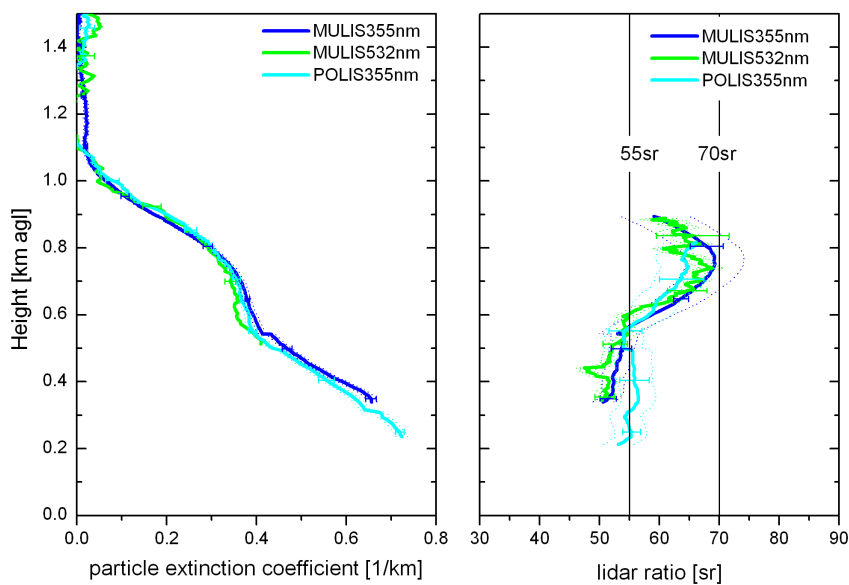


Figure 4.9: Raman measurements of the particle extinction coefficient and lidar ratio on 29 January 2008, 20:40 - 21:40 UTC at 355 and 532 nm above Praia. The error bars indicate the statistical errors, the dotted lines the systematic uncertainties.

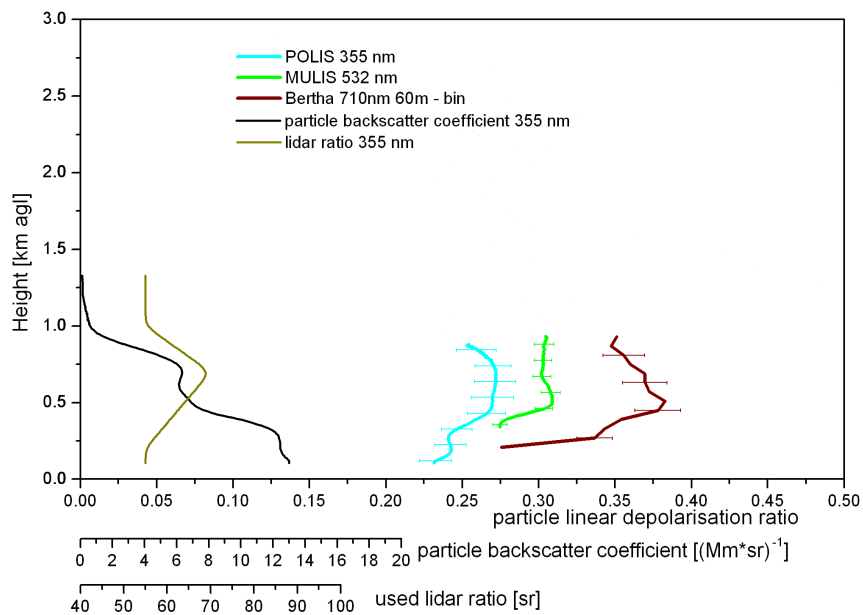


Figure 4.10: Particle linear depolarization ratio on 29 January, 20:40 - 21:40 UTC at 532 and 710 nm, and 18:00 - 20:00 UTC at 355 nm above Praia. The error bars indicate the systematic uncertainties.



coefficient at 355 nm to get an impression of the layering structure of the atmosphere, the golden line shows the used lidar ratio in the Klett-/Fernald algorithm (Section 2.3.1) for the analysis at 355 nm. The lidar ratios used for the analyses of  $\delta_p$  at 532 nm and 710 nm are not shown in this plot.

In the boundary layer  $\delta_p = 0.24 \pm 0.01$  at 355 nm and  $\delta_p = 0.28 \pm 0.01$  at 532 nm is derived. The mean lidar ratio values are  $S_p = 55 \text{ sr} \pm 3 \text{ sr}$  at 355 nm for POLIS and  $S_p = 53 \text{ sr} \pm 3 \text{ sr}$  at 355 nm and  $S_p = 52 \text{ sr} \pm 3 \text{ sr}$  at 532 nm for MULIS; note the good agreement between the POLIS and MULIS measurements. They are slightly lower than the values in the pure dust layer (0.5 - 1.0 km). Similar to the lower layer neither  $\alpha_p$  nor  $S_p$  show any wavelength dependence. The mean  $S_p$  in the pure dust layer are  $S_p = 60 \text{ sr} \pm 6 \text{ sr}$  (POLIS) and  $S_p = 65 \text{ sr} \pm 5 \text{ sr}$  (MULIS) at 355 nm, and  $S_p = 63 \text{ sr} \pm 2 \text{ sr}$  at 532 nm. Like in the boundary layer, the particle linear depolarization ratio  $\delta_p$  in the pure dust layer also shows clear wavelength dependence, however,  $\delta_p$ -values are a bit larger than in the boundary layer with means of  $\delta_p = 0.27 \pm 0.01$  at 355 nm,  $\delta_p = 0.30 \pm 0.01$  at 532 nm, and  $\delta_p = 0.36 \pm 0.04$  at 710 nm.

### 4.1.3 Long-range transported Saharan dust

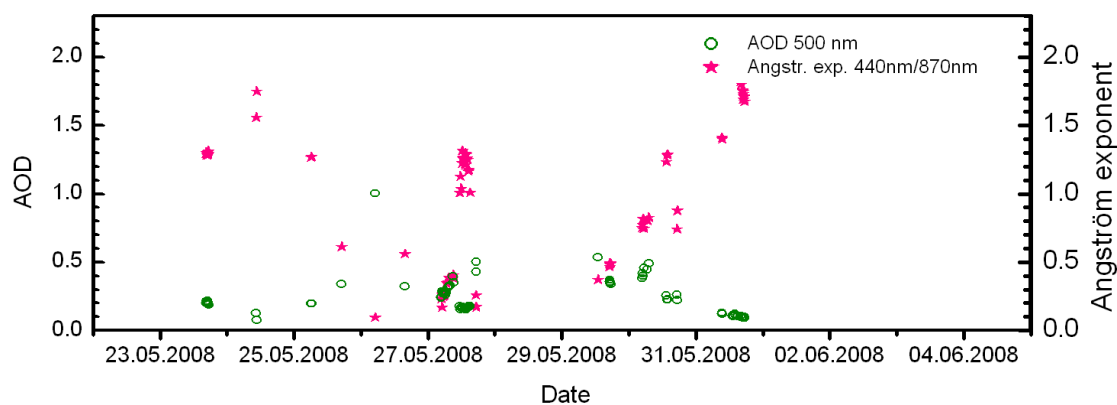


Figure 4.11: Aerosol optical depth at 500 nm and Angström coefficient (440 nm / 870 nm) from CIMEL sunphotometer measurements over Munich.

At the end of May 2008 one of the strongest Saharan dust outbreaks ever reached Central Europe. It significantly influenced the aerosol load over Southern Germany for as long as one week. High dust loaded air masses reached the measurement sites Munich and Maisach on 25 May 2008 with a southerly flow. A low pressure system over Western Europe together with a high pressure system over South-Eastern Europe in the first part of the event and North-Eastern Europe in the second part initiated the advection of warm dust loaded air masses from the Saharan desert to Central Europe. During the first part of the event they crossed north-western Libya, the Mediterranean Sea, northern Italy and the Alps before arriving in Central Europe. After the front passage on 30 May and 31

May, the high dust loaded air masses crossed north-westerly Algeria, the western part of the Mediterranean Sea, South France and Switzerland.

The dust episode is characterized by low Angström exponents (440/870 nm) of  $0.1 \leq \kappa \leq 0.5$ , and AOD of more than 0.3 at 500 nm, up to a maximum value of 1 (see Fig. 4.11). According to this, Munich was affected by the dust event from 25 May (noon) until 2 June 2008, interrupted by a front passage on 30 May. It led to relatively clean air for the next two days with  $\text{AOD} \leq 0.2$  at 500 nm and  $\kappa \geq 1$  (440 to 870 nm), indicating small particles.

Measurements during this event were performed with the lidar systems MULIS in Maisach (25 km north-west of Munich) and POLIS in Munich. For the second part of the event (since 30 May, 2008) POLIS was moved to Maisach. The analysis of  $S_p$  in the dust layer ranged from 50 – 70 sr at both wavelengths. In the dust layer unexpectedly large values of the mean  $\delta_p$  up to 0.4 at 355 nm were observed during this event, while  $0.3 \leq \delta_p \leq 0.35$  at 532 nm. However, considering the large systematic errors especially at 355 nm, no significant wavelength dependence of the particle linear depolarization ratio between 355 nm and 532 nm can be found. The unexpected high values at 355 nm may be caused by aging of the dust aerosols during the long-range transport, changing the size distribution of the long-range transported Saharan dust particles.

### Case study 28 May 2008

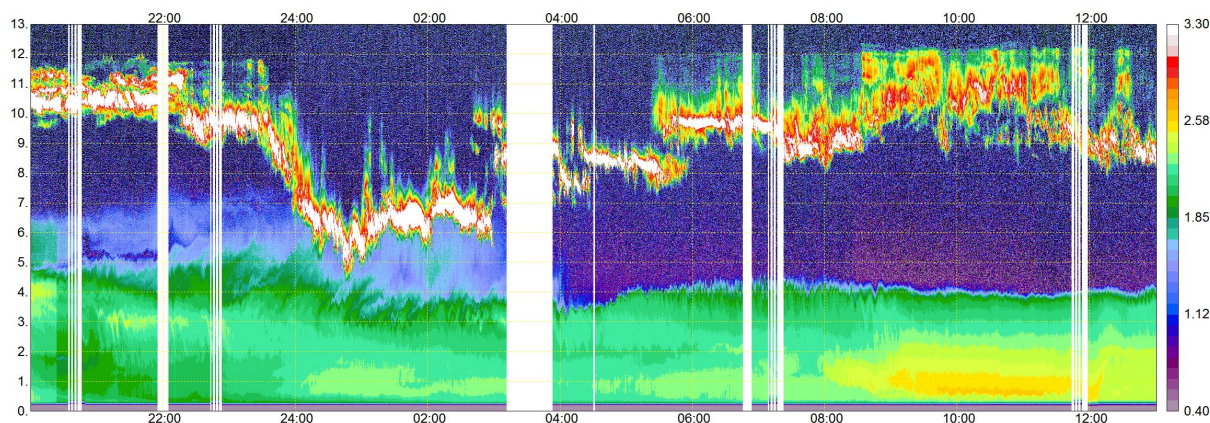


Figure 4.12: Time-height cross section of the range-corrected signal at 1064 nm derived from MULIS lidar measurements at Maisach from 27 May 2008, 20:00 to 28 May 13:00 UTC, for 0 - 13 km above ground level.

Figure 4.12 shows the range-corrected signal of the MULIS measurements at 1064 nm. The time period is from 27 May, 20:00 UTC to 28 May, 13:00 UTC. The blank parts of the image are due to disruptions of the regular measurements required for the calibration of the depolarization channels or adjustments. In the evening of 27 May and into the night to 28 May (about 20:00 - 4:00 UTC) the top of the dust layer was about 5.0 km, with a

thin but still significant aerosol layer up to almost 8.0 km. A cloud layer is visible above 9 km, descending to 5 - 8 km shortly before midnight. After 4:00 UTC the upper layer has disappeared and a sharp upper boundary of the aerosol layer builds up between 4 to 5 km, remaining unchanged until the evening of 28 May. The cloud layer is still present between 7 - 12 km.

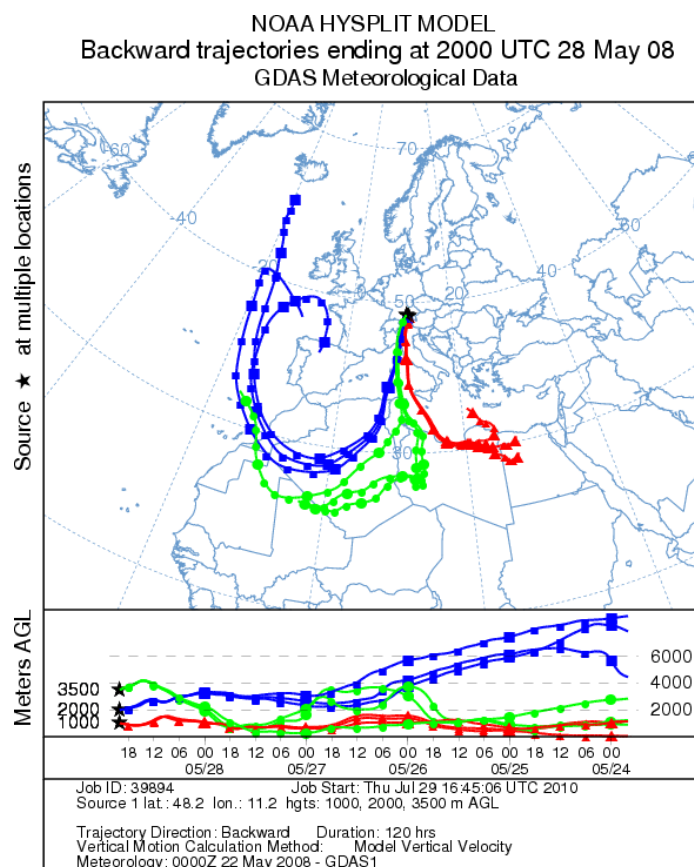


Figure 4.13: 160-h HYSPLIT backward trajectory ending in Munich, Germany on 28 May, 2008 at 20:00 UTC.

According to calculated HYSPLIT backward trajectories (Figure 4.13) the air masses observed in Munich and Maisach originated in the Saharan region. The dust plume traveled 4 - 6 days until it arrived over Southern Germany. The air masses arriving at Munich/Maisach were in contact with the lowermost atmosphere of the Saharan desert, where they could uptake significant amounts of dust.

The time interval 22:40 - 23:40 UTC was selected for Raman-measurements. Averaging over 60 minutes is justified because of the sufficient temporal stability. Due to the low signal-to-noise-ratios of the  $N_2$ -Raman shifted signals at 387nm and 607nm the raw data signals are smoothed with a window length of 87 range-bins and 121 range-bins at 355 nm (POLIS  $\Theta=70^\circ$ ) and 532 nm (MULIS  $\Theta=85^\circ$ ), respectively. Due to technical problems  $S_p$  at 355 nm could only be retrieved from POLIS measurements. For analyses of the particle

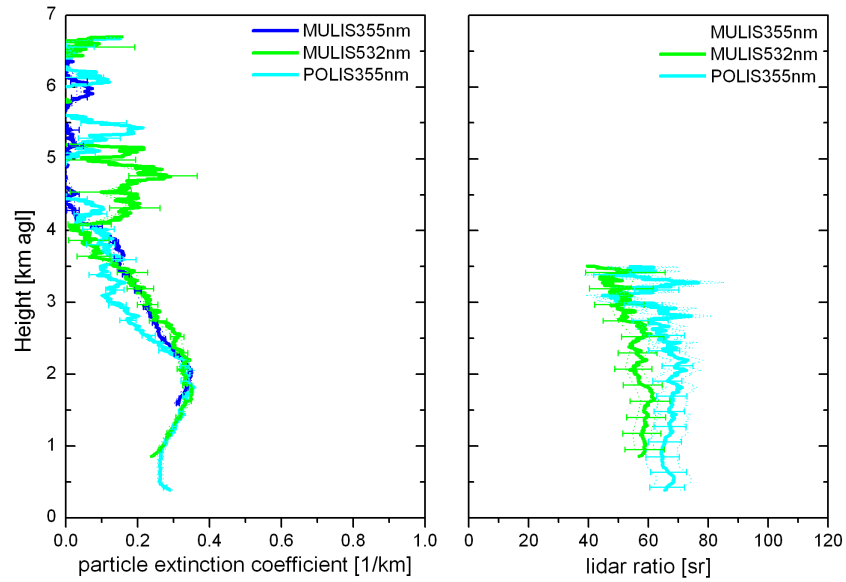


Figure 4.14: Raman measurements of the particle extinction coefficient and lidar ratio on 28 January 2008, 20 UTC at 355 and 532 nm above Maisach. The error bars indicate the statistical errors, the dotted lines the systematic uncertainties.

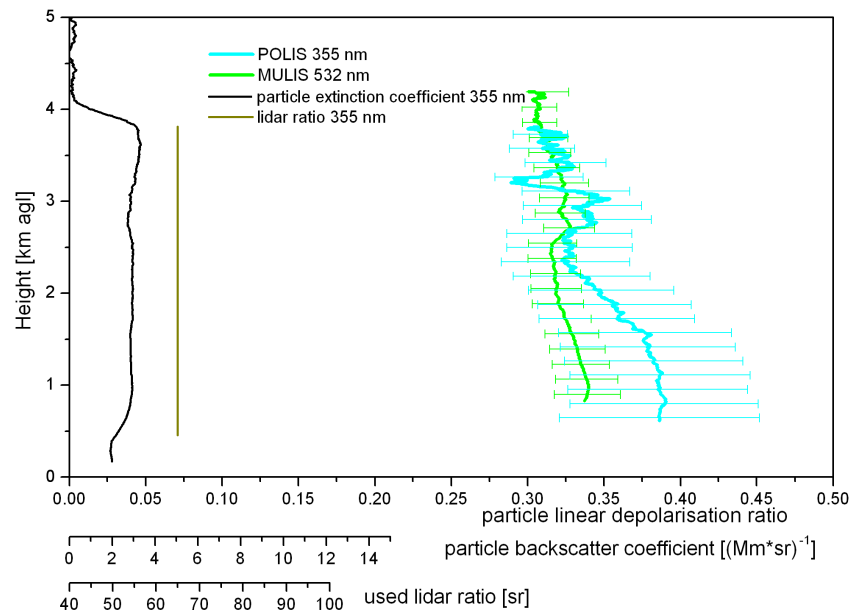


Figure 4.15: Particle linear depolarization ratio on 28 May, 20 UTC at 355 and 532 nm above Munich. The error bars indicate the systematic uncertainties.

linear depolarization ratio the time period 18:00 - 20:00 UTC was chosen. For analysis of the depolarization measurement a smoothing window length of 11 range-bins is chosen at an elevation angle of  $\Theta=85^\circ$  and  $\Theta=69^\circ$  for MULIS and POLIS, respectively.

Note, that MULIS measurements were performed in Maisach (about 25 km north-west of Munich), whereas POLIS was measuring in Munich. Differences in the aerosol distribution, especially in the analysis of  $\delta_p$  may be caused by this spatial distance.

In Figure 4.14 the profiles of  $\alpha_p$  and  $S_p$  at 355 nm (POLIS - cyan and MULIS - blue) and 532 nm (MULIS - green) for the selected time periods are shown. In the dust layer (1.7 - 3.0 km) the AOD was quite high with 0.42, the corresponding Angström exponent was  $0.01 \pm 0.09$ , indicating particles large compared to the laser wavelength. Differences in the profiles of  $\alpha_p$  at 355 nm from POLIS and MULIS measurements can be explained by the spatial distance of the measurements, as mentioned above. The profiles of  $S_p$  are almost constant in the dust layer with mean values  $S_p = 63 \pm 9$  sr at 355nm and  $S_p = 58 \pm 5$  sr at 532 nm. Figure 4.15 shows profiles of  $\delta_p$  at both wavelengths for the selected time period. Again the black line shows the mean particle backscatter coefficient at 355 nm to give an overview over the vertical structure of the layer. The golden line shows the mean lidar ratio  $S_p$  used for the Klett-analysis at 355 nm.  $\delta_p$  profiles at 532 nm are almost constant throughout the dust layer with a mean value of  $0.32 \pm 0.02$ . At 355 nm  $\delta_p$  ranged between 0.28 and 0.39 with a mean value of  $0.35 \pm 0.04$ . Note, the errors denote again the mean systematic error.

#### 4.1.4 Change of optical properties during transport

Measurements in high dust loaded air masses during both SAMUM field campaigns and during a strong Saharan dust event over Europe allow the examination of changes in the optical properties of Saharan dust during transport. For this examination the intensive properties, the lidar ratio  $S_p$  and the particle linear depolarization ratio  $\delta_p$  are used, because they are dependent on micro-physical and chemical properties of the examined type of aerosol and not on its concentration.  $S_p$  is analyzed at two wavelengths (355 nm and 532 nm) with the lidar systems MULIS and POLIS.  $\delta_p$  is analyzed at three wavelength (355 nm, 532 nm and 710 nm) during the SAMUM campaigns and at two wavelengths (355 nm and 532 nm) during the Saharan dust event over Munich/Maisach.

Figure 4.16 shows the mean values of  $\delta_p$  in the pure Saharan dust layers for selected days of the three events. It can be seen, that the systematic errors of  $\delta_p$  at 355 nm and 710 nm were large during the first SAMUM field campaign. During SAMUM-1 the errors prohibit a conclusion about wavelength dependence of pure fresh Saharan dust. The most significant result of  $\delta_p$ -measurements is the mean  $\delta_p$  of  $0.31 \pm 0.01$  at 532 nm from MULIS measurements.  $\delta_p$  at 355 nm could be between 0.17 and 0.32 and at 710 nm between 0.18 and 0.40. The modifications of POLIS and Bertha between both SAMUM campaigns result in a reduction of the systematic errors of  $\delta_p$  for both systems, so that an analysis of the wavelength dependence is now possible for pure Saharan dust at the beginning of its long range transport. A significant wavelength dependence of increasing mean  $\delta_p$ -values with increasing wavelengths is obvious. The mean values for the whole measurements during

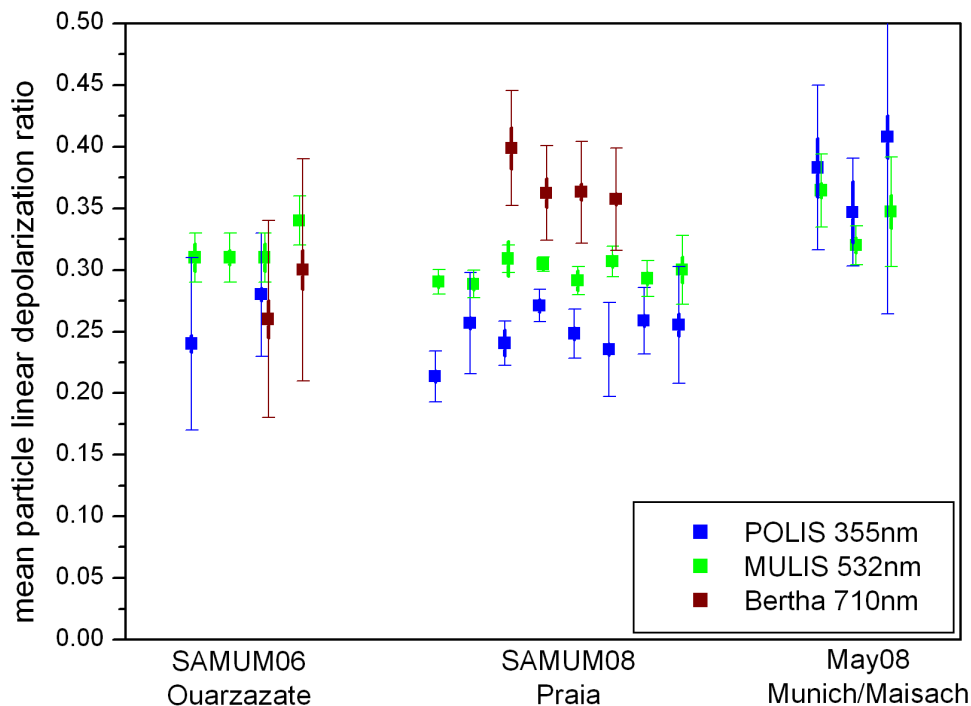


Figure 4.16: Mean  $\delta_p$ -values of pure Saharan dust layers for selected days during SAMUM-1, SAMUM-2, and during a strong Saharan dust event over Munich/Maisach at wavelengths as indicated. The error bars denote the mean systematic error, the thick bars the standard deviation of the mean.

SAMUM-2 are  $\delta_p = 0.25 \pm 0.02$  at 355 nm,  $\delta_p = 0.30 \pm 0.01$  at 532 nm, and  $\delta_p = 0.36 \pm 0.04$  at 710 nm. The errors are again the mean systematic errors. Comparing the mean values and the systematic errors of both campaigns, no changes can be seen of pure fresh Saharan dust and pure Saharan dust at the beginning of its long-range transport with respect to  $\delta_p$ , within the error bars. Regarding the mean  $\delta_p$  values of the analysis of the measurements performed in Munich and Maisach during a strong Saharan dust event of  $\delta_p = 0.38 \pm 0.09$  at 355 nm and  $\delta_p = 0.34 \pm 0.03$  at 532 nm, one can see significant changes in the mean  $\delta_p$  values at 355 nm. The mean values at both wavelengths are higher than the mean values during the SAMUM-Project, but  $\delta_p$  at 532 nm agrees well with former measurement within the error bars. Although the errors at 355 nm for the Munich measurements are very large, there is a significant difference to the values found during SAMUM-2, with higher values for the long-range transported Saharan dust. A wavelength dependence between 355 nm and 532 nm is no longer obvious.

In Figure 4.17 the mean values of  $S_p$  of the pure dust layers for selected days during

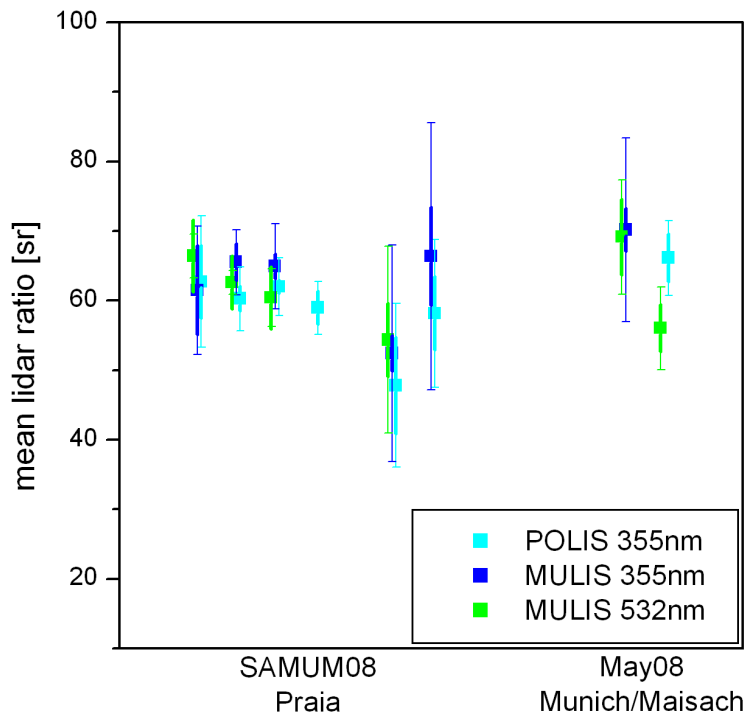


Figure 4.17: Mean  $S_p$ -values of pure Saharan dust layers for selected days during SAMUM-2 and during a strong Saharan dust event over Munich/Maisach at wavelengths as indicated. The error bars denote the mean systematic error, the thick bars the standard deviation of the mean.

Table 4.1: Optical properties of pure fresh, pure short-range transported and pure long-range transported Saharan dust. The mean values are the averages of the layer mean values of all analyses during the period, the range denotes the maximum and minimum mean values of all analysis.

	$\delta_p$ <b>355 nm</b>	$\delta_p$ range	$S_p$ [sr] <b>355 nm</b>	$S_p$ range [sr]	type
SAMUM-1	0.25	0.22 - 0.26	55	47 - 60	fresh pure dust
SAMUM-2	0.25	0.21 - 0.26	58	48 - 63	aged pure dust
Munich 2008	0.38	0.35 - 0.41	68	60 - 70	long-range transp. dust
	$\delta_p$ <b>532 nm</b>	$\delta_p$ range	$S_p$ [sr] <b>532nm</b>	$S_p$ range [sr]	type
SAMUM-1	0.31	0.29 - 0.31	56	47 - 62	fresh pure dust
SAMUM-2	0.30	0.29 - 0.31	61	56 - 66	aged pure dust
Munich 2008	0.34	0.31 - 0.36	59	53 - 69	long-range transp. dust

SAMUM-2 and during the strong Saharan dust event over Munich/Maisach are shown. These values can not be compared to mean dust values for selected days during SAMUM-

1, as the corresponding data are not available. During the second campaign of the SAMUM project,  $S_p$  values between 355 nm and 532 nm are independent of wavelength and mainly ranged between 50 sr and 70 sr. At the end of the campaign, the errors of  $S_p$  increased due to a reduced aerosol load in this layer. Regarding  $S_p$  measured over Munich/Maisach during a strong dust event, no significant changes of  $S_p$  are obvious. A wavelength dependence of  $S_p$  for long-range transported Saharan dust can not be seen within the error bars. Looking at the mean values of the retrieved lidar ratios  $S_p$  for Saharan dust, slightly higher mean values are found during SAMUM-2 compared to the results of SAMUM-1 for 355 nm as well as for 532 nm. The mean  $S_p$  values reported for the first SAMUM field campaign are  $S_p = 55 \text{ sr} \pm 5 \text{ sr}$  at 355 nm and  $S_p = 56 \text{ sr} \pm 5 \text{ sr}$  at 532 nm. These values are results of the analysis of Bertha measurements and can be found in Tesche et al. (2009a). During SAMUM-2  $S_p = 58 \text{ sr} \pm 8 \text{ sr}$  at 355 nm and  $S_p = 61 \text{ sr} \pm 5 \text{ sr}$  are found for analyses of the POLIS- and MULIS-measurements. The mean values for pure dust long-range transported to Europe are  $S_p = 68 \text{ sr} \pm 9 \text{ sr}$  at 355 nm and  $S_p = 59 \text{ sr} \pm 6 \text{ sr}$  at 532 nm.

The mean values found during the second field campaign are slightly higher than the one found during the first. It has to be kept in mind, that measurements of different lidar systems are used for the analysis of the particular values. An offset in one of the analyses and/or both is not impossible and could cause the differ of the mean values. Another possibility are small changes in the micro-physical parameters of the dust particles, or a mixing with other types of aerosols during transport. However, although the mean values of both campaigns show a slight difference, they match within the error bars. A significant difference of  $S_p$  in the first few days of transport can not be seen. Considering also the mean values found for long-range transported dust, the mean  $S_p$  at 355 nm shows even a slightly higher value ( $65 \pm 9 \text{ sr}$ ) than found during SAMUM-2, but the errors are very large and so this difference is not significant. The mean values of all considered analysis and their maximum and minimum values are outlined in Table 4.1.

## 4.2 Biomass burning aerosols

The atmosphere during the second campaign of the SAMUM project showed a multi-layer structure. This provides the opportunity to study biomass burning aerosols. Almost during the whole campaign there were lofted aerosol layers above 1.5 km, consisting of biomass burning aerosols with a possible dust contribution. High aerosol loaded air-masses, released in the fire regions of the Sahel, were advected over the Atlantic Ocean and the Cape Verde Islands. In these air masses Lieke et al. (2011) found large amounts of soot and other biomass burning material, probably mixed with some dust from thermal uptakes.

Due to the multi-layer structure, sun-photometer measurements of AOD and  $\kappa$ , can not be used to identify these mixed layers without further information. For small biomass burning aerosols  $\kappa \approx 1.5$  (Holben et al., 2001) would be expected. Those high values were not observed during SAMUM-2. However  $\kappa$  of about  $0.5 \leq \kappa \leq 0.8$  (see Figure 4.6) observed with the SSARA sun-photometer indicates a mixture and/or layering of large and small particles. This  $\kappa$ -range could be observed quite often during SAMUM-2, except on



days with high dust load (afternoon of 28 January to afternoon of 30 January 2008) and low aerosol concentration (9 February 2008).

The mixed biomass burning layers ranged from minimum 1.5 km for the lower boundary to maximum 5 km for the top of the layer. Mean  $S_p$  observed in these layers are  $S_p = 76 \text{ sr} \pm 12 \text{ sr}$  (65 - 102 sr) at 355 nm and  $S_p = 66 \text{ sr} \pm 11 \text{ sr}$  (61 - 90 sr) at 532 nm. It is found that  $S_p$  at 532 nm is either slightly lower than at 355 nm (just outside the error bars) or no wavelength dependence of  $S_p$  can be found. The corresponding  $\delta_p$  of these layers varied from 0.12 to 0.2 at all three wavelengths (355 nm, 532 nm and 710 nm), with a wavelength independent mean value over the whole period of  $\delta_p = 0.16$ . On specific days  $\delta_p$  at 532 nm shows lower values compared to 355nm. One reason of the spectral behavior of  $S_p$  and  $\delta_p$  is, that air masses from areas with forest fires consist of a variety of different types of aerosols. Furthermore the mixture of biomass burning aerosols is not homogeneous throughout the measurement time.

As an example for the multi-layering structure and the values of the biomass burning smoke mixture profiles of 30 January 2008 are shown and discussed in the following.

### Case study 30 January 2008

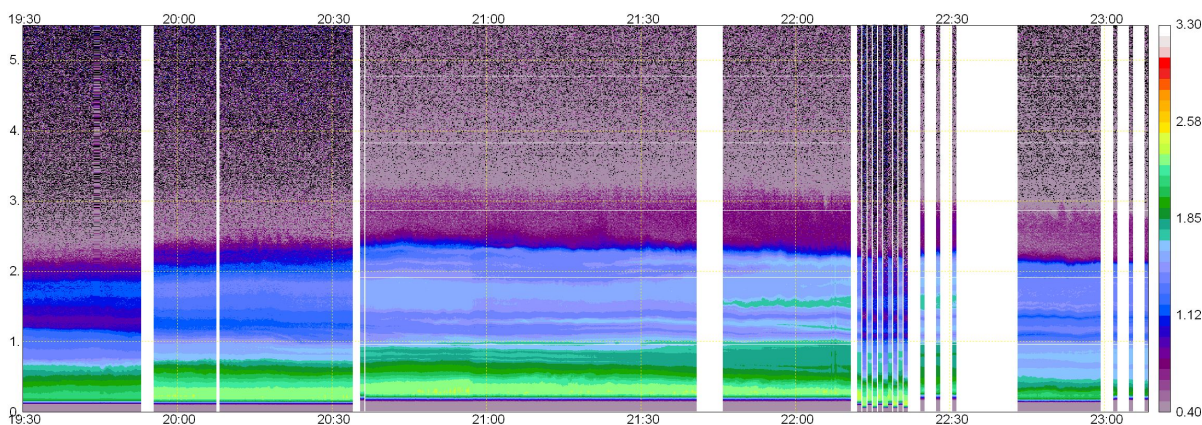


Figure 4.18: Time-height cross section of the range-corrected signal at 1064 nm derived from MULIS lidar measurements at Praia from 30 January 2008, 19 UTC – 23:10 UTC, for 0 - 5.5 km above ground level.

The range corrected signal of MULIS measurements at 1064 nm is shown in Figure 4.18 from 19:00 to 22:10 UTC. It shows a three layer structure with a boundary layer reaching up to 0.5 km, an overlaying dust layer from 0.5 to about 1 km and a lofted layer consisting of a mixture of biomass burning aerosols and dust above about 1.2 km. Throughout the measurement time, the atmosphere showed a stable layering. Backward trajectories (Figure 4.19) indicate the Saharan desert as source region for the air-masses up to 1.0 km with

a possible mixing of dust and marine aerosols in the boundary layer. The upper layer is mainly dominated by biomass burning aerosols from Western Africa.

For the evaluation of the optical parameters three time intervals were chosen. For the analysis of  $S_p$  the time period from 20:35 - 22:30 UTC is used, for the analysis of  $\delta_p$  at 532 nm and 710 nm the time interval is 22:59 - 23:59 UTC and at 355 nm it was 18:00 - 20:00 UTC. The temporal stability during and between these time intervals is sufficient, as can be seen from Fig. 4.18. So the results of the chosen time intervals are well combinable. The smoothing window length for the analysis of the particle linear depolarization ratio  $\delta_p$  is 11 range-bins at  $\Theta=79^\circ$  and  $\Theta=87^\circ$  for POLIS and MULIS, respectively. The range-resolution of Bertha signals is again 60 m at  $\Theta=90^\circ$ . For the analysis of the Raman measurements smoothing with a window length of 87 range-bins is necessary.

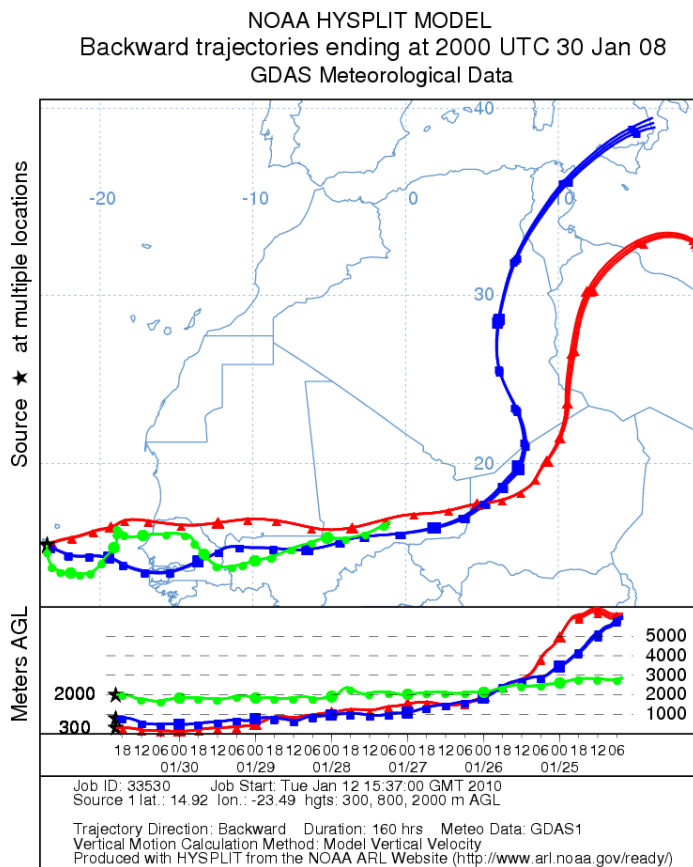


Figure 4.19: 160-h HYSPLIT backward trajectory ending in Praia on 30 January 2008 at 20:00 UTC.

Figures 4.20 and 4.20 show that in the upper layer (above 1.5 km)  $\alpha_p$ , as well as  $S_p$  are wavelength dependent, with larger values at 355 nm. The mean values are  $S_p = 87 \text{ sr} \pm 8 \text{ sr}$  at 355 nm for POLIS measurements, and  $S_p = 78 \text{ sr} \pm 5 \text{ sr}$  at 355 nm and  $S_p = 67 \text{ sr} \pm 5 \text{ sr}$  at 532 nm for MULIS-measurements. The mean  $\kappa$  in this layer (1.2 - 2 km) is about  $1.04 \pm 0.23$ , indicating small particles.  $\delta_p$  shows no wavelength dependence within the

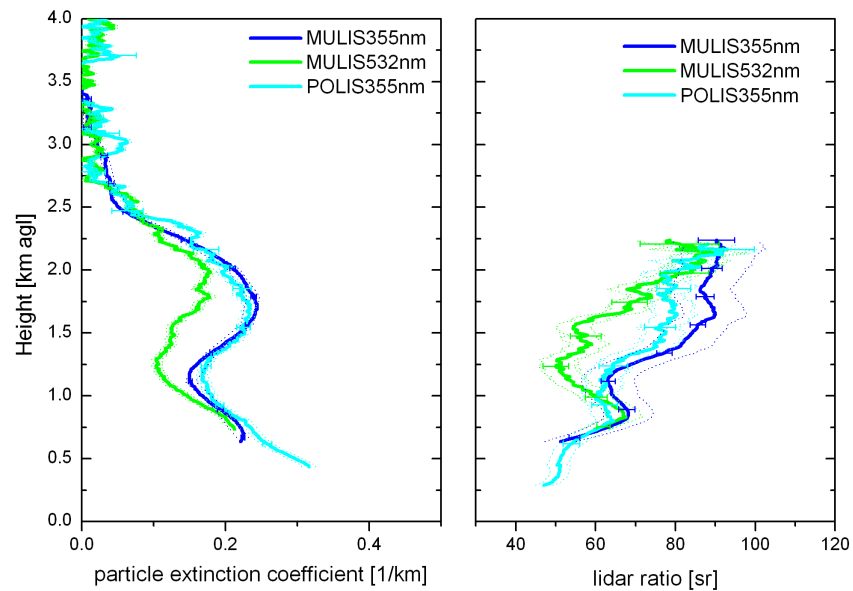


Figure 4.20: Raman measurements of the particle extinction coefficient and lidar ratio on 30 January 2008, 20:35 - 22:30 UTC at 355 and 532 nm above Praia. The error bars indicate the statistical errors, the dotted lines the systematic uncertainties.

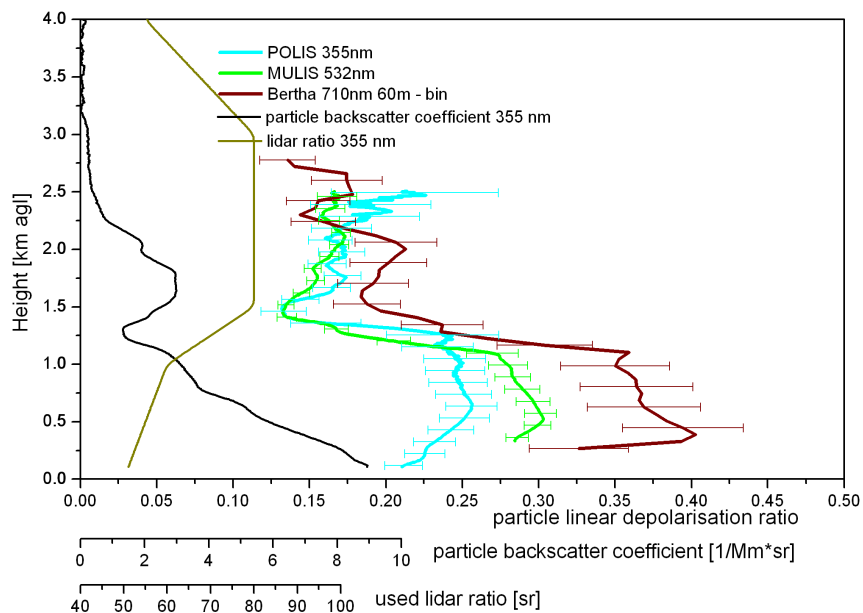


Figure 4.21: Particle linear depolarization ratio on 30 January, 18:00 - 20:00 UTC at 355 nm (POLIS), and 20:35 - 22:30 UTC at 532 nm and 710 nm above Praia. The error bars indicate the systematic uncertainties. The POLIS backscatter coefficient was calculated with the Fernald algorithms using the lidar ratio retrieved from simultaneous Raman measurements

error bars. The layer mean values are  $\delta_p = 0.17 \pm 0.02$  at 355 nm,  $\delta_p = 0.16 \pm 0.01$  at 532 nm, and  $\delta_p = 0.18 \pm 0.03$  at 710 nm. This layer consists of biomass burning aerosols with a possible contribution of dust particles. Neither  $\alpha_p$  nor  $S_p$  show a wavelength dependence in the dust layer. The layer mean values are  $S_p = 60 \text{ sr} \pm 4 \text{ sr}$  (POLIS) and  $S_p = 64 \text{ sr} \pm 6 \text{ sr}$  (MULIS) at 355 nm, and  $S_p = 60 \text{ sr} \pm 4 \text{ sr}$  at 532 nm (MULIS).  $\delta_p$  is wavelength dependent with  $\delta_p = 0.25 \pm 0.02$  at 355 nm,  $\delta_p = 0.29 \pm 0.01$  at 532 nm, and  $\delta_p = 0.36 \pm 0.04$  at 710 nm. In the boundary layer ( $\leq 0.5 \text{ km}$ )  $S_p$  and  $\delta_p$  can only be retrieved from POLIS-measurements at 355 nm with a layer mean value of  $S_p = 50 \pm 2 \text{ sr}$  and  $\delta_p = 0.22 \pm 0.01$ , again indicating a contribution of marine aerosols in this layer.

### 4.3 Marine aerosols

During several days during SAMUM-2 (3 - 9 February 2008), northern and north-easterly flow from the nearby coast, together with high wind velocity, activated and advected marine aerosols over the measurement site at Praia. This provides the opportunity to study the optical properties of marine aerosols in the boundary layer below 0.5 km. The relative humidity in these layers ranged between 60 – 90 %, suggesting dissolved sea salt particles.

Analysis of the lidar measurements result in wavelength independent mean  $S_p$  of  $S_p = 18 \pm 5 \text{ sr}$  (14 sr - 18 sr) at 355 nm, and  $S_p$  of  $S_p = 18 \pm 2 \text{ sr}$  (17 sr - 19 sr) at 532 nm for marine aerosols.  $\delta_p$  ranged independent of wavelength between 0.02 and 0.05 with a mean value of  $\delta_p = 0.02 \pm 0.01$  at 355 nm and  $\delta_p = 0.02 \pm 0.02$  at 532 nm. Analysis at 710 nm can not be done. As an example, the analysis of the boundary layer on 05 February 2008 is shown in the following.

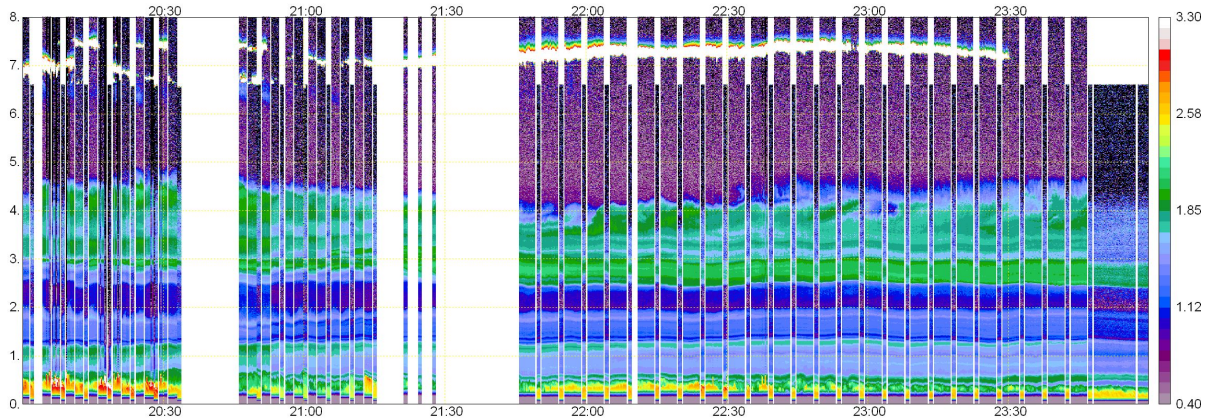


Figure 4.22: Time-height cross section of the range-corrected signal at 1064 nm derived from MULIS lidar measurements at Praia on 05 February 2008, 20:00 – 24:00 UTC, for 0 - 8 km above ground level.

## Case study 05 February 2008

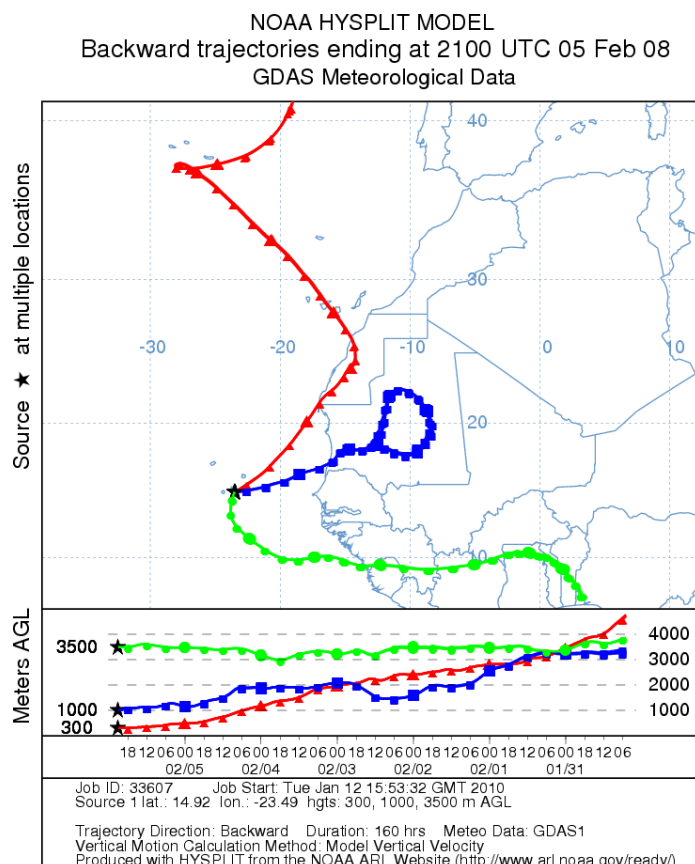


Figure 4.23: 160-h HYSPLIT backward trajectories ending in Praia, Cabe Verde Islands on 05 February 2008, 21:00 UTC.

Figure 4.22 shows the range corrected signal at 1064 nm measured with MULIS on 05 February (20:00 - 24:00 UTC). It clearly shows a three layer structure with a boundary layer in the lowermost 0.5 km, and two lofted layers from 0.5 - 2.0 km the lower one, and 2.8 - 4.5 the upper one. A cloud layer is visible in 6 - 9 km. The columnar structure of the plot is again due to scanning. As the marine boundary layer is of interest at that day, the focus is on the analyses of the lowermost 0.5 km in the analysis only.

Backward trajectories (Figure 4.23) show, that the air masses in the boundary layer were advected with north-easterly flow from the Atlantic Ocean. The wind velocity on this day was high, leading to the assumption that this layer consists of a high amount of marine aerosols. In the layer between 0.5 and 2.5 km the Saharan desert was located as source region and for the lofted layers the fire region in the Sahel.

As mentioned above, the focus is only on the lowermost 0.5 km of that day, to evaluate the optical properties of the marine boundary layer. The analysis below 0.5 km (Fig. 4.24 and 4.25) can be done at two wavelengths (355 nm and 532 nm) as MULIS measurements were performed under an elevation angle of 20°. The elevation angle of POLIS

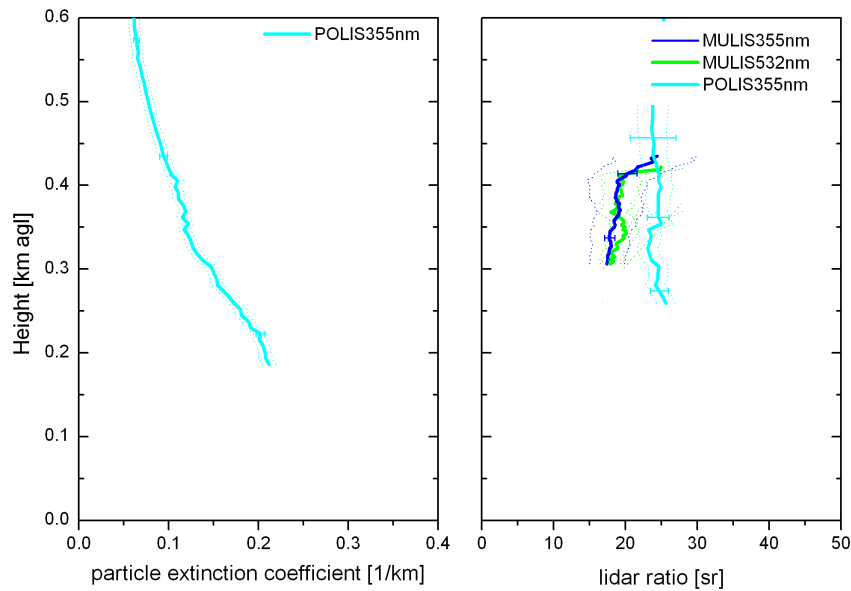


Figure 4.24: Raman measurements of the particle extinction coefficient and lidar ratio on 05 February 2008, 20:30 - 22:30 UTC at 355 and 532 nm above Praia. The error bars indicate the statistical errors, the dotted lines the systematic uncertainties.

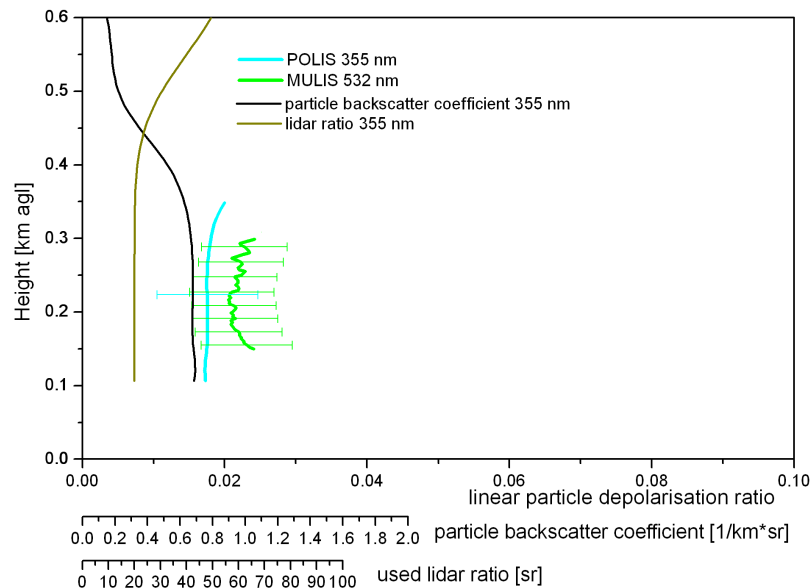


Figure 4.25: Particle linear depolarization ratio on 05 February, 21:00 UTC at 355 nm and 532 nm above Praia. The error bars indicate the systematic uncertainties. The POLIS backscatter coefficient was calculated with the Fernald algorithms using the lidar ratio retrieved from simultaneous Raman measurements.

measurements was  $79^\circ$ . The selected time periods are 20:30 - 23:45 UTC for analysis of the Raman-measurements and the linear depolarization ratio  $\delta_p$  at 532 nm from MULIS measurements, and 18:00 - 20:00 UTC for the analysis of  $\delta_p$  from POLIS-measurements. The smoothing-window length for the depolarization analysis is 11 range-bins, for the Raman method it is 87 range-bins below 0.5 km for POLIS measurements, and of 53 range-bins for MULIS measurements. The mean  $S_p$ , found in the boundary layer, are  $S_p = 24 \text{ sr} \pm 6 \text{ sr}$  (23 sr – 26 sr) (POLIS), and  $S_p = 19 \text{ sr} \pm 2 \text{ sr}$  (17 sr – 23 sr) (MULIS) at 355 nm, and  $S_p = 19 \text{ sr} \pm 2 \text{ sr}$  (18 sr – 24 sr) (MULIS) at 532 nm. The corresponding values of  $\delta_p$  are  $\delta_p = 0.02 \pm 0.01$  at 355 nm and  $\delta_p = 0.02 \pm 0.01$  at 532 nm, indicating low depolarizing aerosols, probably a liquid sea salt dominance.

## 4.4 Volcanic ash particles

On 14 April 2010 explosive eruptions of the Eyjafjallajökull (63.63 N, 19.63 W) started. The ash plumes reached heights up to 8 km. A north-westerly flow transported ash loaded air-masses to Central Europe. The volcanic plume could first be detected on 16 April at about 17 UTC in heights from 5 km – 7 km over Maisach. It descended to 4 km at midnight and to less than 2.5 km after 11 UTC the next day, mainly due to subsidence of the air mass (Wiegner et al., 2011). After 16:00 UTC the volcanic plume started to entrain into the boundary layer. The maximum extinction coefficient of the plume was measured around 7:00 UTC on 17 April in about 2.0 km – 2.4 km with wavelength independent values as high as  $0.75 \text{ km}^{-1}$ . From 16 April to 25 April volcanic aerosols could be found throughout the troposphere, in lofted layers or mixed into the boundary layer.

### 4.4.1 Pure volcanic ash

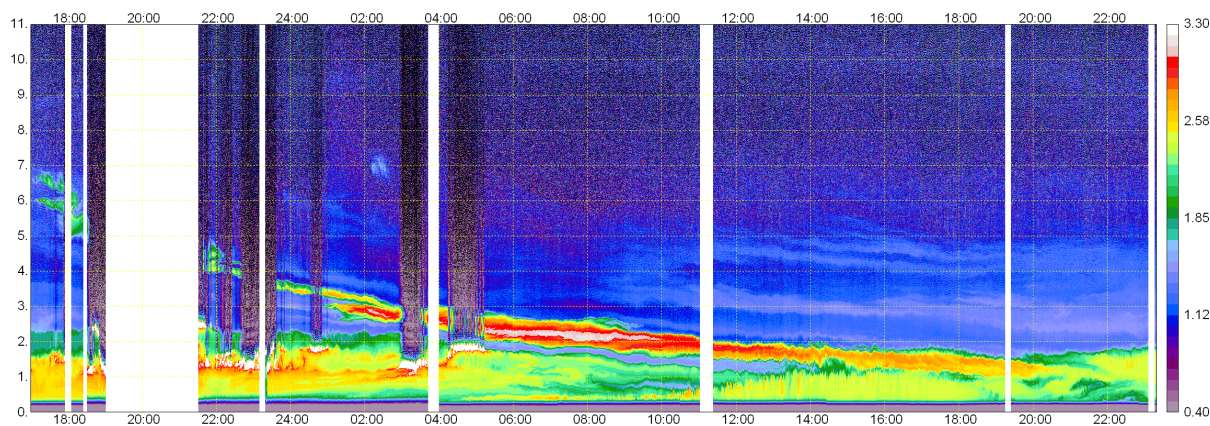


Figure 4.26: Time-height cross section of the range-corrected signal at 1064 nm derived from MULIS lidar measurements at Maisach from 16 April, 2010, 17:00 UTC to 17 April 24:00 UTC, for 0 - 11 km above ground level.

### Case study 17 April 2010

Figure 4.26 displays the temporal development of the volcanic plume over Maisach from 16 April 17:00 UTC to 17 April 24:00 UTC as detected by MULIS; shown is the range corrected signal at 1064 nm. Rain and clouds on top of the boundary layer prevented the monitoring of the volcanic plume only during short time periods (blank areas).

HYSPLIT backward trajectories (Figure 4.27) demonstrated that the origin of the lofted layer – here shown for 17 April at 2:00 UTC at an altitude of 2.8 km (green line) was located in Iceland.

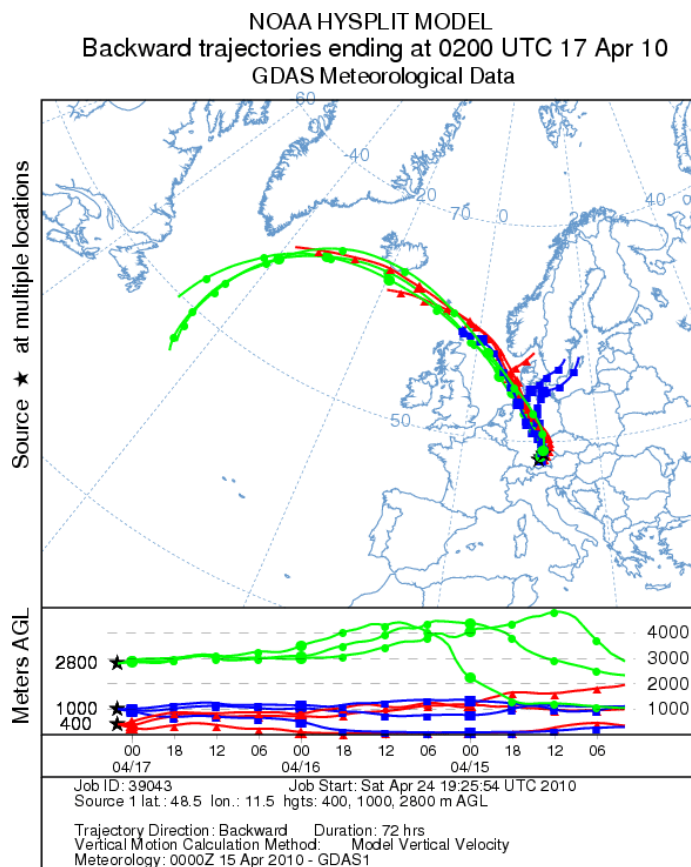


Figure 4.27: 72-h HYSPLIT backward trajectories ending in Munich, Germany on 17 April, 2010 at 2:00 UTC

The raw data of the lidar systems are smoothed with a window length of 11 range-bins for the depolarization analysis, and to 41 range-bins for the Raman analysis. The measurements were performed under an elevation angle of  $79^\circ$  and  $85^\circ$  for POLIS and MULIS, respectively. For the night measurement the signals are averaged between 01:30 – 02:40 UTC.

The layer of volcanic aerosols at 2.6 – 3.5 km shows no wavelength dependence of  $\alpha_p$  at 355 nm and 532 nm within the error bars (Figure 4.28), the mean Angström exponent



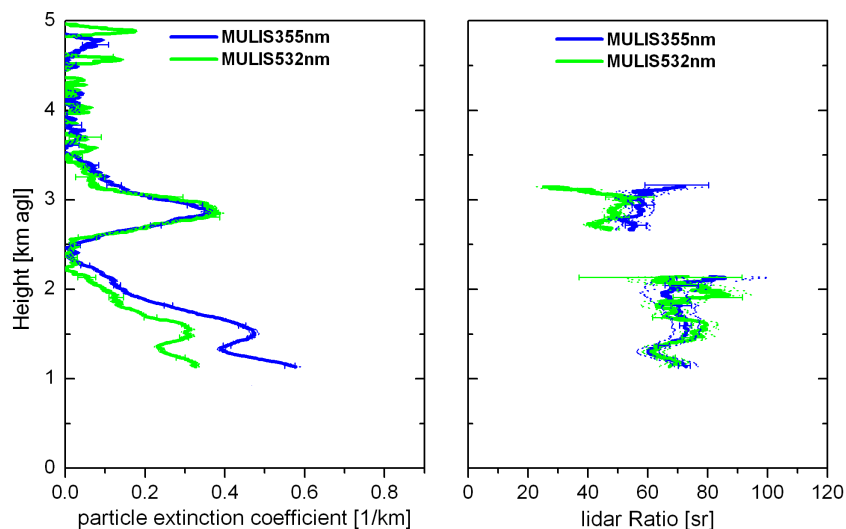


Figure 4.28: Raman measurements of the particle extinction coefficient and lidar ratio on 17 April 2010, 1:30 - 2:40 UTC at 355 and 532 nm above Maisach. The error bars indicate the statistical errors, the dotted lines the systematic uncertainties.

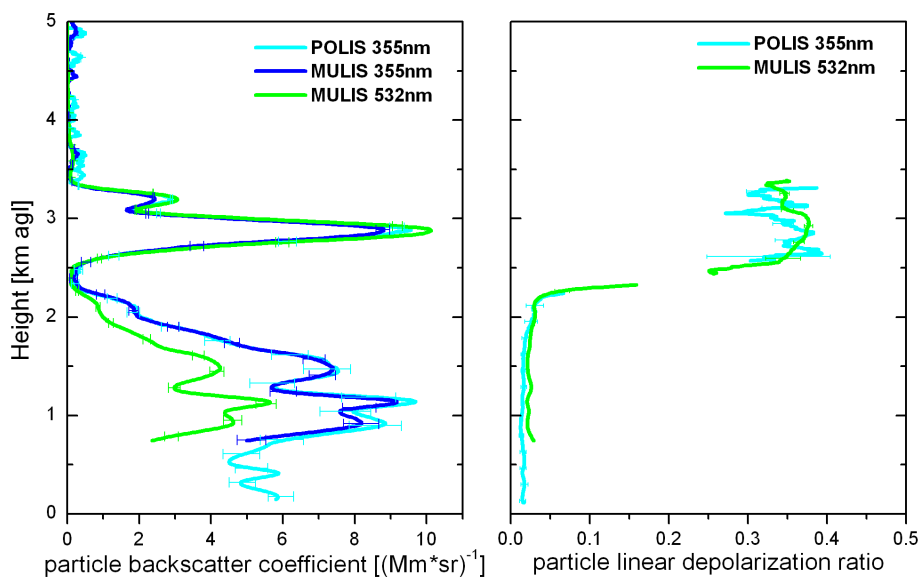


Figure 4.29: Particle backscatter coefficient, and particle linear depolarization ratio at 355 nm and 532 nm on 17 April 2010 1:40 - 2:30 UTC derived from POLIS- and MULIS-measurements, respectively. The error bars indicate the systematic errors.

( $\kappa$ ) (not shown) is  $\kappa = -0.11 \pm 0.18$ , indicating large particles.

The profiles of the particle backscatter coefficient  $\beta_p$  (Figure 4.29) in the volcanic layer show the same spectral behavior as  $\alpha_p$ . As a consequence, the lidar ratio is height-independent within the volcanic layer. Although it seems that in the dust plume  $\alpha_p$  and  $\beta_p$  at the wavelength 532 nm show slightly higher values than at 355 nm, they match the others within the error bars. To get the linear depolarization ratio at 355 nm additional measurements with POLIS were performed. This implies the retrieval of  $\beta_p$  at 355 nm (see Equation 2.32). Measurements of  $\beta_p$  of both systems show an excellent agreement. The particle linear depolarization ratio  $\delta_p$  in the lofted layer are  $0.35 \leq \beta_p \leq 0.38$  and wavelength independent, with layer mean values of  $\delta_p = 0.35 \pm 0.02$  at 355 nm and  $\delta_p = 0.37 \pm 0.02$  at 532 nm. These high values clearly indicate non-spherical particles and suggest a high fraction of glass- and mineral aerosols. The optical properties of the boundary layer (1.0 – 2.2 km) below the ash plume are considerably different: The spectral dependence of  $\alpha_p$  is significant, with  $\alpha_p$  at 355 nm being larger than at 532 nm. The corresponding  $\kappa$ , averaged over the boundary layer, is  $\kappa = 1.3 \pm 0.5$ , which indicates rather small particles. The corresponding  $S_p$  ranged between  $60 \text{ sr} \leq S_p \leq 80 \text{ sr}$  and does not depend on wavelength (within the error bars of the retrieval).  $\delta_p$  shows wavelength independent low values between 0.01 and 0.02.

#### 4.4.2 Volcanic ash and sulfuric acid mixed with boundary layer aerosols

##### Case study 20 April 2010

Figure 4.30 shows the measurements of 20 April with the MULIS system. Plotted is again the range-corrected signal at 1064 nm.

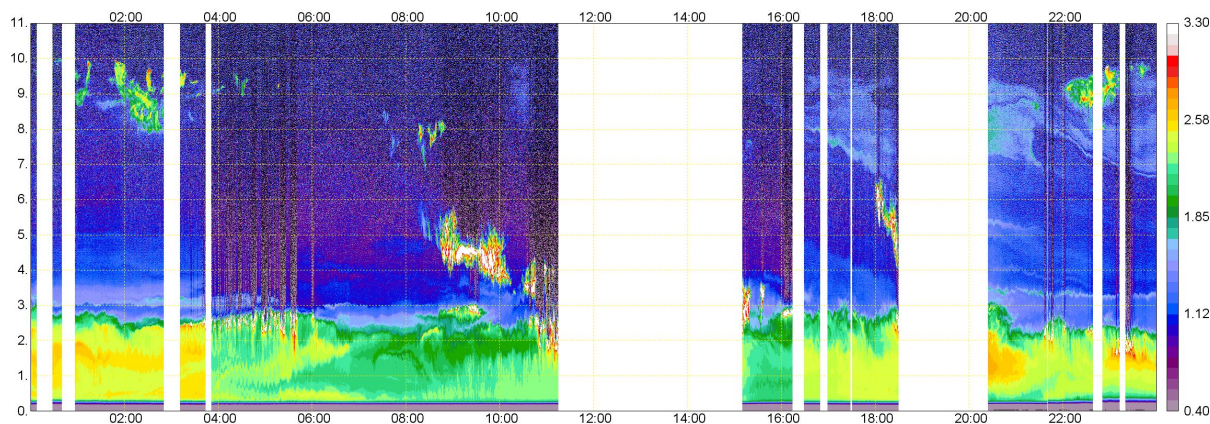


Figure 4.30: Time-height cross section of the range-corrected signal at 1064 nm derived from MULIS lidar measurements at Maisach from 20 April 2010, 0:00 UTC – 24:00 UTC.

In the morning,  $\delta_v$  (larger than 0.1 at 532 nm) indicates volcanic particles mixed into the boundary layer up to about 2.9 km (not shown). In the afternoon and at nighttime ash was also visible in the upper troposphere as optically thin filaments up to 10 km. This finding is supported from back-trajectory analysis (Figure 4.31 – red and blue lines) showing that the origin of the air-masses was again Iceland.

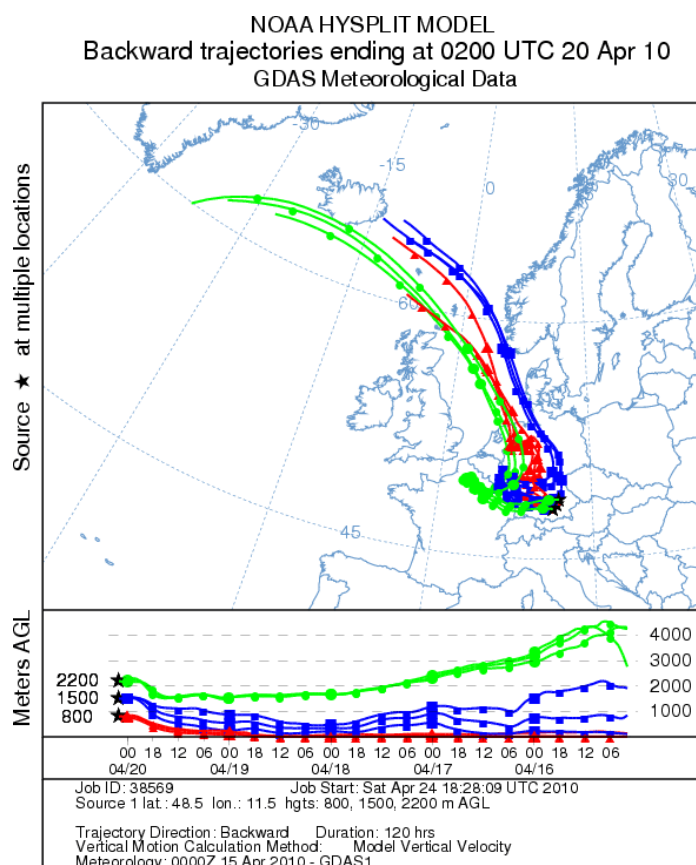


Figure 4.31: 120-hours HYSPLIT backward trajectory ending in Maisach on 20 April, 2010 2:00 UTC.

For 20 April the time period from 01:00 UTC to 02:50 UTC was selected for the characterization of the aerosol layers. The smoothing window length is again 11 range-bins for the depolarization measurements and 41 range-bins for the Raman analysis.

For the selected time period, the focus is on two height ranges, the first between 0.5 km and 1.2 km, the second between 1.5 km and 2.4 km. Though both are part of the boundary layer they show quite different optical properties. The wavelength dependence of  $\alpha_p$  (derived with the Fernald/Klett method) is described by a mean Angström exponent of  $\kappa = 1.5 \pm 0.1$  and  $\kappa = 1.1 \pm 0.4$  in the lower and upper layer, respectively, suggesting larger particles in the upper layer. The corresponding lidar ratio  $S_p$  is wavelength independent and rather low with  $35 \text{ sr} \leq S_p \leq 50 \text{ sr}$  in the lower layer increasing to  $45 \text{ sr} \leq S_p \leq 60 \text{ sr}$  in the upper layer (Fig. 4.33).

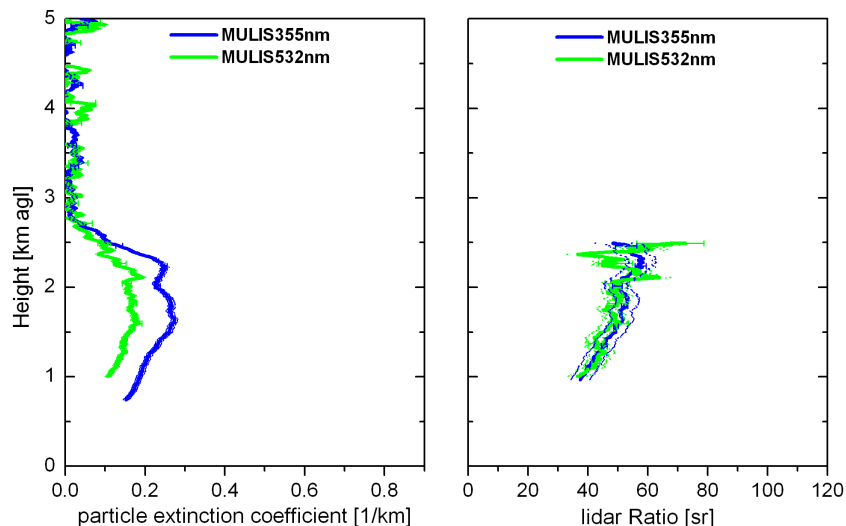


Figure 4.32: Raman measurements of the particle extinction coefficient and lidar ratio on 20 April 2010, 01:00 - 02:50 UTC at 355 nm and 532 nm above Maisach. The error bars indicate the statistical errors, the dotted lines the systematic uncertainties.

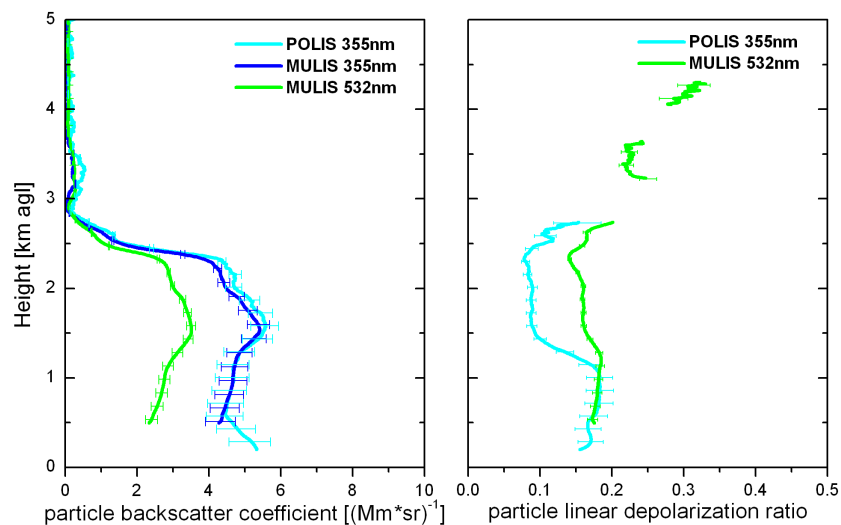


Figure 4.33: Particle backscatter coefficient at 355 nm, 532 nm and 1064 nm, and particle linear depolarization ratio at 355 nm and 532 nm for 20 April 2010 01:00 - 02:50 UTC derived from POLIS- and MULIS-measurements at an elevation angle of 75° and 85°, respectively. The smoothing window-length was 80 m. The error bars indicate the systematic errors.

The most interesting feature of the optical characterization is, however, the depolarization ratio. The profiles of  $\delta_p$  (Figure 4.33) within the lower layer (below 1.2 km) show no wavelength dependence with mean values of  $0.18 \pm 0.02$ . In the upper layer the profiles of  $\delta_p$  at both wavelengths are clearly different with mean values of  $0.08 \pm 0.01$  at 355 nm and  $0.16 \pm 0.01$  at 532 nm.

Above the boundary layer only  $\delta_p$  at 532 nm (MULIS data) can be retrieved and shows values larger than 0.2, indicating that volcanic aerosols are also present in the free troposphere.



# Chapter 5

## Discussion

### 5.1 Review of $S_p$ and $\delta_p$

Most values of the particle linear depolarization ratio  $\delta_p$  of mineral dust reported in literature are in the range of 0.1 – 0.25 at 532 nm (e.g. Chen et al. 2007; Ansmann et al. 2003; Murayama et al. 2004), describing long-range transported dust or dust mixed with other types of aerosols. Measurements in fresh dust close to the Taklimakan desert (Iwasaka et al., 2003) or of fresh Gobi dust (e.g. Murayama et al. 2004) showed larger values of  $0.27 \leq \delta_p \leq 0.35$  at 532 nm. Liu et al. (2008b) presented an analysis of spaceborne lidar measurements (CALIOP) with mean  $\delta_p$  values of about 0.32 at 532 nm for a case study of a Saharan dust plume transported over the Atlantic ocean. Measurements at four wavelengths of fresh Saharan dust during SAMUM-1 were presented in Freudenthaler et al. (2009) with a mean value of  $0.27 \leq \delta_p \leq 0.35$  at 532 nm. These  $\delta_p$  values of fresh Saharan dust are in good agreement with results for mean  $\delta_p$  during SAMUM-2 of  $0.29 \leq \delta_p \leq 0.31$  at 532 nm for the presumptive pure dust layers. Comparing SAMUM-2  $S_p$  values of Saharan dust of 48 – 63 sr at 355 nm and 54 – 70 sr at 532 nm with the mean values of  $(55 \pm 7)$  sr at 355 nm and  $(56 \pm 5)$  sr at 532 nm found during SAMUM-1 (Tesche et al., 2009a) a good agreement can be seen. These  $S_p$  values from measurements are considerably larger than those published by Ackermann (1998), which had been calculated using Mie theory (Mie, 1908) for spherical particles: He found  $S_p$  around 42 sr for 355nm and around 20 sr for 532nm. These discrepancies highlight that the non-sphericity of particles does not only influence the linear depolarization ratio but also the lidar ratio. Recently Wiegner et al. (2009) and Gasteiger et al. (2011) presented calculations of the optical parameters of Saharan dust considering the non-sphericity of the particles. Their results are closer to retrieved values from measurements, but significantly depend on the size distribution, on the particle shape, and on the real part of the refractive index of dust. The findings of SAMUM-2 will help to improve these calculations. Measurements of  $\delta_p$  of marine aerosols and biomass burning aerosols are rare. Murayama et al. (1999) measured the effect of dust and sea-salt particles in the atmospheric boundary layer and found mean values of  $0.01 \leq \delta_p \leq 0.10$  at 532 nm. They expected the large values to be connected to dry, crystalline

sea-salt particles, or a mixture of dry sea-salt and dust particles, whereas the lower values are attributed to pure liquid sea-salt particles. Sakai et al. (2000) measured  $\delta_p$  values at 532 nm of less than 0.05 in air masses influenced from the Pacific Ocean when the relative humidity was large, and  $\delta_p$  values larger than 0.1 at low relative humidity ( $\leq 50\%$ ). In a recent study Sakai et al. (2010) measured  $\delta_p$  at 532 nm for sea-salt and NaCl particles in a laboratory chamber and found mean  $\delta_p$  values of 0.01 for droplets, 0.08 for sea-salt crystals, and 0.21 for NaCl crystals. During SAMUM-2 wavelength independent  $\delta_p$  values between 355 nm and 532 nm of  $0.01 \leq \delta_p \leq 0.03$  were found at relative humidities above 50%, which indicates liquid marine aerosols. Mie theory based numerical studies of the lidar ratio  $S_p$  of marine aerosols (Ackermann, 1998) result in values between 19 sr and 27 sr at 355 nm and between 21 sr and 31 sr at 532 nm for relative humidities above 50%, at which marine aerosols are assumed to be liquid and spherical. The SAMUM-2 values of  $14 \text{ sr} \leq S_p \leq 24 \text{ sr}$  at 355 nm with a mean measurement error of  $\pm 4 \text{ sr}$  are a bit smaller but agree within the error bars with the theoretical values, while the SAMUM-2 values at 532 nm of  $17 \text{ sr} \leq S_p \leq 19 \text{ sr}$  ( $\pm 2 \text{ sr}$ ) are just below the theoretical results. For the mixture of biomass burning aerosols in the elevated layers values of  $0.12 \leq \delta_p \leq 0.23$  were found, wavelength independent for 355 nm, 532 nm and 710 nm. Heese and Wiegner (2008) reported about particle linear depolarization ratios  $\delta_p$  of  $0.1 \leq \delta_p \leq 0.15$  at 355 nm for a mixture of Saharan dust and biomass burning aerosols measured during the AMMA field campaign. These values are lower than the values found during SAMUM-2. For the AMMA data a high dust load within the mixed layer had been assumed, and hence a mean lidar ratio  $S_p$  for mineral dust of 55 sr had been used for the retrieval of  $\delta_p$ , most likely leading to the lower  $\delta_p$  values. However, Heese and Wiegner (2008) also show Raman measurements resulting in a mean lidar ratio  $S_p$  of  $(75 \pm 15) \text{ sr}$  at 355 nm within the mixed layer of dust and biomass burning aerosols. Amiridis et al. (2009) showed a wide range of  $S_p$  between 50 sr and 94 sr for biomass burning aerosols over Greece that originated from Russian forest fires. The SAMUM-2 results of 60 – 98 sr (mean value 76 sr) for 355 nm and 532 nm are in good agreement with those values. The high variability of the optical parameters of biomass burning aerosols from the measurements corresponds to the high variability of the particle composition found by Lieke et al. (2011). It can be assumed that the biomass burning aerosol is not homogeneous, but consists of a variety of different burning products and different amounts of dust from different sources.

## 5.2 Changes of optical properties of Saharan dust

Comparing the linear depolarization ratio  $\delta_p$  of Saharan dust at different states of transport, one can see a significant change in  $\delta_p$  at 355 nm between fresh and short-wave transported Saharan dust and dust long-range transported to Central Europe. However, at 532 nm  $\delta_p$  rather stays constant throughout the transport. The changes of the optical properties, especially at 355 nm, may be caused by alteration of the size distribution of the Saharan dust layer during transport. Wiegner et al. (2009) showed, that the spectral dependence of  $\delta_p$  is mainly dependent on the size distribution of the particles. Another reason may



be a lack of strongly hygroscopic sulfuric acid droplets (Kaaden et al., 2009) within this layer, compared to the findings during SAMUM-1 (Kandler et al., 2009). These droplets are in the size range of 200 - 400 nm (Kandler et al., 2009) and therewith most effective on the backscatter coefficient, and on the depolarization, at 355 nm. During their transport over humid areas, these droplets may have grown in size, and finally fallen out. As a consequence  $\delta_p$  at 355 nm increases while  $\delta_p$  at 532 nm (rather unaffected of small sulfuric acid droplets) stays constant. However, the cause of the alteration in  $\delta_p$  values at 355 nm is speculative, as no in-situ measurements were performed in the dust layers during the Saharan dust event over Central Europe.

The differences of the lidar ratio  $S_p$  of Saharan dust at different states of transport were within the uncertainty range. However, the mean values during SAMUM-2 are slightly higher, compared to SAMUM-1. Studies of backward trajectories and satellite images during SAMUM-1 and SAMUM-2 (Knippertz et al., 2009, 2011) found different source regions of the Saharan dust layers during both campaigns. During the first campaign the main source regions were located in western Tunisia and Mali, whereas the main source regions of the Saharan dust layers during the second campaign were located in the Bodele depression, as well as Mali and Niger. Kandler et al. (2011a) found an absence of calcium in the dust layers over Praia, and a higher iron content, compared to the dust layers during SAMUM-1. These differences may be attributed to the different source regions, or to changes during transport. The decrease of non-absorbing aerosols within the dust layer, together with the higher iron content, may lead to these slightly higher values (Gasteiger et al., 2011), as  $S_p$  is mainly influenced from the chemical composition of the aerosols (Wiegner et al., 2009).  $S_p$  values for long-range transported Saharan dust to Central Europe agree well with the values found during SAMUM-1 and SAMUM-2 within the error bars. Analysis of the chemical composition of the dust layers and their source region were not performed for this event.

### 5.3 Comparison of lidar derived AOD and SSARA measurements

For signal analysis following the Fernald/Klett algorithm (see Section 2.3.1) a lidar ratio  $S_p$  for the assumed type of aerosol has to be chosen, or taken from simultaneous Raman measurements. During the events presented in this work,  $S_p$  was adopted from night-time Raman measurements. Although the temporal stability of the atmosphere was verified, and so the application of the night-time derived  $S_p$  justified, differences in the vertical distribution and the low signal-to-noise ratio of the Raman measurements are potential error sources. The correctness of  $S_p$  used for the Fernald/Klett algorithm can be checked with the help of simultaneous sun-photometer measurements, by comparing the lidar and the sun-photometer derived (AOD).

As an example, the measurements of SAMUM-2 are shown in Figure 5.1. For this purpose, the total AOD at 355 nm was calculated from SSARA measurements at 340

nm using the Angström exponent between 340 nm and 500 nm. The missing values are either due to high cloudiness or the absence of day-time lidar measurements. For this comparison, sun-photometer measurements in middle of the time average of the lidar data, or the nearest value to the middle, were chosen. As the lowermost 100 m are missed by lidar measurements, a constant value of the extinction coefficient in this height range was assumed for the calculation of the AOD.

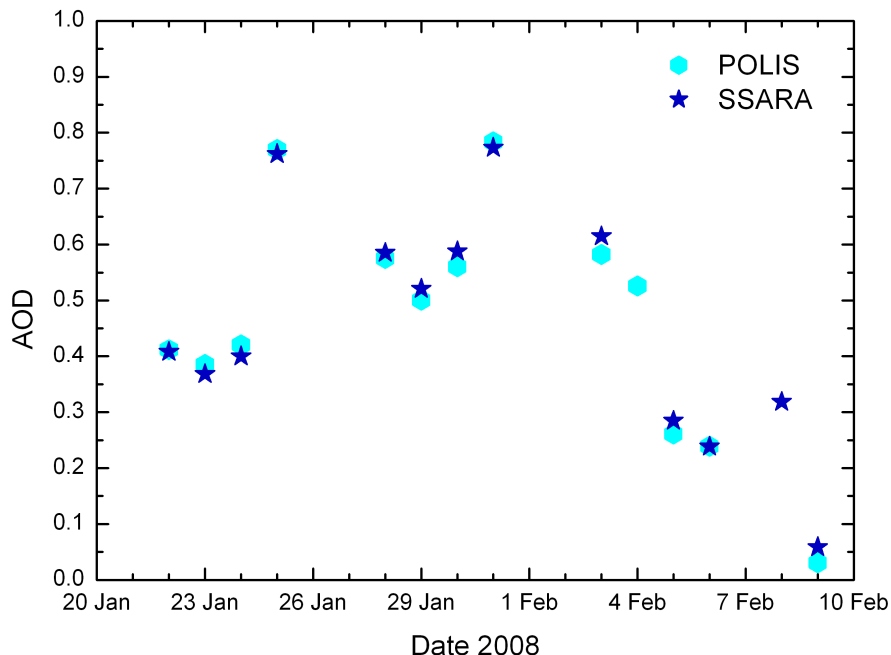


Figure 5.1: Aerosol optical depth at 355 nm derived from POLIS lidar measurements and SSARA sun-photometer measurements during the SAMUM-2 campaign.

As can be seen, the AOD derived from POLIS lidar and SSARA sun-photometer measurements agree well. However, small differences in both measurements are obvious. The slope of the linear regression over all measurements is 0.98 with an negative offset of the POLIS measurements of  $\approx 0.02$  (see Figure 5.2). One reason for these differences may result from uncertainties in the estimation of the AOD in the lowermost 100 m. Another explanation may be the different measurement directions of both instruments. Airborne measurements (Weinzierl et al., 2011) found that the aerosol distribution in the surrounding of the measurement site was strongly influenced from the island. As SSARA measures the direct solar radiances, it is looking in the direction of the sun, whereas for measurements with POLIS the direction of the sun is avoided to reduce the influence of solar radiation.

This example shows, that with the correct lidar ratio, and for instruments with an overlap close to the ground, the lidar derived AOD agrees well with co-located sun-photometer measurements. Raman measurements require contingent of man power, which is not affordable for a high spatial coverage of lidar measurements. Therefore the comparison of sun-photometer and lidar measurements can help to select the correct lidar ratio, e.g. in

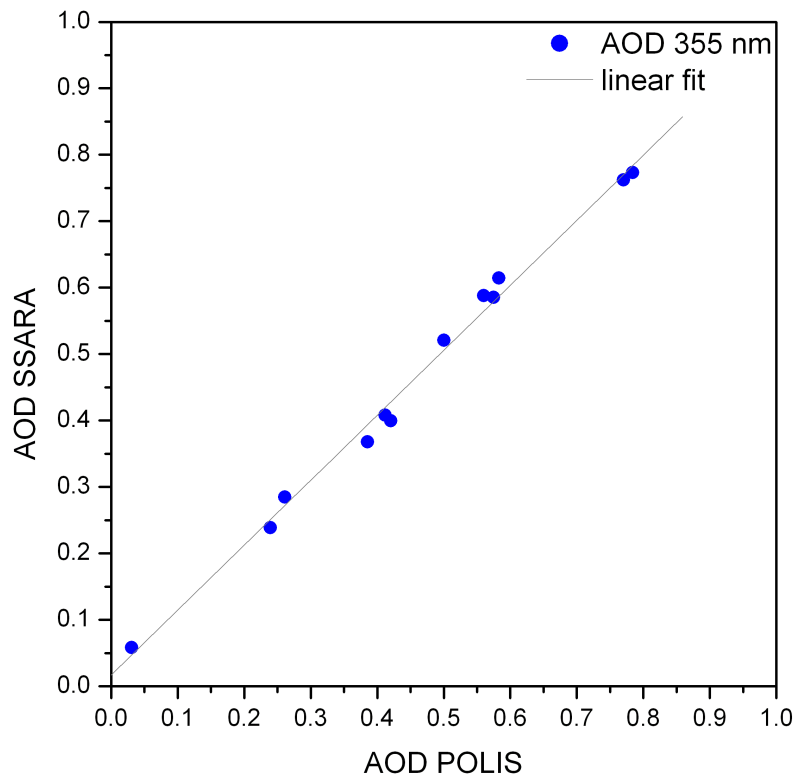


Figure 5.2: Aerosol optical depth (AOD) at 355 nm derived from SSARA measurements over AOD from POLIS measurements during the SAMUM-2 campaign.

cases of elastic backscatter lidars. However, this method should be handled with care if the overlap of the systems is not close to the ground, as the assumption of the AOD in the overlap region can lead to large errors. Another source of errors occurs if a multi-layer structure of more than one type of aerosol with different lidar ratios are present in the atmosphere. The scaling of the mean lidar ratio with sun-photometer measurements can lead to an overestimation of the AOD of one layer and underestimation of the AOD of another. In such cases, further information are required to get an estimation of the type of aerosol and the corresponding lidar ratio.

## 5.4 Strategy to discriminate different aerosol types

Intensive properties of aerosols are dependent on the type of aerosol and do not depend on its amount. Therefore, a certain value of the intensive parameter is associated to a certain type of aerosol. In the Chapter 4 it was shown, that the intensive parameters  $S_p$  and  $\delta_p$  are quite different for different types of aerosols, and additionally show a wavelength dependence for certain types. Therefore they are an appropriate tool to distinguish different types of aerosols. However, a classification based on optical properties, is only possible if

the sources of uncertainties are considered in an extensive error analysis (see Section 2.5) and the resulting errors are small. An reliable error analysis is thus as important as the measurement itself.

Table 5.1: Optical properties of different aerosols types presented in Chapter 4. The mean values are the averages of the layer mean values of all analysis during the period and the corresponding mean error, the range denotes the maximum and minimum mean values of all analyses. POLIS measurements at 355 nm

Date	$\delta_p$ <b>355 nm</b>	$\delta_p$ range	$S_p$ [sr] <b>355</b>	$S_p$ range [sr]	type
SAMUM-1	0.25±0.07	0.22 – 0.26	55±5	47 – 60	fresh dust
SAMUM-2	0.25±0.02	0.21 – 0.36	58±8	48 – 63	aged pure dust
Munich 2008	0.38±0.08	0.35 – 0.41	68±9	60 – 70	long-range transp. dust
SAMUM-2	0.16±0.03	0.12 – 0.20	76±12	60 – 102	biomass burning
SAMUM-2	0.02±0.01	0.01 – 0.02	18±3	14 – 27	marine aerosol
Munich 2010	0.36±0.02	0.30 – 0.38	56±4	50 – 60	volcanic ash

Table 5.2: Same as Tabel 5.1 but for MULIS measurements at 532 nm

Date	$\delta_p$ <b>532 nm</b>	$\delta_p$ range	$S_p$ [sr] <b>532</b>	$S_p$ range [sr]	type
SAMUM-1	0.31±0.01	0.29 – 0.31	56±5	47 – 62	fresh pure dust
SAMUM-2	0.30±0.01	0.29 – 0.31	61±5	56 – 66	aged pure dust
Munich 2008	0.34±0.02	0.31 – 0.36	59±8	53 – 69	long-range transp. dust
SAMUM-2	0.16±0.01	0.12 – 0.20	66±11	60 – 90	biomass burning
SAMUM-2	0.02±0.02	0.01 – 0.02	18±2	17 – 19	marine aerosol
Munich 2010	0.37±0.02	0.35 – 0.38	49±2	40 – 56	volcanic ash

Figures 5.3 and 5.4 display the corresponding mean lidar ratios  $S_p$  over the mean particle linear depolarization ratio  $\delta_p$  for POLIS measurements at 355 nm and for MULIS measurements at 532 nm, respectively. The measurement for this classification were performed during the field campaigns and aerosol events described above. The statistics of the underlying dataset can be found in Appendix A.

For the 355 nm measurement (see Table 5.4) values of  $0.24 \leq \delta_p \leq 0.26$  and  $48 \text{ sr} \leq S_p \leq 63 \text{ sr}$  were found for pure Saharan dust, and  $0.12 \leq \delta_p \leq 0.2$  and  $65 \text{ sr} \leq S_p \leq 102 \text{ sr}$  for the layer of biomass burning aerosols with dust contribution. In the marine boundary layer mean values of  $0.02 \leq \delta_p \leq 0.05$  and  $14 \text{ sr} \leq S_p \leq 28 \text{ sr}$  were found. For the transported Saharan dust  $\delta_p$  and  $S_p$  are found to be as high as  $0.3 \leq \delta_p \leq 0.45$  and  $50 \text{ sr} \leq S_p \leq 70 \text{ sr}$ , respectively, and for transported volcanic ash  $0.3 \leq \delta_p \leq 0.38$  and  $50 \leq S_p \leq 60 \text{ sr}$ , respectively. For 532 nm corresponding mean values (see Tabel 5.4) for transported but pure Saharan dust of  $0.29 \leq \delta_p \leq 0.31$  and  $54 \leq S_p \leq 66 \text{ sr}$  are found. The mean values

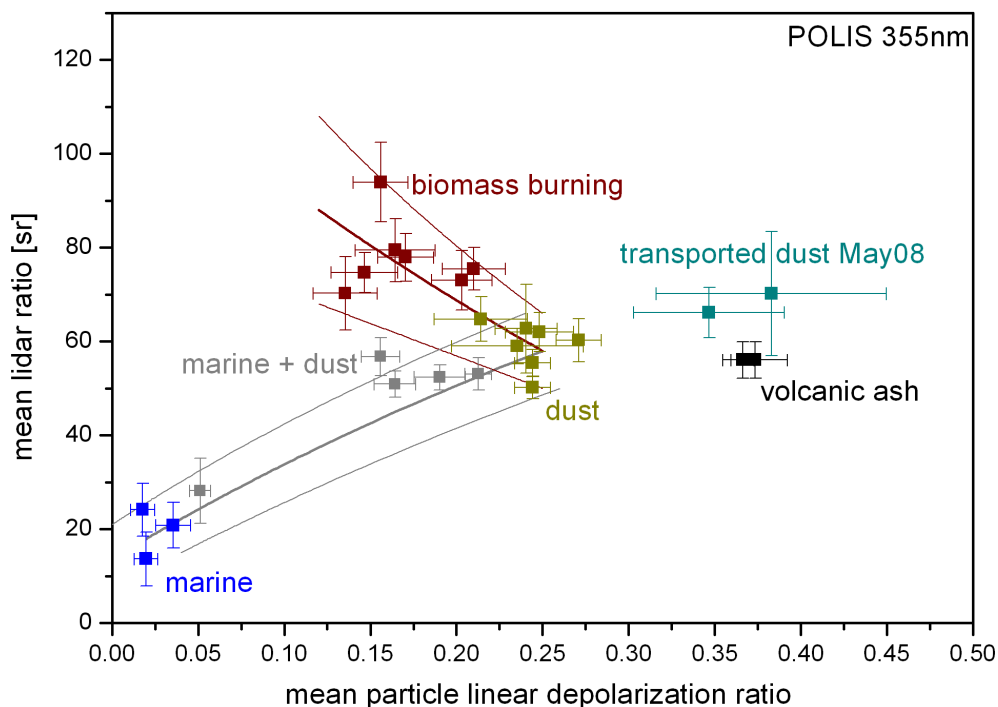


Figure 5.3: Layer-mean values of  $S_p$  plotted over layer-mean values of  $\delta_p$  at 355 nm. The corresponding measurements were performed with POLIS during both SAMUM campaigns in Morocco and Praia, as well as during aerosol events in Munich and Maisach. The dots are backscatter weighted mean values, the error bars show the layer-mean systematic errors. The thick gray and wine lines show calculated values of  $S_p$  over  $\delta_p$  for two-component aerosol mixtures. The thin gray and wine lines denote the uncertainty ranges.

allocated to biomass burning aerosols mixed with dust particles are  $0.12 \leq \delta_p \leq 0.2$  and  $61 \leq S_p \leq 90$  sr, and for marine aerosols in the boundary layer  $0.01 - 0.07$  for  $\delta_p$  and  $17 \text{ sr} \leq S_p \leq 19$  sr. The values found for long-range transported Saharan dust and volcanic particles over Central Europe are  $0.30 \leq \delta_p \leq 0.36$  and  $50 \text{ sr} \leq S_p \leq 68$  sr, and  $0.33 \leq \delta_p \leq 0.38$  and  $45 \text{ sr} \leq S_p \leq 50$  sr, respectively.

This classification shows, that in principle it is possible to discriminate certain types of aerosols, and mixtures of aerosols, on the basis of lidar measurements. Additionally some aerosols show a wavelength dependence of the optical properties. Thus the use of two or more wavelengths can improve the classification. For example, the discrimination of Saharan dust and volcanic aerosols at 532 nm is critical.  $S_p$ -values at 532 nm of Saharan dust retrieved during SAMUM-2 are quite similar to  $S_p$  of volcanic ash, furthermore  $\delta_p$  of Saharan dust is only slightly lower than  $\delta_p$  of volcanic ash. Considering the additional measurements of  $S_p$  and  $\delta_p$  at 355 nm the discrimination between both aerosol types can be improved, as  $\delta_p$  shows a wavelength dependence for Saharan dust, but is wavelength independent for volcanic ash. Impossible is the discrimination between long-range transported

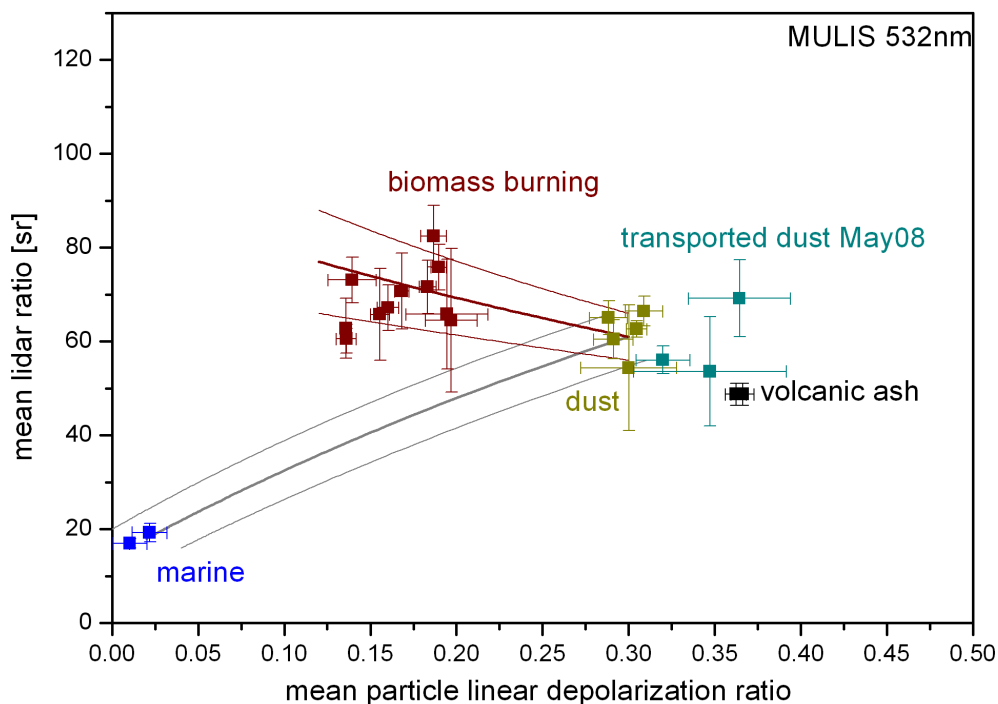


Figure 5.4: Same as Figure 5.3 but for MULIS measurements at 532 nm.

dust to Europe and volcanic ash based on the measurements presented in this work. Both aerosols show wavelength independent values of  $\delta_p$  and similar values of  $S_p$ , furthermore the uncertainties of the retrieved optical properties of the long-range transported Saharan dust are large. As a consequence additional information is needed to distinguish between these aerosol types.

## 5.5 Change of optical properties in aerosol mixtures

With accurate measurements and resulting small errors, it is not only possible to discriminate different types of aerosols and different mixtures, it is also possible to determine the contribution of the aerosol components to the total particle extinction coefficient  $\alpha_p$  of the particles, assuming a two-component mixture. As an example the relationship between  $S_p$  and  $\delta_p$ , respectively, and the fraction of the total extinction is shown for mixtures of Saharan dust and biomass burning aerosols, and Saharan dust and marine aerosols.

The lidar ratio of an aerosol ensemble is  $S_{p,ens} = \alpha_p/\beta_p$  (Gasteiger et al., 2011). Assuming a two component mixture and normalizing the total particle extinction coefficient to  $\alpha_p=1$ ,  $S_{p,ens}$  can be calculated from

$$S_{p,ens} = \frac{1}{\frac{1-x}{S_{p,1}} + \frac{x}{S_{p,2}}} \quad (5.1)$$

with  $x$  (with  $x = 0.0 \dots 1.0$ ) being the fraction of one aerosol type of the total particle extinction coefficient of the ensemble, and  $S_{p,1}$  and  $S_{p,2}$  the lidar ratios of the two considered aerosol components. For the calculation,  $S_p$ -values resulting from analyses of the SAMUM-2 dataset (see Chapter 4 and Section 5.4) were used. The relationship between  $S_p$  and the contribution of Saharan dust and biomass burning aerosols (red curve), and Saharan dust and marine aerosols (blue curve) to  $\alpha_p$ , was found to be clearly non-linear (see Figure 5.5). Over a large range of mixtures the lidar ratio starting from pure marine aerosols increases much slower than the contribution of Saharan dust to  $\alpha_p$ . E.g. an increase of half of the  $S_p$ -range from pure marine to pure dust aerosols is achieved with a dust fraction of  $\alpha_p$  of about 76%. For the mixture of biomass burning aerosols and dust a decrease of half the  $S_p$ -range is achieved with a dust fraction of  $\alpha_p$  of about 43%.

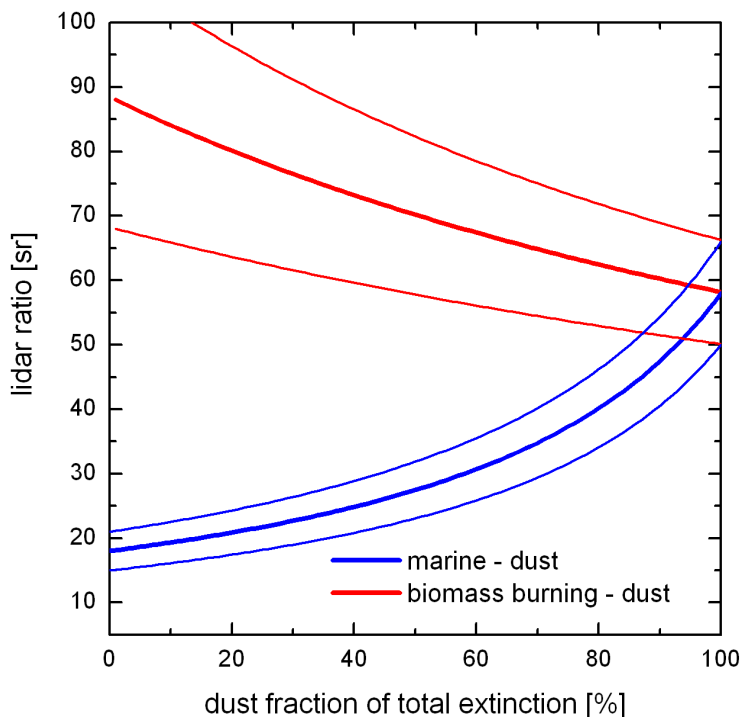


Figure 5.5: Relationship of the lidar ratio at 355 nm and the dust fraction of the total extinction coefficient in a two-component mixtures of mineral dust and biomass burning aerosols (red curve), and of mineral dust and marine aerosols (blue curve). The red thick line shows the mean fit between Saharan dust and biomass burning aerosols, the thick blue line between Saharan dust and marine aerosols. The thin lines show the fit of the retrieval considering the errors of the input parameters.

The linear depolarization ratio of a two component mixture can be calculated from

$$\delta_{p,ens} = \frac{\frac{1-x}{S_{p,1}} \frac{\delta_{p,1}}{1+\delta_{p,1}} + \frac{x}{S_{p,2}} \frac{\delta_{p,2}}{1+\delta_{p,2}}}{\frac{1-x}{S_{p,1}} \frac{1}{1+\delta_{p,1}} + \frac{x}{S_{p,2}} \frac{1}{1+\delta_{p,2}}} \quad (5.2)$$

with  $\delta_{p,1}$  and  $\delta_{p,2}$  the particle linear depolarization ratio of the pure aerosol components in the two-component mixture. For  $\delta_p$ -values of both contributing components again values resulting from SAMUM-2 (see Chapter 4 and Section 5.4) were used. The relationship between the contribution to the total extinction coefficient and  $\delta_p$  is again clearly non-linear (see Figure 5.6). For the marine-dust mixture half the  $\delta_p$ -range, starting from  $\delta_p$  of pure marine aerosols, is achieved with a dust fraction of  $\alpha_p$  of 79%. For the mixture of biomass burning aerosols and dust, the increase of  $\delta_p$  is faster than the increasing dust fraction, as half of the  $\delta_p$ -range is achieved with about 43% dust fraction of  $\alpha_p$ .

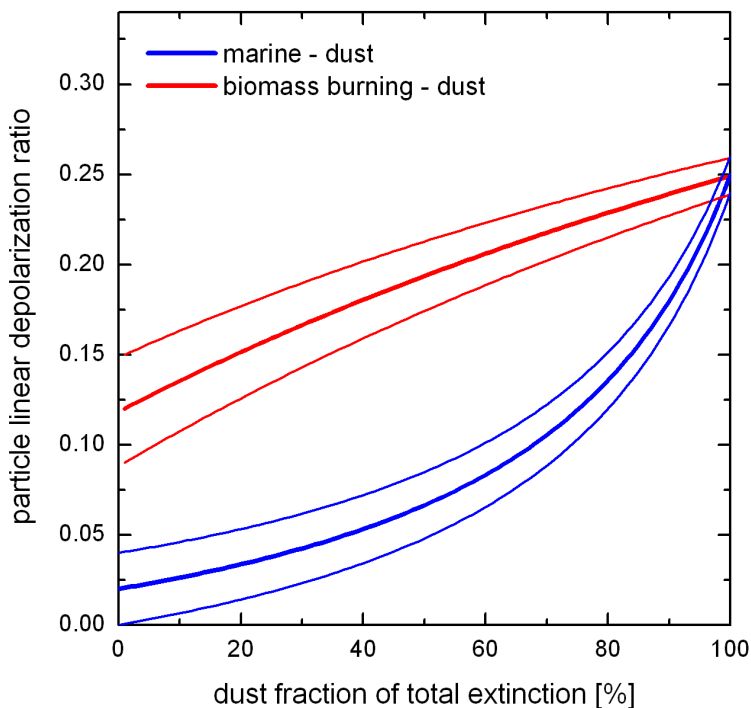


Figure 5.6: Same as Figure 5.6 but for the particle linear depolarization ratio at 355 nm.

The results of Equations 5.1 and 5.2 can be used as look-up tables to determine the contribution of the single aerosol types to the total extinction coefficient, when a two-component mixture is assumed, and to verify the assumed contributing aerosol types.



## 5.6 Determination of volume fraction

Assuming a two component aerosol mixture the optical properties of the contributing aerosol types (see Chapter 4) can be used to determine the volume fraction of the contributing aerosol types to the mixture. This approach is based on high quality measurements of  $\delta_p$ . In general, this methodology is based on the assumption of a two component mixture, of which one is spherical (subscript  $s$ ), the other one non-spherical (subscript  $ns$ ). In a first step, the profiles of the backscatter coefficient of both aerosol components are derived following a procedure described by Tesche et al. (2009b), relying on  $\delta_p$  of the two pure components from the aerosol characterization.

$$\beta_{ns} = \beta_p \frac{(\delta_p - \delta_s)(1 + \delta_{ns})}{(\delta_{ns} - \delta_s)(1 + \delta_p)} \quad (5.3)$$

$\delta_p$  in Equation 5.3 denotes the mean particle linear depolarization ratio of the mixture. The backscatter coefficient of the spherical particles can easily be calculated from  $\beta_s = \beta_p - \beta_{ns}$ .

In the next step, the profiles of the extinction coefficient are determined, using the corresponding lidar ratio of the pure components.

$$\alpha_{ns} = \beta_{ns} \cdot S_{ns} \quad (5.4)$$

$$\alpha_s = \beta_s \cdot S_s \quad (5.5)$$

From the extinction coefficient the volume concentration  $v_{ns}$  and  $v_s$  can be derived according to

$$v_{ns} = c_{ns} \cdot \alpha_{ns} \quad (5.6)$$

$$v_s = c_s \cdot \alpha_s \quad (5.7)$$

with  $c_{ns}$  and  $c_s$  being the conversion factors from extinction to volume concentration. This factor can be determined if the micro-physical properties of the type of aerosol is known, in particular the size distribution, the refractive index and the particle shape.

As an example, the detailed analysis of a marine-dust mixture in the planetary boundary layer (PBL) over Praia on 3 February, 2008, 17:30 - 19:30 UTC is shown. This analysis is based on POLIS measurements at 355 nm.  $\delta_p$  and  $S_p$  at 355 nm for the pure aerosol

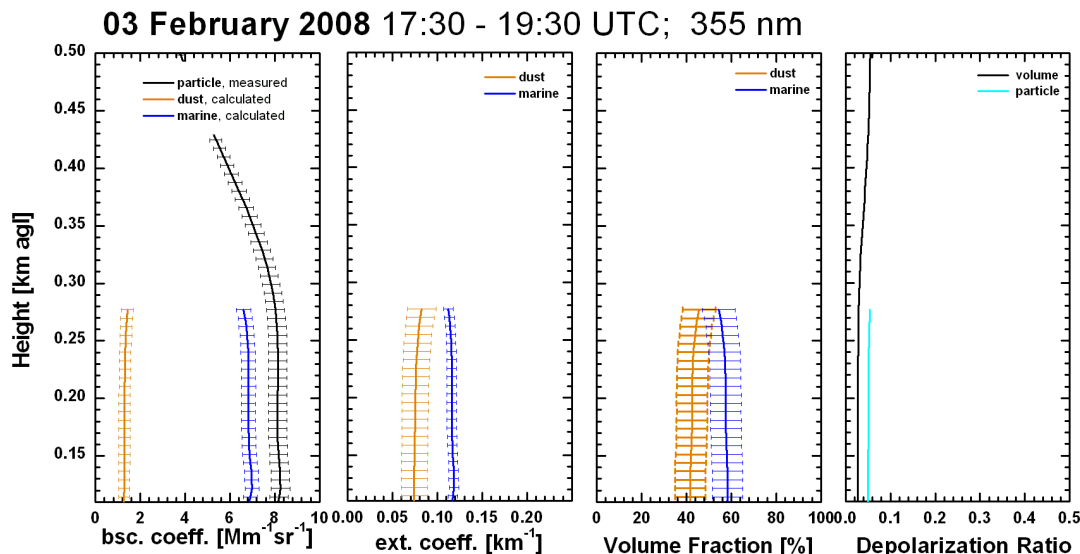


Figure 5.7: Dust (orange line), marine (blue line) and total backscatter coefficient (black line), dust and marine extinction coefficient, both at 355 nm, volume fraction of dust and marine aerosols, and measured volume and particle linear depolarization ratio on 03 February 2008 between 17:30 – 19:30 UTC.

type are 0.25 and 58 sr for dust, and 0.02 and 18 sr for marine aerosols (according to the aerosol characterization in Chapter 4), respectively. Conversion factors published by Hess et al. (1998) in the OPAC-database are used. However, their conversion factor for dust ( $0.905 \cdot 10^6$  m) is based on the assumption of spherical particles, which overestimates the true values, as it is known from scattering theory (Gasteiger et al., 2010). Thus the conversion factor for dust is reduced to  $0.7 \cdot 10^6$  m. For the marine component,  $0.615 \cdot 10^6$  m was used according to OPAC for marine aerosol at a relative humidity of 70%. The uncertainty of this method is estimated to 20 - 30 %.

The mean value of  $S_p$  in this layer is  $28 \pm 7$  sr and of  $\delta_p = 0.05 \pm 0.01$ . These values indicate a high contribution of spherical particles, probably wet sea salt. The profiles of the measured backscatter coefficient, and volume and particle linear depolarization ratio, the calculated backscatter and extinction coefficients of dust and marine aerosols, and the resulting volume fractions are shown in the four panels of Figure 5.7. With respect to the backscatter coefficient, dust contributes with roughly 20% to the total. The dust related extinction coefficient is  $0.075 \text{ km}^{-1}$ , compared to  $0.12 \text{ km}^{-1}$  of marine aerosols. The calculated dust and marine volume fractions in the PBL reveal a almost equal contribution of 42% dust and 58% marine aerosols.

Another method to derive the volume fraction of the marine and dust aerosols is from ground-based in-situ measurements, as it was done during SAMUM-2. In Schladitz et al. (2011a,b) the derivation of a “dry” dust volume fraction  $v_d^{dry}$  is described. Based on this

parameter, an “ambient” volume fraction  $v_d^{amb}$  is derived from numerical models using measured particle number size distribution, hygroscopic mixing state information, and hygroscopic growth factors. The temporal resolution of the retrieved data is three hours, thus somewhat lower than the remote sensing data; on the other hand they are continuously available. The relative uncertainty of the volume fractions is roughly estimated from the calculated volume concentrations to be 20%. As a conclusion,  $v_d^{amb}$  is representative for the mixing state under the actual atmospheric conditions and thus, directly comparable to the volume fractions retrieved from lidar data. The dry volume fraction  $v_d^{dry}$  might differ from  $v_d^{amb}$  in case of hygroscopic particles and high relative humidity.

Comparing the lidar derived values to the results from the in-situ sampling from 18:00 – 21:00 UTC, very good agreement with the ambient volume fraction of dust (39%) can be seen, but significant differences when the dry volume fraction, which is much higher (66%), is considered. This effect may be explained with the hygroscopicity of marine aerosols (e.g. Tang et al. 1997). From Wise et al. (2005) an increase of 60% of the volume equivalent radius of marine aerosols due to hygroscopic growth is estimated for the meteorological conditions of Praia during SAMUM-2, i.e., relative humidity in the range of 60 - 70% and transport of marine particles from the sea, where higher humidities are likely. In contrast, the Saharan dust particles are not hygroscopic.

To elaborate the implications of hygroscopic growth on aerosol mixtures of hydrophobic and hygroscopic components - in this case dust and marine aerosols - and to compare the available methodologies, the different time series of the analyses over the whole measurement period are shown in Figure 5.8. Shown are the dry and ambient volume fractions of dust derived from the ground-based in-situ measurements, the retrievals from the single particle analysis (Kandler et al., 2011a), and the volume fractions calculated from the lidar measurements. Note, that the lidar retrievals include twelve cases in total.

Three features are of special relevance. First, it is clearly visible, that at the beginning of February the aerosol regime changed from a dust-dominated mixture to a mixture with significant contribution of marine aerosols. Second, it is obvious that the dry volume fraction is always equal or greater than the ambient volume fraction (derived from the in-situ measurements). This is a consequence of the underlying physical concept that under conditions of high relative humidity a certain number of the non-dust component grows. The reduction of the volume fraction of dust during the second part of the experiment is much more pronounced than during the first part. This fact is consistent with the higher amount of marine aerosols. The third feature is the very good general agreement of the different retrievals. In this context it is noteworthy that the agreement of the retrieval based on the lidar measurements with the ambient volume fraction is much better than with the dry volume fraction, as expected with from the physical processes. For the same reason  $v_d$  from the single particle analysis better agrees with the dry volume fraction from the in-situ data.

Slight differences between  $v_d$  from the lidar retrieval and the ambient volume fraction (in-situ) are only observed when the contribution of dust was low, i.e.,  $v_d^{amb} \leq 30\%$  (5., 6. and 9. February). On these days in-situ measurements reveal a larger dust volume fraction than the lidar measurements. A possible reason for the discrepancy are the relative large

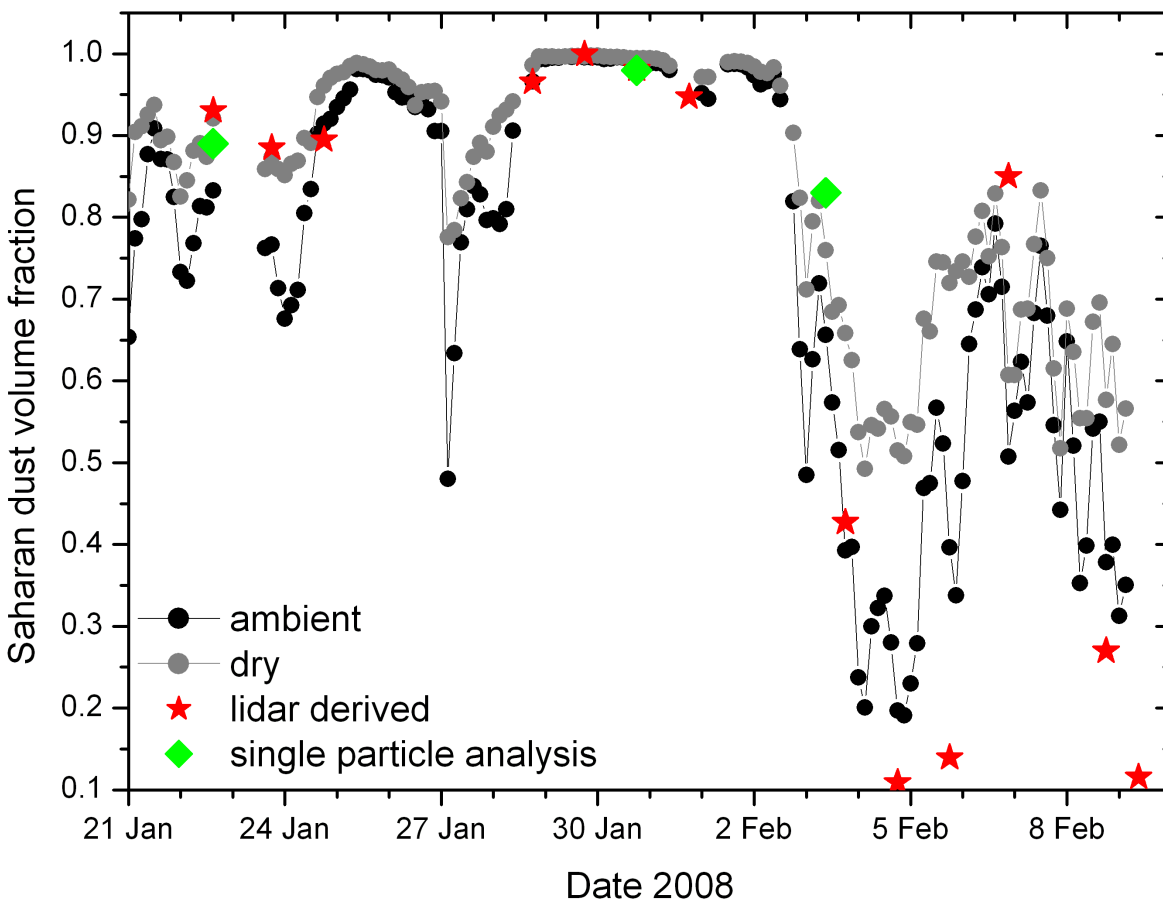


Figure 5.8: Volume fraction of Saharan dust in the PBL over Praia, Cape Verde, from 21 January – 09 February 2008. The black dots show the in-situ measurements under ambient relative humidity, the gray dots in-situ measurements of the dry volume fraction. The single particle analysis, as well as the lidar derived volume fractions are indicated by the green rectangles and red stars, respectively.

errors of the retrievals when  $v_d$  is low. Another reason is that the lowermost hundred meters cannot be observed by the lidars in spite of the low overlap of POLIS and the fact that MULIS measurements under low elevation angles were considered in the evaluation. Under conditions with a high marine component in the PBL this very shallow height range might become relevant: as the wind speed is high (Knippertz et al., 2011), the production of dust with large particles (radius larger than  $10 \mu m$ ) (Kandler et al., 2011b) from local sources might be enhanced and accumulate in this layer. As a consequence, a vertical gradient of aerosol properties builds up, leading to differences between the ground based aerosol samples and the atmospheric volume that is sensed by the lidar. This effect is in particular relevant on days with a low background concentration of Saharan dust as during

the last days of the campaign.

This methodology can be extended by the use of lidar depolarization ratios at two wavelengths. This extension might either increase the accuracy for the method applied on a two component aerosol mixture or make it even possible to apply the method on more complex mixtures. As the knowledge of mass fraction can be quite important (e.g. with respect to air quality and flight safety), the retrieval of volume fraction can be extended to a retrieval of mass fraction. This extension is easily feasible by multiplying with the mass density.

## 5.7 Hygroscopicity and depolarization

The characterization of the volcanic particles released from the Eyjafjallajökull was shown in Section 4.4. The most remarkable result of the studies of the ash plume is, that  $\delta_p$  shows a wavelength dependence with lower values at 355 nm under certain conditions. Comparisons with radiosondes launched at Oberschleißheim (22 km east of Maisach) lead to the assumption that  $\delta_p$  and the relative humidity may be correlated, and thus  $\delta_p$  may indicate the presence of hygroscopic particles. The spectral dependence of  $\delta_p$  might have the potential to extract some information on the size of the hygroscopic particles. For this purpose, some of the results are picked up again in this section.

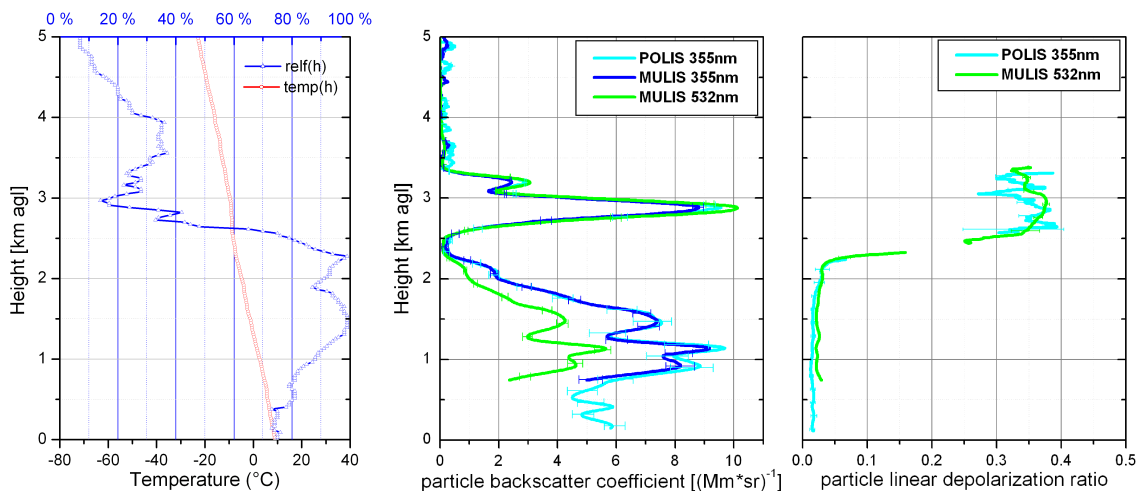


Figure 5.9: Profiles of relative humidity and temperature derived from radiosonde measurements at Oberschleißheim on 17 April 2010 at 0:00 UTC (left panel), and particle backscatter coefficient, and particle linear depolarization ratio at 355 nm and 532 nm (middle and right panel) for 17 April 2010 1:40 - 2:30 UTC derived from POLIS- and MULIS-measurements. The error bars indicate the systematic errors.

On 17 April, 1:40 - 2:40 UTC, the high values of  $\delta_p$ , wavelength independent between

$0.35 \leq \delta_p \leq 0.38$ , clearly indicate non-spherical particles. Ammonium sulfate particles, probably also present in the volcanic layer, would be dry (Kaaden et al., 2009) and thus also non-spherical, as the relative humidity within this layer is lower than 40 % (Figure 5.9). The relative humidity in the boundary layer is close to 100 %. This is consistent with the very low values of  $\delta_p$  between 0.01 and 0.02, which is a clear indication of liquid, spherical particles.

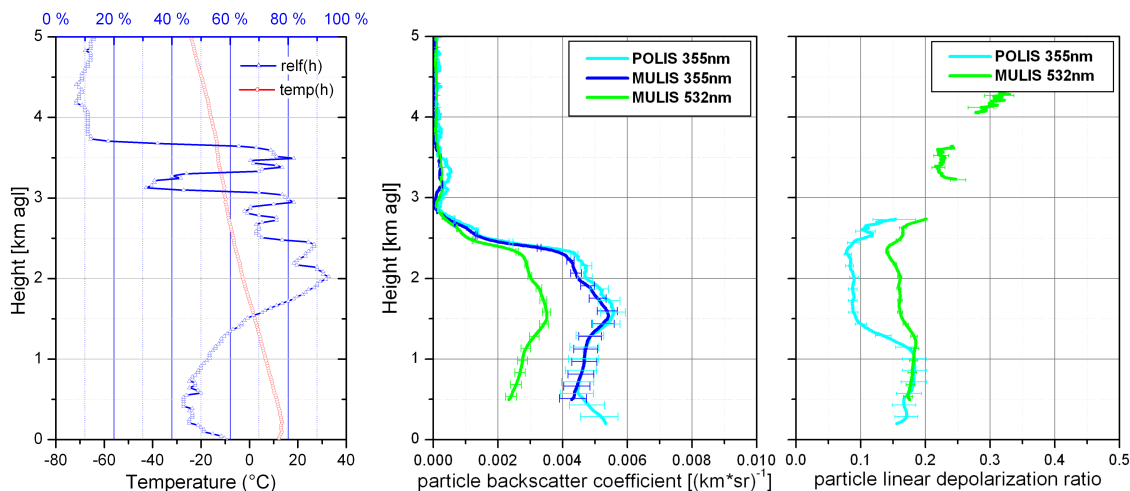


Figure 5.10: Profiles of relative humidity and temperature derived from radiosonde measurements at Oberschleißheim on 20 April 2010 at 0:00 UTC (left panel), and particle backscatter coefficient and particle linear depolarization ratio at 355 nm and 532 nm (middle and right panel) for 20 April 2010 1:00 - 2:50 UTC derived from POLIS- and MULIS-measurements. The error bars indicate the systematic errors.

On 20 April, 1:00 - 2:50 UTC,  $\delta_p$  between 0.5 - 1.2 km is wavelength independent with a mean value of  $0.18 \pm 0.02$ . Between 1.5 and 2.4 km the profiles of  $\delta_p$  at both wavelengths are clearly different with mean values of  $0.08 \pm 0.01$  at 355 nm and  $0.16 \pm 0.01$  at 532 nm. This change of  $\delta_p$  suggests a significant modification of the micro-physical properties of the particles. It is likely that the relative humidity is at least one of the reasons for this behavior. In the lower layer, the relative humidity is below 50%, whereas it is larger than 70% in the upper layer, i.e., heights above 1.5 km. Due to the higher relative humidity, it is assumed that the upper layer contains a larger number of spherical particles than the lower layer, and thus the depolarization ratio  $\delta_p$  decreases. This statement implies, that hygroscopic particles must be present. Whether they are sulfuric acid droplets, hygroscopic species attached to the ash particles or locally produced aerosols, must remain speculation as no in-situ chemical analyses are available. Nevertheless  $\delta_p$  retrieved from the lidar measurements rather suggests the presence of small hygroscopic particles, such as sulfuric acid particles, than large mineral- or glass particles with hygroscopic attachments. The fact that throughout both layers  $\delta_p$  is quite high is attributed to the presence of hydrophobic

non-spherical volcanic ash particles. Sulfuric acid droplets and ammonium sulfate droplets show hygroscopic growth when the relative humidity exceeds 70 - 75 % (Kaaften et al., 2009; Carrico et al., 2003).

It is remarkable that the decrease at 532 nm is only moderate, whereas the decrease at 355 nm is considerable. This may be explained with the assumption that the sulfuric acid droplets grow to sizes still small enough (Kandler et al., 2009) that primarily backscattering at 355 nm is enhanced but not at 532 nm. Then, the decrease of  $\delta_p$  would be stronger at the shorter wavelength. For relative humidities closer to 100% the size of the hygroscopic droplets might come to an order of magnitude where backscattering at 532 nm also increases and consequently  $\delta_p$  at 532 nm decreases as well. The slight decrease of  $\delta_p$  on 20 April, 2008 (01:00 - 02:50 UTC) at 532 toward the top of the upper layer, where the relative humidity reaches its maximum, might support this hypothesis.





# Chapter 6

## Conclusion

### Summary

Although the effort to improve the understanding of aerosols and their impact on global climate was huge in the last decades, there are still major gaps in our knowledge. Up to now, the knowledge about spatial and temporal distribution of individual aerosol types is limited. Further uncertainties are the optical properties of aerosols, mainly the linear particle depolarization ratio  $\delta_p$  and lidar ratio  $S_p$ . Especially the non-spherical shape and inhomogeneity of individual aerosol types make it difficult to simulate them in models and therewith to evaluate their optical properties.

In this work the optical properties of four major aerosol types of the atmosphere — Saharan dust, biomass burning, marine aerosols and volcanic ash — are investigated. Therefore about 600 hours of simultaneous measurements with the portable lidar system POLIS and the multi-wavelength lidar system MULIS were performed during the second field experiment of the SAMUM project (SAMUM-2) and during special meteorological events over Munich and Maisach. For SAMUM-2 additional informations of the Bertha system of the IFT were considered. In the scope of this work, improvements of the small lidar system POLIS were made with respect to detection range and depolarization measurements. With the performed changes it is possible to perform measurements from about 100 m above ground to the free troposphere. Furthermore the errors of the linear particle depolarization ratio could be significantly reduced.

For the characterization of the four aerosols types intensive parameters, in particular the particle linear depolarization ratio  $\delta_p$  and the lidar ratio  $S_p$ , are used.  $\delta_p$  was measured at three wavelengths (355 nm, 532 nm, and 710 nm) during SAMUM-2 and at two wavelengths (355 nm and 532 nm) during events over Munich/Maisach.  $S_p$  was measured at two wavelengths (355 nm and 532 nm). For a complete characterization, a comprehensive error calculation of the retrieved properties is almost as important as the measurements itself. An error calculation of the systematical errors, considering the input values, and of the statistical errors, due to signal noise, of  $S_p$  was developed. It was found that the estimation of the reference value of the backscatter ratio  $R$  at the reference height  $r_0$  is

the most critical factor in the determination of the lidar ratio. For  $\delta_p$  only the systematic errors are considered in the error calculation, as the statistical errors are assumed to be negligible. Uncertainties of the  $S_p$ , as well as errors of the depolarization calibration are the main error sources of  $\delta_p$ .

The modifications of the lidar systems and the resulting small errors of  $S_p$  and  $\delta_p$  allow for the first time to study the wavelength dependence of  $\delta_p$  of Saharan dust at three wavelengths during SAMUM-2. A significant wavelength dependence of  $\delta_p$  of Saharan dust was found, with mean values of  $\delta_p = 0.25 \pm 0.02$  at 355 nm,  $\delta_p = 0.30 \pm 0.01$  at 532 nm and  $\delta_p = 0.37 \pm 0.04$  at 710 nm. The corresponding  $S_p$  at 355 nm and 532 nm was found to be wavelength independent within the error bars. The mean values are  $S_p = 58$  sr  $\pm$  8 sr at 355 nm and  $S_p = 61$  sr  $\pm$  5 sr at 532 nm. Comparing these values with the results of SAMUM-1 of  $\delta_p = 0.25 \pm 0.07$  at 355 nm,  $\delta_p = 0.31 \pm 0.01$  at 532 nm and  $\delta_p = 0.27 \pm 0.09$  at 710 nm, and  $S_p = 55$  sr  $\pm$  5 sr at 355 nm and  $S_p = 56$  sr  $\pm$  5 sr at 532 nm no significant changes of the intensive parameters can be seen. However, considering mean values found in case of long-range transported dust, e.g. in the Saharan dust layer over Munich/Maisach of  $S_p = 68$  sr  $\pm$  9 sr at 355 nm and  $S_p = 59$  sr  $\pm$  8 sr at 532 nm, and  $\delta_p = 0.38 \pm 0.08$  at 355 nm and  $\delta_p = 0.34 \pm 0.02$  at 532 nm a significant change in  $\delta_p$  at 355 nm is obvious. In contrast the change at 532 nm is only of minor extend. These changes may result from changes of the size distribution of the dust particles or the absence of highly hygroscopic small particles, like sulfuric acid droplets, which were found in the dust layer during both SAMUM campaigns.

Besides Saharan dust, optical properties of biomass burning aerosols, marine aerosols and volcanic ash are presented. Mean values of  $S_p = 76$  sr  $\pm$  12 sr at 355 nm and  $S_p = 66$  sr  $\pm$  11 sr at 532 nm are found for biomass burning aerosols, of  $S_p = 18$  sr  $\pm$  3 sr at 355 nm and  $S_p = 18$  sr  $\pm$  2 sr at 532 nm for marine aerosols, and  $S_p = 56$  sr  $\pm$  5 sr at 355 nm and  $S_p = 49$  sr  $\pm$  2 sr at 532 nm for volcanic ash. The mean values of  $\delta_p$  are  $\delta_p = 0.16 \pm 0.03$  at 355 nm,  $\delta_p = 0.16 \pm 0.02$  at 532 nm and  $\delta_p = 0.16 \pm 0.04$  at 710 nm for biomass burning aerosols,  $\delta_p = 0.02 \pm 0.02$  at 355 nm and 532 nm for marine aerosols, and  $\delta_p = 0.36 \pm 0.02$  at 355 nm and  $\delta_p = 0.37 \pm 0.02$  at 532 nm for volcanic ash.

It is shown, that simultaneous measurements of  $\delta_p$  and  $S_p$  are important, as they provide the potential to distinguish between different types of aerosols. This is in particular valuable concerning satellite remote sensing, as it can be used as basis for the determination of the correct input values in inversion retrievals of the optical properties. Another application is the use for the investigation of aerosol climatologies based on lidar measurements. The results of this work may help to identify different aerosol types. Hence the knowledge about spatial and temporal distributions of individual aerosol types may be improved.

With a new approach, not only the different aerosol types can be determined from  $\delta_p$  and  $S_p$ , but also the changes of  $\delta_p$  and  $S_p$  in two-component aerosol mixtures, and therewith the contribution of the individual types to that mixture. Comparisons of the lidar retrieved contribution of dust to the volume concentration of a dust-marine mixture with independent in-situ measurements of the volume fraction showed good agreements and proved the applicability of this method. Converting the volume fraction of the aerosol

types into mass concentration can easily be feasible by multiplying with the mass density. Thus this method can be quite important with respect to air quality and flight safety.

### Open scientific questions

The analyses in this work showed the potential of lidar measurements. But several questions remain unanswered.

The changes of values and wavelength dependence of  $\delta_p$  of Saharan dust show the necessity of multi-wavelength lidar observations in aerosol research. However, the errors of the retrieved optical properties of the long-range transported Saharan dust are quite large and therefore the findings are still limited. Dust events over Central Europe are rare and the dust is mostly mixed with other types of aerosols. Further observations of transported dust to Central Europe are needed to improve our understanding. In this context it has to be mentioned that the transport time of dust to the Cape Verde Islands (SAMUM-2) is only two to three days shorter than the transport time to Munich/Maisach. This fact raises the question whether the transport path has a larger impact on changes of optical properties of Saharan dust than the transport time. Therefore additional measurements over Central Europe, as well as observations at the destination of the transported dust plumes over the Atlantic Ocean are urgently required.

Besides the characterization of the considered aerosols in this work, the knowledge of the optical properties of other aerosol particles and the changes of the optical properties during transport is limited. Furthermore the connection between the optical properties and their micro-physical properties and chemical composition has to be improved. A data base of multi-spectral measured optical properties of different aerosol types in combination with their micro-physical and chemical properties is needed. Therefore further coordinated remote sensing and in-situ measurements are required for different measurement situations. Long-term studies of the lidar derived optical properties may improve our knowledge about the temporal and spatial variability of different aerosol types. Coordinated measurements of research networks with advanced lidar systems may furthermore cast some light on the problem about changes of optical properties during transport.



# Appendix A

## Statistical information of calculated mean values

Although  $\delta_p$  and  $S_p$  are intensive parameters of the aerosols, low signal intensities lead to large uncertainties. To reduce these statistical uncertainties the layer mean values are weighted with the backscatter coefficient  $\beta_p$  (see A.1 and A.2).

$$\overline{S_p} = \int_{r_1}^{r_2} \frac{\beta_p S_p}{\int_{r_1}^{r_2} \beta_p dr} dr = \frac{\int_{r_1}^{r_2} \alpha_p dr}{\int_{r_1}^{r_2} \beta_p dr} \quad (\text{A.1})$$

$$\overline{\delta_p} = \int_{r_1}^{r_2} \frac{\beta_p \delta_p}{\int_{r_1}^{r_2} \beta_p dr} dr \quad (\text{A.2})$$

The statistical information of all mean values shown and discussed in this work are listed in the following.

Table A.1: Date and parameters of all MULIS measurements of the particle linear depolarization ratio at 532 nm during SAMUM-2. Elev. denotes the lidar pointing elevation angle from horizontal.

date	time		height		elev.	$\delta_p$				
	from	to	from	to		mean	error	stdev	max	min.
	UTC	UTC	km	km	( $^\circ$ )	532 nm				
22. Jan 2008	16:00	17:00	0.4	0.8	87	0.23	0.01	0.007	0.25	0.22
22. Jan 2008	16:00	17:00	1.0	1.3	87	0.19	0.01	0.008	0.20	0.16
22. Jan 2008	16:00	17:00	1.5	2.0	87	0.16	0.01	0.024	0.34	0.14
23. Jan 2008	17:45	18:45	0.4	0.8	87	0.19	0.01	0.004	0.21	0.18
23. Jan 2008	17:45	18:45	1.2	2.0	87	0.14	0.01	0.003	0.15	0.13
24. Jan 2008	20:00	22:30	0.3	0.7	87	0.25	0.01	0.007	0.27	0.22
24. Jan 2008	20:00	22:30	1.1	1.7	87	0.15	0.01	0.003	0.16	0.14
24. Jan 2008	20:00	22:30	2.2	2.9	87	0.12	0.01	0.006	0.14	0.11
25. Jan 2008	14:00	16:00	0.5	1.3	87	0.29	0.01	0.002	0.30	0.28
25. Jan 2008	14:00	16:00	1.5	2.5	87	0.14	0.01	0.011	0.18	0.12
26. Jan 2008	01:30	02:30	0.5	1.1	87	0.29	0.01	0.003	0.29	0.28
26. Jan 2008	01:30	02:30	1.5	2.8	87	0.14	0.01	0.005	0.16	0.13
28. Jan 2008	21:10	22:20	0.2	0.4	28	0.25	0.01	0.016	0.29	0.23
28. Jan 2008	21:10	22:20	0.4	1.2	28	0.31	0.01	0.014	0.34	0.29
29. Jan 2008	20:40	21:40	0.2	0.4	29	0.28	0.01	0.001	0.29	0.28
29. Jan 2008	20:40	21:40	0.5	0.8	87	0.30	0.01	0.002	0.31	0.30
30. Jan 2008	20:35	22:30	0.5	1.0	87	0.29	0.01	0.008	0.30	0.27
30. Jan 2008	20:35	22:30	1.5	2.5	87	0.16	0.01	0.006	0.17	0.14
31. Jan 2008	20:18	22:16	0.5	1.0	87	0.31	0.01	0.001	0.31	0.30
31. Jan 2008	20:18	22:16	1.5	4.0	87	0.14	0.01	0.010	0.17	0.10
3. Feb 2008	20:30	22:30	0.1	0.2	20	0.07	0.01	0.002	0.07	0.07
3. Feb 2008	20:30	22:30	0.5	1.0	87	0.29	0.01	0.003	0.30	0.29
3. Feb 2008	20:30	22:30	1.8	3.0	87	0.18	0.01	0.004	0.19	0.17
4. Feb 2008	20:00	22:30	0.2	0.4	20	0.01	0.02	0.001	0.02	0.01
4. Feb 2008	20:00	22:30	0.8	1.1	87	0.30	0.03	0.011	0.31	0.26
4. Feb 2008	20:00	22:30	1.5	2.8	87	0.19	0.02	0.005	0.21	0.18
4. Feb 2008	20:00	22:30	3.1	3.9	87	0.19	0.01	0.010	0.21	0.16
5. Feb 2008	20:45	21:15	0.1	0.3	20	0.02	0.02	0.001	0.02	0.03
5. Feb 2008	20:45	21:15	0.8	1.9	87	0.25	0.02	0.030	0.29	0.18
5. Feb 2008	20:45	21:15	2.8	4.5	87	0.18	0.01	0.007	0.21	0.17
6. Feb 2008	20:30	22:30	1.0	2.2	87	0.20	0.01	0.005	0.21	0.18
6. Feb 2008	20:30	22:30	3.0	4.5	87	0.17	0.01	0.006	0.18	0.16
8. Feb 2008	17:00	19:00	0.2	0.5	20	0.03	0.02	0.002	0.04	0.03
8. Feb 2008	17:00	19:00	1.0	1.3	87	0.18	0.02	0.008	0.20	0.17
8. Feb 2008	17:00	19:00	3.6	4.3	87	0.17	0.01	0.014	0.20	0.04
9. Feb 2008	09:14	09:20	0.1	0.6	20	0.2	0.01	0.001	0.02	0.01

Table A.2: Same as Tabel A.1 but for POLIS measurements at 355 nm.

date	time		height		elev.	$\delta_p$	error	stdev	max	min.
	from	to	from	to		mean				
	UTC	UTC	km	km	( $^\circ$ )	355 nm				
22. Jan 2008	16:00	17:00	0.1	0.7	80	0.19	0.02	0.003	0.20	0.18
22. Jan 2008	16:00	17:00	1.0	1.3	80	0.16	0.02	0.007	0.18	0.14
22. Jan 2008	16:00	17:00	1.3	2.0	80	0.16	0.04	0.010	0.18	0.13
23. Jan 2008	17:45	18:45	0.2	0.8	80	0.16	0.01	0.005	0.17	0.15
23. Jan 2008	17:45	18:45	1.2	2.0	80	0.14	0.02	0.007	0.15	0.12
24. Jan 2008	18:00	20:00	0.2	1.0	80	0.16	0.01	0.005	0.17	0.15
24. Jan 2008	18:00	20:00	1.1	1.7	80	0.15	0.03	0.008	0.18	0.14
24. Jan 2008	18:00	20:00	2.2	2.9	80	0.16	0.02	0.007	0.19	0.15
25. Jan 2008	14:00	16:00	0.2	0.5	78	0.21	0.01	0.002	0.22	0.21
25. Jan 2008	14:00	16:00	0.5	1.3	78	0.21	0.02	0.002	0.22	0.21
25. Jan 2008	14:00	16:00	1.5	2.5	78	0.15	0.01	0.004	0.17	0.14
26. Jan 2008	02:00	03:00	0.2	0.5	78.5	0.24	0.03	0.002	0.24	0.23
26. Jan 2008	02:00	03:00	0.6	1.1	78.5	0.26	0.04	0.003	0.26	0.25
26. Jan 2008	02:00	03:00	1.5	2.8	78.5	0.16	0.02	0.007	0.20	0.16
28. Jan 2008	18:30	19:30	0.1	0.4	78	0.21	0.01	0.005	0.22	0.20
28. Jan 2008	18:30	19:30	0.5	1.2	78	0.24	0.02	0.010	0.27	0.22
29. Jan 2008	18:00	20:00	0.1	0.4	79	0.24	0.01	0.005	0.26	0.23
29. Jan 2008	18:00	20:00	0.5	0.8	79	0.27	0.01	0.005	0.27	0.27
30. Jan 2008	18:00	20:00	0.1	0.4	79	0.22	0.01	0.005	0.24	0.21
30. Jan 2008	18:00	20:00	0.6	1.2	79	0.25	0.02	0.004	0.26	0.23
30. Jan 2008	18:00	20:00	1.6	2.5	79	0.17	0.02	0.010	0.23	0.16
31. Jan 2008	19:00	19:41	0.1	0.4	79	0.19	0.02	0.010	0.22	0.18
31. Jan 2008	19:00	19:41	0.5	1.0	79	0.24	0.03	0.002	0.24	0.23
31. Jan 2008	19:00	19:41	1.7	2.7	79	0.15	0.02	0.009	0.20	0.11
3. Feb 2008	17:30	19:30	0.1	0.4	80	0.05	0.01	0.001	0.05	0.05
3. Feb 2008	17:30	19:30	0.7	1.0	80	0.26	0.03	0.004	0.27	0.23
3. Feb 2008	17:30	19:30	1.8	3.0	80	0.18	0.03	0.008	0.21	0.15
4. Feb 2008	15:00	17:00	0.2	0.4	77	0.02	0.01	0.001	0.02	0.02
4. Feb 2008	15:00	17:00	0.8	1.1	77	0.26	0.04	0.009	0.27	0.22
4. Feb 2008	15:00	17:00	2.4	2.8	77	0.21	0.07	0.003	0.22	0.21
4. Feb 2008	15:00	17:00	3.1	4.0	77	0.21	0.02	0.032	0.25	0.13
5. Feb 2008	18:00	20:00	0.1	0.3	78	0.02	0.01	0.01	0.02	0.02
5. Feb 2008	18:00	20:00	0.8	1.9	78	0.24	0.06	0.013	0.29	0.21
5. Feb 2008	18:00	20:00	2.8	4.0	78	0.21	0.03	0.010	0.25	0.19
6. Feb 2008	19:00	19:50	1.5	2.0	78	0.24	0.05	0.006	0.25	0.23
6. Feb 2008	19:00	19:50	3.5	4.5	77	0.18	0.02	0.012	0.21	0.15
8. Feb 2008	18:00	20:00	0.2	0.5	79	0.03	0.01	0.001	0.04	0.03
8. Feb 2008	18:00	20:00	1.0	1.3	79	0.23	0.08	0.013	0.26	0.20
8. Feb 2008	18:00	20:00	3.6	4.3	79	0.20	0.02	0.008	0.22	0.18
9. Feb 2008	09:00	09:45	0.1	0.6	76	0.03	0.01	0.001	0.03	0.02

Table A.3: Same as Table A.1 but for Bertha measurements at 710 nm.

date	time		height		elev. (°)	$\delta_p$				
	from	to	from	to		mean	error	stdev	max	min.
	UTC	UTC	km	km		710 nm				
22. Jan 2008	20:05	22:31	0.4	0.8	90	0.27	0.03	0.009	0.28	0.26
22. Jan 2008	20:05	22:31	1.0	1.3	90	0.21	0.03	0.016	0.23	0.19
22. Jan 2008	20:05	22:31	1.3	2.0	90	0.16	0.03	0.013	0.19	0.14
23. Jan 2008	20:51	22:10	0.4	0.8	90	0.28	0.03	0.008	0.30	0.27
23. Jan 2008	20:51	22:10	1.2	1.9	90	0.20	0.03	0.004	0.21	0.19
28. Jan 2008			0.5	1.2	90	0.40	0.05	0.017	0.44	0.34
29. Jan 2008			0.4	1.0	90	0.36	0.04	0.017	0.38	0.34
30. Jan 2008	20:08	22:58	0.5	1.0	90	0.36	0.04	0.007	0.38	0.35
30. Jan 2008	20:08	22:58	1.5	2.5	90	0.18	0.03	0.018	0.21	0.14
31. Jan 2008	21:32	23:32	0.5	1.5	90	0.36	0.04	0.004	0.36	0.35
31. Jan 2008	21:32	23:32	1.5	4.0	90	0.14	0.02	0.017	0.19	0.11
4. Feb 2008	21:21	22:14	1.7	2.9	90	0.23	0.04	0.018	0.26	0.19
4. Feb 2008	21:21	22:14	3.0	3.9	90	0.23	0.04	0.016	0.26	0.19
5. Feb 2008	20:45	21:15	2.5	3.5	90	0.20	0.03	0.015	0.22	0.16
6. Feb 2008	20:49	22:35	3.5	4.0	90	0.15	0.03	0.032	0.19	0.05



Table A.4: Date and parameters of all MULIS measurements of the particle lidar ratio at 532 nm during SAMUM-2. Elev. denotes the lidar pointing elevation angle from horizontal.

date	time		height		elev. (°)	$S_p(532\text{nm})$				
	from UTC	to UTC	from km	to km		mean sr	error sr	stdev sr	max sr	min. sr
22. Jan 2008	20:20	22:30	1.0	1.3	87	82	7	3	87	71
22. Jan 2008	20:20	22:30	1.5	2.0	87	66	10	4	73	51
23. Jan 2008	20:51	22:11	0.4	0.8	87	63	6	3	71	60
23. Jan 2008	20:51	22:11	1.2	2.0	87	90	22	10	113	73
24. Jan 2008	20:07	22:37	1.1	1.7	87	71	10	5	80	56
24. Jan 2008	20:07	22:37	2.2	2.9	87	84	7	8	95	61
26. Jan 2008	01:30	02:30	0.5	1.1	87	65	4	1	68	62
26. Jan 2008	01:30	02:30	1.5	2.8	87	73	5	4	79	64
28. Jan 2008	22:44	21:17	0.4	1.2	28	66	3	5	75	46
29. Jan 2008	21:47	22:18	0.5	0.8	87	63	2	4	69	54
30. Jan 2008	20:35	22:59	0.5	1.0	87	60	4	4	68	51
30. Jan 2008	20:35	22:59	1.5	2.5	87	67	5	8	85	54
31. Jan 2008	20:18	22:16	1.5	4.0	87	61	3	7	77	53
4. Feb 2008	20:05	22:30	0.2	0.4	20	17	2	2	19	11
4. Feb 2008	20:05	22:30	0.8	1.1	87	54	13	5	65	28
4. Feb 2008	20:05	22:30	1.5	2.8	87	66	12	14	85	38
4. Feb 2008	20:05	22:30	3.1	3.9	87	76	5	12	119	62
5. Feb 2008	21:45	23:59	0.1	0.3	20	19	2	1	24	18
5. Feb 2008	21:45	23:45	0.8	1.9	87	81	19	6	103	57
5. Feb 2008	21:45	23:45	2.8	4.5	87	72	6	8	95	58
6. Feb 2008	20:30	22:30	1.0	2.2	87	64	15	4	72	51
6. Feb 2008	20:30	22:30	3.0	4.5	87	71	8	9	94	34

Table A.5: Same as Table A.4 but for MULIS measurements at 355 nm.

date	time		height		elev.	$S_p(355\text{nm})$				
	from	to	from	to		mean	error	stdev	max	min.
	UTC	UTC	km	km	( $^{\circ}$ )	sr	sr	sr	sr	sr
22. Jan 2008	20:20	22:30	1.0	1.3	87	82	7	3	86	75
22. Jan 2008	20:20	22:30	1.5	2.0	87	76	12	5	84	65
23. Jan 2008	20:51	22:11	0.4	0.8	87	70	8	4	80	63
23. Jan 2008	20:51	22:11	1.2	2.0	87	69	19	4	77	58
24. Jan 2008	20:07	22:37	1.1	1.7	87	81	13	2	86	73
24. Jan 2008	20:07	22:37	2.2	2.9	87	98	9	1	102	91
26. Jan 2008	01:30	02:30	0.5	1.1	87	82	7	1	84	79
26. Jan 2008	01:30	02:30	1.5	2.8	87	86	9	3	91	80
28. Jan 2008	22:44	21:17	0.4	1.2	87	61	9	6	69	45
29. Jan 2008	21:47	22:18	0.5	0.8	87	65	5	3	69	45
30. Jan 2008	20:35	22:59	0.5	1.0	87	64	6	2	68	59
30. Jan 2008	20:35	22:59	1.5	2.5	87	87	8	3	90	82
31. Jan 2008	20:18	22:16	1.5	4.0	87	73	5	3	79	63
4. Feb 2008	20:05	22:30	0.2	0.4	20	88	28	2	92	83
4. Feb 2008	20:05	22:30	0.8	1.1	87	15	1	1	16	12
4. Feb 2008	20:05	22:30	1.5	2.8	87	52	16	3	41	57
4. Feb 2008	20:05	22:30	3.1	3.9	87	75	15	9	56	87
5. Feb 2008	21:45	23:59	0.1	0.3	20	73	5	4	64	80
5. Feb 2008	21:45	23:45	0.8	1.9	87	19	2	1	24	17
5. Feb 2008	21:45	23:45	2.8	4.5	87	66	19	7	85	58
6. Feb 2008	20:30	22:30	1.0	2.2	87	70	6	4	84	61
6. Feb 2008	20:30	22:30	3.0	4.5	87	79	10	6	89	43

Table A.6: Same as Table A.4 but for POLIS measurements at 355 nm.

date	time		height		elev. (°)	$S_p(355\text{nm})$				
	from	to	from	to		mean	error	stdev	max	min.
	UTC	UTC	km	km		sr	sr	sr	sr	sr
22. Jan 2008	20:30	22:30	0.1	0.7	80	52	3	3	57	44
22. Jan 2008	20:30	22:30	1.0	1.3	80	79	7	3	85	71
22. Jan 2008	20:30	22:30	1.3	2.0	80	79	12	8	98	61
23. Jan 2008	20:40	22:40	0.2	0.8	80	57	4	1	60	54
23. Jan 2008	20:40	22:40	1.2	2.0	80	70	8	3	77	66
23. Jan 2008	20:40	22:40	0.2	1.0	80	82	25	8	111	64
24. Jan 2008	20:30	22:34	1.1	1.7	80	51	3	2	57	46
24. Jan 2008	20:30	22:34	2.2	2.9	80	67	9	6	81	43
24. Jan 2008	20:30	22:34	0.2	0.5	78	94	8	8	106	68
28. Jan 2008	20:30	22:30	0.1	0.4	78	53	3	5	56	46
28. Jan 2008	20:30	22:30	0.5	1.2	78	63	9	5	73	52
29. Jan 2008	20:50	22:30	0.1	0.4	79	55	3	1	57	53
29. Jan 2008	20:50	22:30	0.5	0.8	79	60	5	2	66	58
30. Jan 2008	20:45	22:15	0.3	0.5	79	50	2	1	51	47
30. Jan 2008	20:45	22:15	0.6	1.2	79	62	4	1	64	58
30. Jan 2008	20:45	22:15	1.6	2.5	79	78	5	1	81	75
31. Jan 2008	20:14	22:45	0.5	1.0	79	59	4	2	65	53
31. Jan 2008	20:14	22:45	1.7	2.7	79	75	4	7	88	61
3. Feb 2008	20:20	22:20	0.1	0.4	80	28	7	4	34	20
3. Feb 2008	20:20	22:20	1.8	3.0	80	72	20	5	86	64
4. Feb 2008	21:10	22:20	0.2	0.4	77	14	6	1	15	11
4. Feb 2008	21:10	22:20	0.8	1.1	77	48	12	7	61	34
4. Feb 2008	21:10	22:20	2.4	2.8	77	87	15	6	102	66
4. Feb 2008	21:10	22:20	3.1	4.0	77	75	5	6	93	60
5. Feb 2008	20:30	22:00	0.1	0.3	78	24	6	1	26	23
5. Feb 2008	20:30	22:00	0.8	1.9	78	58	11	5	75	51
5. Feb 2008	20:30	22:00	2.8	4.0	78	65	5	6	78	51
6. Feb 2008	20:20	22:35	3.5	4.5	77	102	15	27	284	76
8. Feb 2008	20:30	22:30	0.2	0.5	79	21	5	1	24	16
8. Feb 2008	20:30	22:30	1.0	1.3	79	42	1	7	60	27
8. Feb 2008	20:30	22:30	3.6	4.3	79	73	6	4	86	61

Table A.7: Same as Table A.1 but for measurements at Maisach/Munich.

date	time		height		elev. $S_p(532\text{nm})$	mean	error	stdev	max	min.
	from	to	from	to						
	UTC	UTC	km	km						
27 May 2008	21:30	22:30	1.5	4.5	85	69	8	5	90	52
28 May 2008	22:40	23:40	0.9	4.5	85	56	3	3	62	40
17 Apr 2010	01:30	02:40	2.6	3.5	85	49	2	3	56	40

Table A.8: Same as Table A.7 but for MULIS measurements at 355 nm.

date	time		height		elev. $S_p(355\text{nm})$	mean	error	stdev	max	min.
	from	to	from	to						
	UTC	UTC	km	km						
27 May 2008	21:30	22:30	1.2	4.9	85	70	13	3	86	62
17 Apr 2010	01:30	02:40	2.6	3.5	85	56	4	2	60	50

Table A.9: Same as Table A.7 but for POLIS measurements at 355 nm.

date	time		height		elev. $S_p(355\text{nm})$	mean	error	stdev	max	min.
	from	to	from	to						
	UTC	UTC	km	km						
28. May 2008	22:40	23:40	0.4	3.5	70	66	5	3	77	45

Table A.10: Date and parameters of all POLIS measurements of the particle linear depolarization ratio at 355 nm over Munich. Elev. denotes the lidar pointing elevation angle from horizontal.

date	time		height		elev.	$\delta_p$	error	stdev	max	min.
	from	to	from	to						
	UTC	UTC	km	km						
27 May 2008	19:00	20:30	3.0	5.0	70	0.38	0.07	0.02	0.46	0.35
28 May 2008	18:00	19:00	0.6	3.8	69	0.35	0.05	0.02	0.39	0.28
2 Jun 2008	00:55	02:55	2.0	5.5	76	0.40	0.15	0.02	0.47	0.37
17 Apr 2010	01:30	02:40	2.6	3.5	79	0.37	0.01	0.01	0.38	0.32
17 Apr 2010	06:30	07:40	1.9	2.5	79	0.37	0.01	0.01	0.41	0.36

Table A.11: Date and parameters of all MULIS measurements of the particle linear depolarization ratio at 532 nm over Munich. Elev. denotes the lidar pointing elevation angle from horizontal.

date	time		height		elev. (°)	$\delta_p$				
	from	to	from	to		mean	error	stdev	max	min.
	UTC	UTC	km	km		532 nm				
27 May 2008	20:30	22:30	0.7	5.3	85	0.36	0.03	0.01	0.38	0.36
28 May 2008	18:00	19:00	1.2	4.2	85	0.31	0.02	0.01	0.33	0.30
2 Jun 2008	00:00	01:30	2.2	5.5	85	0.34	0.04	0.01	0.37	0.32
17 Apr 2010	01:30	02:40	2.6	3.5	85	0.37	0.01	0.01	0.38	0.32
17 Apr 2010	06:30	07:40	1.9	2.5	85	0.36	0.01	0.01	0.37	0.36



# Appendix B

## List of abbreviations

Abbreviation	Definition
A/D	analog-to-digital
AERONET	Aerosol Robotic Network
AOD	Aerosol Optical Depth
APD	avalanche photo diode
Bertha	backscatter extinction lidar-ratio temperature humidity profiling apparatus
BS	Beam Splitter
CALIOP	Cloud-Aerosol Lidar with Orthogonal Polarization
CALIPSO	Cloud Aerosol Lidar and Infrared Pathfinder Satellite Observations
CH <sub>4</sub>	Methane
CO <sub>2</sub>	Carbon Dioxide
DBS	Dichroic Beam-Splitter
DFG	Deutsche Forschungsgemeinschaft / German Research Foundation
DLR	Deutsches Zentrum für Luft- und Raumfahrt / German Aerospace Center
DWD	Deutscher Wetterdienst / German Weather Service
EARLINET	European Aerosol Research Lidar Network
GDAS	Global Data Assimilation System
GOCART	Goddard Chemistry Aerosol Radiation and Transport Water
H <sub>2</sub> O	
HSRL	High Spectral Resolution Lidar
HWP	half wave plate
HYSPLIT	Hybrid Single particle Lagrangian Integrated Trajectory
IF	interference filter
IFT	Institut für Troposphärische Research, Leipzig
IPCC	International Panel on Climate Change

lidar	light detecting and ranging
LMU	Ludwig-Maximilians-Universität
MIM	Meteorological Institute of the LMU, Munich
MISR	Multangle Imaging SpectroRadiometer
MODIS	Moderate Resolution Imaging Spectroradiometer
MULIS	Multi-wavelength Lidar System
N <sub>2</sub>	Nitrogen
N <sub>s</sub> O	Nitrous oxid
NASA	National Aeronautics and Space Administration
Nd:YAG	Neodym-doped Yttrium-Aluminium-Granat (laser)
NOAA	National Oceanic and Atmospheric Administration
OPAC	Optical Properties of Aerosols and Clouds
PBC	Polarizing Beam-splitter Cube
PBL	Planetary Boundary Layer
PBS	see PBC
PMT	Photomultiplier Tube
POLIS	Portable Lidar System
READY	Real-time Environmental Applications and Display System
SAMUM	Saharan Mineral Dust Experiment
SAMUM-1	first SAMUM field campaign
SAMUM-2	second SAMUM field campaign
SSARA	Sun- and Sky- Automated Radiometer
SO <sub>2</sub>	sulfur dioxid
T	Transmission
Ti:Sa	Titanium-sapphire

---



# Bibliography

- Ackermann, J., “The extinction-to-backscatter ratio of tropospheric aerosol: A numerical study,” *Journal of Atmospheric and Oceanic Technology*, vol. 15, no. 4, pp. 1043–1050, 1998. [Online]. Available: <http://journals.ametsoc.org/doi/abs/10.1175/1520-0426%281998%29015%3C1043%3ATETBRO%3E2.0.CO%3B2>
- Albrecht, B. A., “Aerosols, Cloud Microphysics, and Fractional Cloudiness,” *Science*, vol. 245, no. 4923, pp. 1227–1230, 1989. [Online]. Available: <http://www.sciencemag.org/content/245/4923/1227.abstract>
- Amiridis, V., Balis, D. S., Giannakaki, E., Stohl, A., Kazadzis, S., Koukouli, M. E., and Zanis, P., “Optical characteristics of biomass burning aerosols over southeastern europe determined from uv-raman lidar measurements,” *Atmospheric Chemistry and Physics*, vol. 9, no. 7, pp. 2431–2440, 2009. [Online]. Available: <http://www.atmos-chem-phys.net/9/2431/2009/>
- Andreae, M. O., Rosenfeld, D., Artaxo, P., Costa, A. A., Frank, G. P., Longo, K. M., and Silva-Dias, M. A. F., “Smoking Rain Clouds over the Amazon,” *Science*, vol. 303, no. 5662, pp. 1337–1342, 2004. [Online]. Available: <http://www.sciencemag.org/content/303/5662/1337.abstract>
- Andreae, M., “Biomass burning - its history, use, and distribution and its impact on environmental quality and global climate.” *Cambridge, MA, MIT Press*, vol. A92-37626 15-42, pp. 3–21, 1991.
- Ansmann, A., Baars, H., Tesche, M., Müller, D., Althausen, D., Engelmann, R., Pauliquevis, T., and Artaxo, P., “Dust and smoke transport from africa to south america: Lidar profiling over cape verde and the amazon rainforest,” *Geophysical Research Letters*, vol. 36, p. L11802, 2009.
- Ansmann, A., Wandinger, U., Riebesell, M., Weitkamp, C., and Michaelis, W., “Independent measurement of extinction and backscatter profiles in cirrus clouds by using a combined raman elastic-backscatter lidar,” *Appl. Opt.*, vol. 31, no. 33, pp. 7113–7113, Nov 1992. [Online]. Available: <http://ao.osa.org/abstract.cfm?URI=ao-31-33-7113>

- Ansmann, A., Bösenberg, J., Chaikovsky, A., Comerón, A., Eckhardt, S., Eixmann, R., Freudenthaler, V., Ginoux, P., Komguem, L., Linné, H., Márquez, López, M.Ángel, Matthias, V., Mattis, I., Mitev, V., Müller, D., Music, S., Nickovic, S., Pelon, J., Sauvage, L., Sobolewsky, P., Srivastava, M. K., Stohl, A., Torres, O., Vaughan, G., Wandinger, U., and Wiegner, M., “Long-range transport of saharan dust to northern europe: The 11–16 october 2001 outbreak observed with earlinet.” *Journal of Geophysical Research*, vol. 108, p. 15, 2003.
- Behrendt, A. and Nakamura, T., “Calculation of the calibration constant of polarization lidar and its dependency on atmospheric temperature,” *Opt. Express*, vol. 10, no. 16, pp. 805–817, Aug 2002. [Online]. Available: <http://www.opticsexpress.org/abstract.cfm?URI=oe-10-16-805>
- Biele, J., Beyerle, G., and Baumgarten, G., “Polarization lidar: Correction of instrumental effects,” *Opt. Express*, vol. 7, no. 12, pp. 427–435, Dec 2000. [Online]. Available: <http://www.opticsexpress.org/abstract.cfm?URI=oe-7-12-427>
- Bierwirth, E., Wendisch, M., Ehrlich, A., Heese, B., Tesche, M., Althausen, D., Schladitz, A., Müller, D., Otto, S., Trautmann, T., Dinter, T., Von Hoyningen-Hüne, W., and Kahn, R., “Spectral surface albedo over morocco and its impact on radiative forcing of saharan dust,” vol. 61, p. 252–269, 2009, tellus B.
- Blanchard, D. C. and Syzdek, L. D., “Water-to-Air Transfer and Enrichment of Bacteria in Drops from Bursting Bubbles,” *Appl. Environ. Microbiol.*, vol. 43, no. 5, pp. 1001–1005, 1982. [Online]. Available: <http://aem.asm.org/cgi/content/abstract/43/5/1001>
- Boesenberg, J., “Earlinet : a european aerosol research lidar network to establish an aerosol climatology.” *Max-Planck-Institut fuer Meteorologie, Hamburg*, vol. Report 248, 2003.
- Bureau, R., *La Meteorologie*, vol. 292, 1946.
- Cakmur, R. V., Miller, R. L., Perlwitz, J., Geogdzhayev, I. V., Ginoux, P., Koch, D., Kohfeld, K. E., Tegen, I., and Zender, C. S., “Constraining the magnitude of the global dust cycle by minimizing the difference between a model and observations.” *Journal of Geophysical Research*, vol. 111, 2006.
- Carrico, C. M., Kus, P., Rood, M. J., Quinn, P. K., and Bates, T. S., “Mixtures of pollution, dust, sea salt, and volcanic aerosol during ace-asia: Radiative properties as a function of relative humidity.” *Journal of Geophysical Research*, vol. 108, pp. D23, 8650, 2003.
- Casadevall, T. J., “The 1989-1990 eruption of redoubt volcano, alaska: impacts on aircraft operations,” *Journal of Volcanology and Geothermal Research*, vol. 62, no. 1-4, pp. 301 – 316, 1994. [Online]. Available: <http://www.sciencedirect.com/science/article/B6VCS-48B59RS-3F/2/6ff73db20230c40f1a11c2d8d67b826f>

- Chen, W.-N., Tsai, F.-J., Chou, C. C.-K., Chang, S.-Y., Chen, Y.-W., and Chen, J.-P., “Optical properties of asian dusts in the free atmosphere measured by raman lidar at taipei, taiwan,” *Atmospheric Environment*, vol. 41, no. 36, pp. 7698 – 7714, 2007. [Online]. Available: <http://www.sciencedirect.com/science/article/B6VH3-4P1G9T5-1/2/40d5923b97830bdde99a57092c2dd2c7>
- Chin, M., Ginoux, P., Kinne, S., Holben, B. N., Duncan, B. N., Martin, R. V., Logan, J. A., Higurashi, A., and Nakajima, T., “Tropospheric aerosol optical thickness from the gocart model and comparisons with satellite and sunphotometer measurements.” *Journal of Atmospheric Science*, vol. 59, pp. 461–483, 2002.
- Erickson, I., D. J. and Duce, R. A., “On the global flux of atmospheric sea salt.” *Journal of Geophysical Research*, vol. 93, pp. 14,079–14,088, 1988.
- Esselborn, M., Wirth, M., Fix, A., Weinzierl, B., Rasp, K., Tesche, M., and Petzold, A., “Spatial distribution and optical properties of saharan dust observed by airborne high spectral resolution lidar during samum 2006,” *Tellus B*, vol. 61, p. 131–143, 2009.
- Evan, A. T., Dunion, J., Foley, J. A., Heidinger, A. K., and Velden, C. S., “New evidence for a relationship between atlantic tropical cyclone activity and african dust outbreaks.” *Geophysical Research Letters*, vol. 33, p. L19813, 2006.
- Feingold, G., Cotton, W. R., Kreidenweis, S. M., and Davis, J. T., “The impact of giant cloud condensation nuclei on drizzle formation in stratocumulus: Implications for cloud radiative properties,” *Journal of the Atmospheric Sciences*, vol. 56, no. 24, pp. 4100–4117, 1999. [Online]. Available: <http://journals.ametsoc.org/doi/abs/10.1175/1520-0469%281999%29056%3C4100%3ATIOGCC%3E2.0.CO%3B2>
- Fernald, F. G., “Analysis of atmospheric lidar observations: some comments.” *Applied Optics*, vol. 23, pp. 652–653, 1984.
- Freudenthaler, V., Esselborn, M., Wiegner, M., Heese, B., Tesche, M., Ansmann, A., Müller, D., Althaus, D., Wirth, M., Fix, A., Ehret, G., Knippertz, P., Toledano, C., Gasteiger, J., Garhammer, M., and Seefeldner, M., “Depolarization ratio profiling at several wavelengths in pure saharan dust during samum 2006.” *Tellus B*, vol. 61, p. 165–179, 2009.
- Freudenthaler, V., “Lidarmessungen der räumlichen ausbreitung sowie mikrophysikalischer und optischer parameter von flugzeugkondensstreifen,” 2000. [Online]. Available: <http://worldcat.org/oclc/76121606>
- Gasteiger, J., Groß, S., Freudenthaler, V., and Wiegner, M., “Volcanic ash from iceland over munich: mass concentration retrieved from ground-based remote sensing measurements,” *Atmospheric Chemistry and Physics*, vol. 11, no. 5, pp. 2209–2223, 2011. [Online]. Available: <http://www.atmos-chem-phys.net/11/2209/2011/>

- Gasteiger, J., Wiegner, M., Groß, S., Freudenthaler, C., V. Toledano, Tesche, M., and Kandler, K., "Modeling lidar-relevant optical properties of complex mineral dust aerosols," 2011, tellus B - accepted.
- Goudie, A. and Middleton, N., "Saharan dust storms: nature and consequences." *Earth-Science Reviews*, vol. 56, p. 179–204, 2001.
- Hansen, J., Sato, M., and Ruedy, R., "Radiative forcing and climate response." *Journal of Geophysical Research*, vol. 102, pp. 6831–6864, 1997.
- Haywood, J. and Boucher, O., "Estimates of the direct and indirect radiative forcing due to tropospheric aerosols: a review." *Rev. of Geophysics*, vol. 38, pp. 513–543, 2000.
- Heese, B. and Wiegner, M., "Vertical aerosol profiles from raman polarization lidar observations during the dry season amma field campaign," *Journal of Geophysical Research*, vol. 113, p. D00C1, 2008.
- Hess, M., Köpke, P., and Schult, I., "Optical properties of aerosols and clouds: The software package opac." *Bulletin of American Meteorological Society*, 1998.
- Hobbs, P. V. J. P. T., Hegg, D. A., Radke, L. F., and Eltgroth, M. W., "Particles and gases in the emissions from the 1980–1981 volcanic eruptions of mt. st. helens," *Journal of Geophysical Research*, vol. 87, pp. 11,062–11,086, 1982.
- Holben, B., Eck, T., Slutsker, I., Tanré, D., Buis, J., Setzer, A., Vermote, E., Reagan, J., Kaufman, Y., Nakajima, T., Lavenu, F., Jankowiak, I., and Smirnov, A., "Aeronet—a federated instrument network and data archive for aerosol characterization," *Remote Sensing of Environment*, vol. 66, no. 1, pp. 1 – 16, 1998. [Online]. Available: <http://www.sciencedirect.com/science/article/B6V6V-3V7SF8D-1D/2/7452854b09ed6f6d885f0aa14ac67ed6>
- Holben, B., Tanre, D., Smirnov, A., Eck, T. F., Slutsker, I., Abuhassan, N., Newcomb, W. W., Schafer, J. S., Chatenet, B., Lavenu, F., Kaufman, Y. J., Vande Castle, J., Setzer, A., Markham, B., Clark, D., Frouin, R., Halthore, R., Karneli, A., O'Neill, N. T., Pietras, C., Pinker, R. T., Vos, K., and Zibordi, G., "An emerging ground-based aerosol climatology: Aerosol optical depth from aeronet," *Journal of Geophysical Research*, vol. 106, pp. 12,067–12,097, 2001.
- IPCC, "climate change 2007: The scientific basis." *Cambridge University Press*, 2007.
- Iwasaka, Y., Shibata, T., Nagatani, T., Shi, G., Kim, Y. S., Matsuki, A., Trochkin, D., Zhang, D., Yamada, M., Nagatani, M., Nakata, H., Shen, Z., Li, G., Chen, B., and Kawahira, K., "Large depolarization ratio of free tropospheric aerosols over the taklamakan desert revealed by lidar measurements: possible diffusion and transport of dust particles," *Journal of Geophysical Research*, vol. 108, 2003.

- Jacobson, M. Z., “Global direct radiative forcing due to multicomponent anthropogenic and natural aerosols.” *JOURNAL OF GEOPHYSICAL RESEARCH*, vol. 106, pp. 1551–1568, 2001.
- , “The short-term cooling but long-term global warming due to biomass burning,” *Journal of Climate*, vol. 17, no. 15, pp. 2909–2926, 2004. [Online]. Available: <http://journals.ametsoc.org/doi/abs/10.1175/1520-0442%282004%29017%3C2909%3ATSCBLG%3E2.0.CO%3B2>
- Kaaden, N., Massling, A., Schladitz, A., Müller, T., Kandler, K., Schütz, L., Weinzierl, B., Petzold, A., Tesche, M., Leinert, S., Deutscher, C., Ebert, M., Weinbruch, S., and Wiedensohler, A., “State of mixing, shape factor, number size distribution, and hygroscopic growth of the saharan anthropogenic and mineral dust aerosol at tinfou, morocco,” vol. 61, p. 51–63, 2009, *tellus B*.
- Kandler, K., Schütz, L., Deutscher, C., Ebert, M., Hofmann, H., Jäckel, S., Jaenicke, R., Knipperts, P., Lieke, K., Massling, A., Petzold, A., Schladitz, A., Weinzierl, B., Wiedensohler, A., Zorn, S., and Weinbruch, S., “Size distribution, mass concentration, chemical and mineralogical composition and derived optical parameters of the boundary layer aerosol at tinfou, morocco, during samum 2006,” vol. 61, p. 32–50, 2009, *tellus B*.
- Kandler, K., Lieke, K., Benker, N., Küpper, M., Emmel, C., Müller-Ebert, D., Ebert, M., Schladitz, A., Schütz, L., and Weinbruch, S., “Ground-based off-line aerosol measurements at praia, cape verde, during the saharan mineral dust experiment campaign – part 2: Electron-microscopical individual particle analysis,” 2011, *tellus B* - accepted.
- Kandler, K., Schütz, L., Jäckel, S., Lieke, K., Emmel, C., Müller-Ebert, D., Ebert, M., Scheuvs, D., Schladitz, A., Wiedensohler, A., and Weinbruch, S., “Ground-based off-line aerosol measurements 1 at praia, cape verde, during the saharan mineral dust experiment campaign – part 1: Microphysical and mineralogical properties,” 2011, *tellus B* - accepted.
- Klett, J. D., “Stable analytical inversion solution for processing lidar returns,” *Appl. Opt.*, vol. 20, no. 2, pp. 211–220, Jan 1981. [Online]. Available: <http://ao.osa.org/abstract.cfm?URI=ao-20-2-211>
- , “Lidar inversion with variable backscatter/extinction ratios,” *Appl. Opt.*, vol. 24, no. 11, pp. 1638–1643, Jun 1985. [Online]. Available: <http://ao.osa.org/abstract.cfm?URI=ao-24-11-1638>
- Knippertz, P., Ansmann, A., Althausen, D., Mueller, D., Tesche, M., Bierwirth, E., Dinter, T., Müller, T., Hoyningen-Huene, W.von, Schepanski, K., Wendisch, M., Heinold, B., Kandler, K., Petzold, A., Schütz, L., and Tegen, I., “Dust mobilization and transport in the northern sahara during samum 2006 - a meteorological overview.” *Tellus B*, vol. 61, pp. 12–31, 2009.

- Knippertz, P., Tesche, M., Heinold, B., Kandler, K., Toledano, C., and Esselborn, M., “Dust mobilization and transport from west africa to cape verde—a meteorological overview of samum-2,” 2011, *tellus B* - accepted.
- Koren, I., Kaufman, Y. J., Washington, R., Todd, M. C., Rudich, Y., Vanderlei Martins, J., and Rosenfeld, D., “The bodélé depression: a single spot in the sahara that provides most of the mineral dust to the amazon forest.” *Environmental Research Letters*, vol. 1, pp. 014005+, 2006.
- Latham, J. and Smith, M. H., “Effect on global warming of wind-dependent aerosol generation at the ocean surface.” *Nature*, vol. 347, pp. 372–373, 1990.
- Levine, J. S., III, W. R. C., Donald R. Cahoon, J., Winsted, E. L., and Stocks, B. J., “Biomass burning and global change,” *AIP Conference Proceedings*, vol. 277, no. 1, pp. 131–139, 1992. [Online]. Available: <http://link.aip.org/link/?APC/277/131/1>
- Lieke, K., Kandler, K., Emmel, C., Petzold, A., Weinzierl, B., Scheuvs, D., Ebert, M., Weinbruch, S., and Schütz, L., “Particle chemical properties in the vertical column based on aircraft observations in the vicinity of cape verde,” 2011, *tellus B* - accepted.
- Liu, Z., Omar, A., Vaughan, M., Hair, J., Kittaka, C., Hu, Y., Powell, K., Treppe, C., Winker, D., Hostetler, C., Ferrare, R., and Pierce, R., “Calipso lidar observations of the optical properties of saharan dust: A case study of long-range transport,” *Journal of Geophysical Research*, vol. 113, pp. D07207+, 2008.
- Liu, Z., Omar, A., and al., M. V.et, “Calipso lidar observations of the optical properties of saharan dust: A case study of long-range transport,” *Journal of Geophysical Research*, vol. 113, p. D07207, 2008.
- Mahowald, N., Rivera, G. D., and Luo, C., “Comment on ‘relative importance of climate and land use in determining present and future global soil dust emission’,” *Geophysical Research Letters*, vol. 31, p. L24105, 2004.
- Mahowald, N., Baker, A., Bergametti, G., Brooks, N., Duce, R., Jickells, T., Kubilay, N., Prospero, J., and Tegen, I., “Atmospheric global dust cycle and iron inputs to the ocean.” *Global Biogeochemical Cycles*, vol. 19, 2005.
- Maiman, *Nature*, 1960.
- Mather, T., Pyle, D., and Oppenheimer, C., “Tropospheric volcanic aerosol,” *Volcanism and the Earth’s Atmosphere*, vol. 139, pp. 189–212, 2003.
- McClung, F. J. and Hellwarth, R. W., “Giant optical pulsations from ruby,” *Appl. Opt.*, vol. 1, no. S1, pp. 103–105, Jan 1962. [Online]. Available: <http://ao.osa.org/abstract.cfm?URI=ao-1-101-103>

- Menon, S., Hansen, J., Nazarenko, L., and Luo, Y., “Climate Effects of Black Carbon Aerosols in China and India,” *Science*, vol. 297, no. 5590, pp. 2250–2253, 2002. [Online]. Available: <http://www.sciencemag.org/content/297/5590/2250.abstract>
- Mie, G., “Beiträge zur optik trüber medien, speziell kolloidaler metallösungen,” *Annalen der Physik*, vol. 330, pp. 377–445, 1908.
- Monahan, E. C., “Sea spray as a function of low elevation wind speed,” *Journal of Geophysical Research*, vol. 73, p. 1127–1137, 1968.
- Müller, D., Wagner, F., Wandinger, U., Ansmann, A., Wendisch, M., Althausen, D., and Hoyningen-Huene, W.von, “Microphysical particle parameters from extinction and backscatter lidar data by inversion with regularization: Experiment,” *Appl. Opt.*, vol. 39, no. 12, pp. 1879–1892, Apr 2000. [Online]. Available: <http://ao.osa.org/abstract.cfm?URI=ao-39-12-1879>
- Murayama, T., Müller, D., Wada, K., Shimizu, A., Sekiguchi, M., and Tsukamoto, “Characterization of asian dust and siberian smoke with multiwavelength raman lidar over tokyo, japan in spring 2003,” *Geophysical Research Letters*, vol. 31, 2004.
- Murayama, T., Okamoto, H., Kaneyasu, N., Kamataki, H., and Miura, K., “Application of lidar depolarization measurement in the atmospheric boundary layer: Effects of dust and sea-salt particles,” *Journal of Geophysical Research*, vol. 104, pp. 31,781–31,792, 1999.
- Myhre, G. and Stordal, F., “Global sensitivity experiments of the radiative forcing due to mineral aerosols,” *Journal of Geophysical Research*, vol. 106, 2001.
- NOAA, “State of the climate: Global analysis for december 2010.” *NOAA, National Climatic Data Center*, vol. published online, 2011.
- Papayannis, A., Amiridis, V., Mona, L., and al., G. T.et, “Systematic lidar observations of saharan dust over europe in the frame of earlinet (2000–2002),” *Geophysical Research Letters*, vol. 113, p. D10204, 2008.
- Parker, D. E., Wilson, H., Jones, P. D., Christy, J. R., and Folland, C. K., “The impact of mount pinatubo on world-wide temperatures,” *International Journal of Climatology*, vol. 16, p. 487–497, 1996.
- Prospero, J. M. and Carlson, T. N., “Vertical and areal distribution of saharan dust over the western equatorial north atlantic ocean,” *Journal of Geophysical Research*, vol. 77, p. 5255–5265, 1972.
- Prospero, J. M., Ginoux, P., Torres, O., Nicholson, S. E., and Gill, T. E., “Environmental characterization of global sources of atmospheric soil dust derived from the nimbus7 toms absorbing aerosol product, rev,” *Geophys*, vol. 40, p. 2002, 2002.

- Raes, F., Bates, T., McGovern, F., and Van Liedekerke, M., "The 2nd aerosol characterization experiment (ace-2): general overview and main results." *Tellus B*, vol. 52, pp. 111–125, 2000.
- Ramanathan, V. and Carmichael, G., "Global and regional climate changes due to black carbon," *Nature Geoscience*, vol. 1, pp. 221–227, 2008.
- Rampino, M. R. and Self, S., "Historic eruptions of tambora (1815), krakatau (1883), and agung (1963), their stratospheric aerosols, and climatic impact," *Quaternary Research*, vol. 18, no. 2, pp. 127 – 143, 1982. [Online]. Available: <http://www.sciencedirect.com/science/article/B6WPN-4DV0MWT-2H/2/ef9fa93e8c98ea8c033521c008d82a6b>
- Reheis, M. C., Goodmacher, J. C., Harden, J. W., McFadden, L. D., Rockwell, T. K., Shroba, R. R., Sowers, J. M., and Taylor, E. M., "Quaternary soils and dust deposition in southern Nevada and California," *Geological Society of America Bulletin*, vol. 107, no. 9, pp. 1003–1022, September, 1995. [Online]. Available: <http://gsabulletin.gsapubs.org/content/107/9/1003.abstract>
- Reid, J. S., Eck, T. F., Christopher, S. A., Koppmann, R., Dubovik, O., Eleuterio, D. P., Holben, B. N., Reid, E. A., and Zhang, J., "A review of biomass burning emissions part iii: intensive optical properties of biomass burning particles," *Atmospheric Chemistry and Physics*, vol. 5, no. 3, pp. 827–849, 2005. [Online]. Available: <http://www.atmos-chem-phys.net/5/827/2005/>
- Reid, J. S., Koppmann, R., Eck, T. F., and Eleuterio, D. P., "A review of biomass burning emissions part ii: intensive physical properties of biomass burning particles," *Atmospheric Chemistry and Physics*, vol. 5, no. 3, pp. 799–825, 2005. [Online]. Available: <http://www.atmos-chem-phys.net/5/799/2005/>
- Robock, A., "Volcanic eruptions and climate," *Reviews of Geophysics*, vol. 38, pp. 191–219, 2000.
- Rosenfeld, D., "Trmm observed first direct evidence of smoke from forest fires inhibiting rainfall," *Geophysical Research Letters*, vol. 26, p. 3105–3108, 1999.
- Rosenfeld, D., Rudich, Y., and Lahav, R., "Desert dust suppressing precipitation: A possible desertification feedback loop," *Proceedings of the National Academy of Sciences of the United States of America*, vol. 98, no. 11, pp. 5975–5980, 2001. [Online]. Available: <http://www.pnas.org/content/98/11/5975.abstract>
- Sakai, T., Shibata, T., Kwon, S.-A., Kim, Y.-S., Tamura, K., and Iwasaka, Y., "Free tropospheric aerosol backscatter, depolarization ratio, and relative humidity measured with the raman lidar at nagoya in 1994-1997: contributions of aerosols from the asian continent and the pacific ocean," *Atmospheric Environment*, vol. 34, no. 3, pp. 431 – 442, 2000. [Online]. Available: <http://www.sciencedirect.com/science/article/B6VH3-3Y162CG-9/2/b2c145167bea4cadb32ff5aaaf37adb4b>



- Sakai, T., Nagai, T., Zaizen, Y., and Mano, Y., “Backscattering linear depolarization ratio measurements of mineral, sea-salt, and ammonium sulfate particles simulated in a laboratory chamber,” *Appl. Opt.*, vol. 49, no. 23, pp. 4441–4449, Aug 2010. [Online]. Available: <http://ao.osa.org/abstract.cfm?URI=ao-49-23-4441>
- Satheesh, S. and Moorthy, K. K., “Radiative effects of natural aerosols: A review,” *Atmospheric Environment*, vol. 39, no. 11, pp. 2089 – 2110, 2005. [Online]. Available: <http://www.sciencedirect.com/science/article/B6VH3-4FJGWDS-3/2/82028899d671058f9a9e50dbd991a0fc>
- Schladitz, A., Müller, T., Nordmann, S., Tesche, M., Groß, S., Freudenthaler, V., and al.et, “In situ aerosol characterization at cape verde, part 2: Relative humidity and wavelength dependence of aerosol optical properties,” 2011, tellus B - accepted.
- Schladitz, A., Müller, T., Nowak, A., Kandler, K., Lieke, K., Massling, A., and al.et, “In situ aerosol characterization at cape verde, part 1: Particle number size distributions, hygroscopic growth and state of mixing of marine and saharan dust aerosol,” 2011, tellus B - accepted.
- Sokolik, I. N. and Toon, O. B., “Direct radiative forcing by anthropogenic airborne mineral aerosols,” *Nature*, vol. 381, pp. 681 – 683, 1996.
- Sokolik, I. N., Winker, D. M., Bergametti, G., Gillette, D. A., Carmichael, G., Kaufman, Y. J., Gomes, L., Schuetz, L., and Penner, J. E., “Introduction to special section: Outstanding problems in quantifying the radiative impacts of mineral dust,” *Journal of Geophysical Research*, vol. 106, pp. 18,015–18,027, 2001.
- Tang, I., Tridico, A., and Fung, K., “Thermodynamic and optical properties of sea salt aerosols,” *Journal of Geophysical Research*, vol. 102, pp. 23 269–23 275, 1997.
- Tanré, D., Haywood, J., Pelon, J., Leon, J., Chatenet, B., Formenti, P., Francis, P., Goloub, P., Highwood, E., and Myhre, G., “Measurement and modeling of the saharan dust radiative impact: Overview of the saharan dust experiment (shade),” *Journal of Geophysical Research*, vol. 108, pp. 8574+, 2003.
- Tegen, I. and Fung, I., “Contribution to the atmospheric mineral aerosol load from land surface modification,” *Journal of Geophysical Research*, vol. 100, no. D9, pp. 18,707–18,726, 1995.
- Tegen, I., Hollrig, P., Chin, M., Fung, I., Jacob, D., and Penner, J., “Contribution of different aerosol species to the global aerosol extinction optical thickness: Estimates from model results,” *Journal of Geophysical Research*, vol. 102, pp. 23,895–23,915, 1997.
- Tegen, I., Werner, M., Harrison, S. P., and Kohfeld, K. E., “Relative importance of climate and land use in determining present and future global soil dust emission,” *Geophysical Research Letters*, vol. 31, p. L05105, 2004.

- Tesche, M., Ansmann, A., Müller, D., Althausen, D., Engelmann, R., Freudenthaler, V., and Groß, S., “Vertically resolved separation of dust and smoke over cape verde using multiwavelength raman and polarization lidars during saharan mineral dust experiment 2008,” *Journal of Geophysical Research*, vol. 114, p. D13202, 2009.
- Tesche, M., Ansmann, A., Müller, D., Althausen, D., Mattis, I., Heese, B., Freudenthaler, V., Wiegner, M., Esselborn, M., Pisani, G., and Knippertz, P., “Vertical profiling of saharan dust with raman lidars and airborne hsrl in southern morocco during samum,” *Tellus B*, vol. 61, p. 144–164, 2009.
- Toledano, C., Wiegner, M., Garhammer, M., Seefeldner, M., Gasteiger, J., Müller, D., and Köpke, P., “Spectral aerosol optical depth characterization of desert dust during samum 2006,” *Tellus B*, vol. 61, p. 216–228, 2009.
- Trenberth, K. E. and Dai, A., “Effects of mount pinatubo volcanic eruption on the hydrological cycle as an analog of geoengineering,” *Geophysical Research Letters*, vol. 34, p. L15702, 2007.
- Twomey, S., “Pollution and the planetary albedo,” *Atmospheric Environment (1967)*, vol. 8, no. 12, pp. 1251 – 1256, 1974. [Online]. Available: <http://www.sciencedirect.com/science/article/B757C-48CFS0N-J2/2/009cf52c35e42afdb2e4cb730f3cde4e>
- Wandinger, U., Tesche, M., Seifert, P., Ansmann, A., Müller, D., and Althausen, D., “Size matters: Influence of multiple scattering on calipso light-extinction profiling in desert dust,” *Geophysical Research Letters*, vol. 37, p. L10801, 2010.
- Washington, R., Todd, M., Middleton, N. J., and Goudie, A. S., “Dust-storm source areas determined by the total ozone monitoring spectrometer and surface observations,” *Annals of the Association of American Geographers*, vol. 93, p. 297–313, 2003.
- Weinzierl, B., Petzold, A., Esselborn, M., Wirth, M., Rasp, K., Kandler, K., Schütz, L., Köpke, P., and Fiebig, M., “Airborne measurements of dust layer properties, particle size distribution and mixing state of saharan dust during samum 2006,” *Tellus B*, vol. 61, p. 96–117, 2009.
- Weinzierl, B., Sauer, D., Esselborn, M., Petzold, A., Mund, S., Veira, A., Tesche, M., Ansmann, A., and Wirth, M., “Airborne observations of microphysical and optical properties of dust and biomass burning aerosol layers in the cape verde region during samum 2008.” 2011, tellus B - submitted.
- Wiegner, M., Gasteiger, J., Kandler, K., Weinzierl, B., Rasp, K., Esselborn, M., Freudenthaler, V., Heese, B., Toledano, C., Tesche, M., and Althausen, D., “Numerical simulations of optical properties of saharan dust aerosols with emphasis on lidar applications,” *Tellus B*, vol. 61, p. 180–194, 2009.

- Wiegner, M., Gasteiger, J., Groß, S., Schnell, F., Freudenthaler, V., and Forkel, R., “Characterization of the eyjafjallajökull ash-plume: Potential of lidar remote sensing,” *Physics and Chemistry of the Earth, Parts A/B/C*, vol. In Press, Accepted Manuscript, pp. –, 2011. [Online]. Available: <http://www.sciencedirect.com/science/article/B6X1W-521M6DC-1/2/df4c65196c7fbabc1221a92d6f6f10ae>
- Winker, D. M., Hunt, W. H., and McGill, M. J., “Initial performance assessment of caliop,” *Geophysical Research Letters*, vol. 34, p. L19803, 2007.
- Wise, M., Biskos, G., Martin, S., Russell, L., and Buseck, P., “Phase transitions of single salt particles studied using a transmission electron microscope with an environmental cell,” vol. 61, p. 12–31, 2005.
- Wu, L., “Impact of saharan air layer on hurricane peak intensity,” *Geophysical Research Letters*, vol. 34, p. L09802, 2007.
- Zender, C. S., Miller, R. L., and Tegen, I., “Quantifying mineral dust mass budgets: Terminology, constraints, and current estimates,” *EOS*, vol. 85, p. 509–512, 2004.



# Acknowledgment

This thesis is the result of a research work at the Meteorological Institute (MIM) of the Ludwig-Maximilians-Universität (LMU), München. During this particular period I was accompanied and supported by many people. Therefore I want to take the opportunity to thank those numerous people.

First of all I want to thank Dr. Matthias Wiegner for giving me the opportunity for this work, for his excellent guidance during the last years and for many constructive discussions of this thesis. Furthermore, I want to thank my supervisor Prof. Dr. Bernhard Mayer for his interest and support. Also many thanks to my co-supervisor Dr. Bernadett Weinzierl for many fruitful discussions and her helpful suggestions.

My special thanks go to Dr. Volker Freudenthaler for the technical help he gave me, for his constructional critique and for the many inspiring discussions. I also want to thank him for the excellent collaboration during several field experiments and for providing the MULIS measurements required for this work.

Thanks to Dr. Albert Ansmann and especial Matthias Tesche of the Leibniz Institute for Tropospheric Research, Leipzig, for the amicable collaboration during the SAMUM field experiment, for many constructive discussions and for providing lidar measurements and analyses of the Bertha system.

I would like to thank Dr. Carlos Toledano for providing the SSARA measurements during SAMUM-2, and Alexander Schladitz and Dr. Konrad Kandler for providing the in-situ measurements concerning the volume fraction during SAMUM-2.

Many thanks to my colleagues of the MIM lidar group, especially Franziska Schnell for her support during exhausting measurement periods and Josef Gasteiger for numerous helpful discussions.

Zum Schluss möchte ich den Mitgliedern meiner Familie danken, für ihre Unterstützung und Ermutigung, und für ihre Liebe und Ablenkung, wenn diese nötig war. Ein besonderer Dank auch an Tom, dafür, dass er mich beständig angetrieben hat.

This work was mainly funded by the German Research Foundation (Deutsche Forschungsgemeinschaft) within the SAMUM project under grant number FOR 539.



# Lebenslauf

Silke Martha Groß

## zur Person

Name Silke Martha Groß

geboren am 15. Dezember 1978

Geburtsort Kulmbach

Familienstand ledig

## Schulbildung

09/1983 - 07/1989 Besuch der Grundschule Mainleus

09/1989 - 06/1998 Besuch des Caspar-Vischer-Gymnasiums, Kulmbach

## Berufsausbildung

09/1998 - 02/2001 Ausbildung zur Industriekauffrau  
Medienhaus Baumann GmbH & Co. KG, Kulmbach

## Studium

10/2002 - 05/2007 Studium der Meteorologie an der  
Ludwig-Maximilians-Universität, München

Abschluss Dipl. Meteorologe

seit 06/2007 Promotion am Meteorologischen Institut der  
Ludwig-Maximilians-Universität, MIM

## Beschäftigungsverhältnisse

03/2001 - 09/2001 Sachbearbeiterin  
Medienhaus Baumann GmbH & Co. KG, Kulmbach

10/2001 - 09/2002 Sachbearbeiterin  
Vereinte Krankenversicherung AG, München